16

Geology of Ganymede

Robert T. Pappalardo
LASP and Dept. of Astrophysical & Planetary Sciences, University of Colorado

Geoffrey C. Collins
Astronomy & Physics Department, Wheaton College

James W. Head III
Dept. of Geological Sciences, Brown University

Paul Helfenstein
Center for Radiophysics & Space Research, Cornell University

Thomas B. McCord
Hawaii Institute of Geophysics & Planetology

Jeffrey M. Moore
NASA Ames Research Center

Louise M. Prockter
The Johns Hopkins University Applied Physics Laboratory

Paul M. Schenk
Lunar and Planetary Institute

John R. Spencer
Lowell Observatory

16.1 INTRODUCTION

16.1.1 Overview

Ganymede is a planet-sized world, the solar system's largest satellite with a radius of 2631 km. Its physiography, geology, geophysics, surface composition, and evolution are correspondingly planet-like in intricacy. The satellite's density of 1.94 g/cm^3 implies a bulk composition that is about 60% rock and 40% ice, and gravity data from the *Galileo* spacecraft indicates that it is strongly differentiated (Chapter 13). Ganymede is the only moon known to generate an internal magnetic field, implying a hot convecting core of liquid iron alloy; moreover, there are indications of an induced field component, suggesting a deep internal ocean of briny water (Chapter 21).

Ganymede tells of a tumultuous past. Its surface consists of 34 to 35% ancient dark terrain, which is relatively heavily cratered, and 65 to 66% bright terrain, which is more recent and heavily tectonized (Shoemaker *et al.* 1982, Collins *et al.* 2000, Schenk *et al.* 2001). Multispectral evidence confirms that the bright terrain is ice-rich, while dark terrain contains a greater fraction of rocky material. Though its lithosphere is primarily water ice, the geology of bright terrain finds analogy with terrestrial rift zones. Frosts coat the polar latitudes with a thin shroud, hinting of interactions with the magnetospheric particles. Impact features of diverse forms and ages are clues to the interior and recount a turbulent past.

Ganymede is straddled in distance from Jupiter by its siblings Europa and Callisto, and in some respects is transitional between the two. Ganymede's dark terrain is reminiscent of Callisto's desolate landscape (Chapter 17), while its bright terrain evokes Europa's bizarrely tectonized surface (Chapter 15). In understanding Ganymede, we gain insight into its Galilean siblings. Indeed, Ganymede is arguably the solar system's "type example" icy satellite, flaunting terrains from which many other satellites can draw analogy.

This chapter reviews the current state of knowledge about Ganymede, with emphasis on the geology, geochemistry, and other properties of its surface. Other important aspects of Ganymede are discussed in chapters on the Galilean

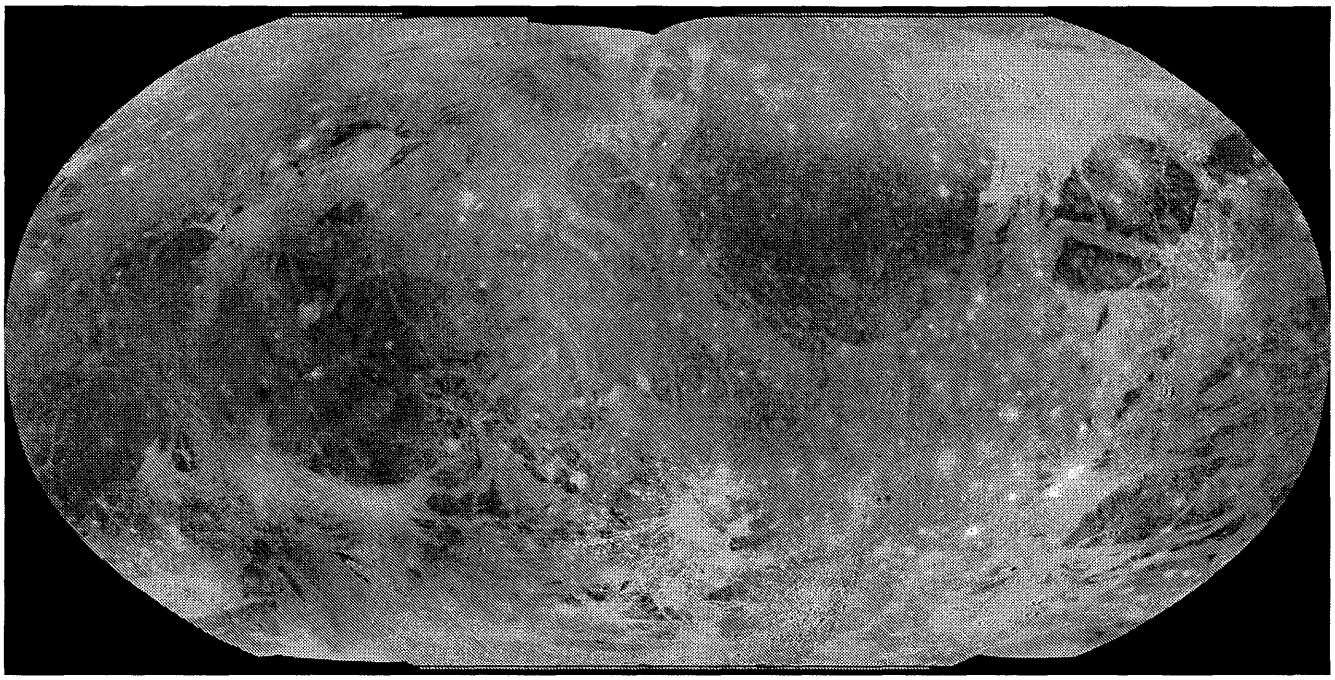

Figure 16.1. Global map of Ganymede constructed from *Voyager* and *Galileo* images, centered at the antijovian point (0° latitude, 180° longitude). Robinson map projection approximates the relative areas of dark and bright terrains.

satellite interiors (Chapter 13), magnetospheric interactions (Chapter 21), and atmospheres (Chapter 19).

16.1.2 Data Sets

Beginning in the late 1950s and culminating in the early 1970s, telescopic spectra demonstrated the icy character of Ganymede's surface and indicated the presence of a dark component (see Morrison 1982 and Morrison and Burns 1976 for reviews). Telescopic data continue to be of great value to the study of Ganymede. For example, Earth-based observations continue to aid in understanding the distribution of oxygen and ultraviolet absorbing species (Section16.3.4), and atmospheric emissions (Chapter 19).

In December 1973, the *Pioneer 10* spacecraft's simple spin-scan Imaging Photopolarimeter revealed darker and brighter surface tracts (Gehrels 1976). But the diversity and complexity of the surface was not realized until the *Voyager 1* and *2* encounters of March and July of 1979. *Voyager 1* imaging covers much of the subjovian hemisphere at resolutions up to ~1 km/pixel. *Voyager 2* imaged the antijovian hemisphere and high southern latitudes at up to ~500 m/pixel, and its camera had a better modulation transfer function so returned sharper images than *Voyager 1*.

The *Galileo* spacecraft made six close encounters with Ganymede (orbits G1, G2, G7, G8, G28 and G29), enabling dedicated remote sensing campaigns by the Solid State Imaging (SSI) camera, Near-Infrared Mapping Spectrometer (NIMS), Photopolarimeter-Radiometer (PPR), and UltraViolet Spectrometer (UVS). Remote sensing data were also obtained during the more distant encounters of other Jupiter orbits; for example, the illuminated leading hemisphere was best observed on orbit C9 and the trailing hemisphere on orbits E6 and E14. Information regarding the 14 orbits during which Ganymede remote sensing data were successfully obtained are listed in eTable 16.1 (see accompanying CD).

Galileo imaging concentrated on high resolution (<200 m/pixel) samples of characteristic terrain and feature types, along with lower resolution (~0.8 to 3.6 km/pixel) imaging to improve upon *Voyager* global-scale imaging, notably in the leading and trailing hemispheres (Head *et al.* 1999). The high resolution coverage of Ganymede is quite limited in area, so conclusions from relatively few high resolution sites must be extrapolated to other regions, and *Voyager* data remain central to understanding the satellite. While this chapter emphasizes results based on *Galileo* spacecraft data, excellent *Voyager*-based syntheses are provided by Shoemaker *et al.* (1982) and McKinnon and Parmentier (1986).

16.2 GEOLOGY

The surface of Ganymede is divided into two principal terrain types, relatively old regions of dark terrain, and younger cross-cutting lanes of bright (typically grooved) terrain (Figures 16.1 and 16.2). Dark and bright terrains are visible through the satellite's thin polar caps, which extend equatorward to about ±40° latitude. Impact craters of a variety of morphologies, including bright patches termed palimpsests, pockmark the surface. The surface geology serves to constrain the properties and history of the lithosphere and deeper interior and the evolution of the satellite as a whole. These topics will be discussed in the following sections on dark terrain, bright grooved terrain, polar caps, and impact structures.

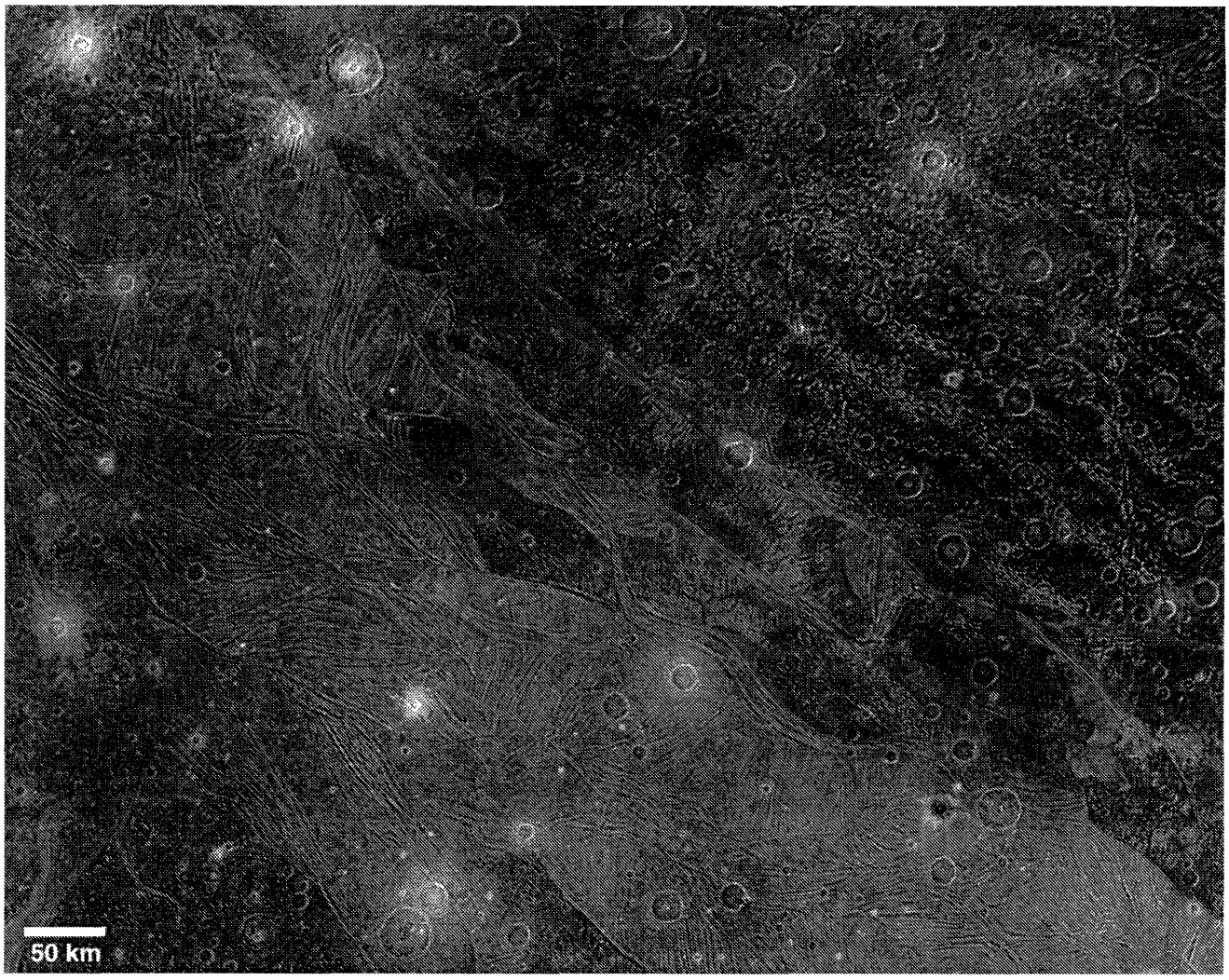

Figure 16.2. Boundary between the furrowed dark terrain of Galileo Regio (upper right) and the bright grooved terrain of Uruk Sulcus (lower left), as imaged by *Voyager 2* at ~1 km/pixel. Furrows of the Lakhmu Fossae system trend subparallel to the northern boundary of Uruk Sulcus, while the Zu Fossae cut them obliquely. A variety of crater forms are visible, including bright ray, central pit, and dark floor craters. North is to the top in this figure (and in other figures, unless indicated).

16.2.1 Dark Terrain

Areas of heavily cratered dark terrain (*regiones*, singular *regio*) comprise about 1/3 of Ganymede's surface. Based on measured crater densities, dark terrain is estimated to be >4 Gyr old (Neukum *et al.* 1997, 1998, Zahnle *et al.* 2003, and Chapter 18); thus, the terrain bears witness to processes affecting Ganymede since the earliest stages of its surface evolution. Dark terrain is transected by furrows ~10 km wide, which typically occur in sets (Smith *et al.* 1979a, 1979b). Geological investigations from *Galileo* high resolution images suggest that the dark material is composed of a relatively thin dark deposit overlying brighter icy material, and has been modified by surface processes such as sublimation, mass wasting, ejecta blanketing, and tectonism (Prockter *et al.* 1998, 2000). Dark terrain is quite heterogeneous in albedo at decameter scales, probably due to thermally driven segregation of ice and non-ice surface components (Spencer 1987a,b). The darkest deposits occur within local topographic lows such as crater and furrow floors, suggesting that downslope movement of the dark non-ice component also may play an important role in albedo segregation (Oberst *et al.* 1999). Though tectonism is generally far more abundant in lanes of bright terrain, *Galileo* images show that some zones of dark terrain are also pervasively tectonized (Patel *et al.* 1999, Prockter *et al.* 2000).

Furrow Systems

Evidence that dark terrain represents ancient surface material is provided in part by remnants of vast multi-ringed structures termed furrow systems (Smith *et al.* 1979a, 1979b and Figure 16.2). Ganymede's furrow systems are the oldest recognizable structures on the surface, predating almost all craters larger than 10 km in diameter (Passey and Shoemaker 1982). The majority of the furrows are arranged in sub-concentric sets, although some cross-cut the others at high angles. Such systems, also seen in the early cratering record of Callisto, are shallower and more subdued than multi-ringed basins on terrestrial planets. They date to an

epoch when Ganymede's surface may have had a higher thermal gradient, perhaps overlying a more ductile, or even liquid, interior (Chapter 18). Because dark terrain is significantly disrupted by younger swaths of bright terrain, furrow systems are incomplete. When intact, however, the largest known system (the Lakhmu Fossae in Galileo Regio, see Figure 16.2) would have been hemispherical in scale (Schenk and McKinnon 1987).

Individual furrows are linear to curvilinear troughs bounded by sharp, raised rims. They extend from tens to hundreds of kilometers in length and are typically ~6 to 20 km wide, with generally flat floors and raised rims (Smith *et al.* 1979a, Shoemaker *et al.* 1982). Interfurrow spacing is fairly uniform at ~50 km, although spacing is generally closer towards the center of a concentric system (Passey and Shoemaker 1982). Topographic models derived from high resolution stereo images of Galileo Regio show that one rim rises a full kilometer above its furrow floor and 900 m above the level of the surrounding terrain (Prockter *et al.* 1998), consistent with estimates from shadow measurements of furrow depth (Murchie and Head 1988).

Voyager-era mapping and photogeologic analysis of the furrow systems led to a variety of models for their formation (e.g., Cassachia and Strom 1984, Schenk and McKinnon 1987, Murchie *et al.* 1990). On the basis of morphology and planform, along with their similarity to impact-formed multi-ringed structures on Europa (Moore *et al.* 1998, 2001, Kadel *et al.* 2000), they are now generally accepted to be fault-bounded troughs formed in response to large impacts into a relatively thin lithosphere early in Ganymede's history (McKinnon and Melosh 1980). Individual furrows likely formed during basin collapse, as the result of radially inward asthenospheric flow with accompanying brittle failure of the overlying lithosphere (McKinnon and Melosh 1980, Melosh 1982). The type and extent of the resulting fault pattern would have depended on the scale of the impact and the rheological structure of the satellite at the time of formation. Furrows may have been reactivated and modified by later endogenic activity (Murchie *et al.* 1990). Raised furrow rims probably formed when the long-wavelength components of fault-induced relief relaxed, resulting in the flexural and/or viscous uplift of the bounding escarpments (McKinnon and Melosh 1980, Pappalardo *et al.* 2003).

Dark Terrain Small-Scale Characteristics

Geological sub-units have been recognized in *Voyager*-era mapping of dark terrain (e.g., Guest *et al.* 1988) but, overall, dark terrain is relatively homogeneous at a large scale. At high resolution, dark terrain is surprisingly heterogeneous as imaged at relatively low phase angles (Figure 16.3). Geological mapping from *Galileo* images has allowed the identification of a variety of sub-units on the basis of relative albedo, morphology, and geological occurrence (Prockter *et al.* 1998, Figueredo *et al.* 1998, 1999). These units are common to several well-separated dark terrain areas, and they have comparable positions in the stratigraphic record, implying similar modes of formation and modification (Prockter *et al.* 2000).

The majority of dark terrain comprises low- and intermediate-albedo plains. Cross-cutting relationships show that the intermediate-albedo plains (I of Figure 16.3) are the oldest recognizable units, and also the most ubiquitous, occurring around both higher and lower topographic features. This unit may represent areas of Ganymede's crust that have been heavily modified by later surface processes. The lowest albedo unit (L) is found only on the floors of furrows and is interpreted to be dark material that has been shed from adjacent furrow walls and is concentrated in topographic lows. This intermediate and dark material has likely been concentrated by a variety of processes including sublimation and mass wasting. Plains material with a smooth or hummocky texture (S) and a higher relative albedo mantles surrounding units, is relatively young, and occurs in close association with impact features; therefore, it is interpreted to be impact ejecta.

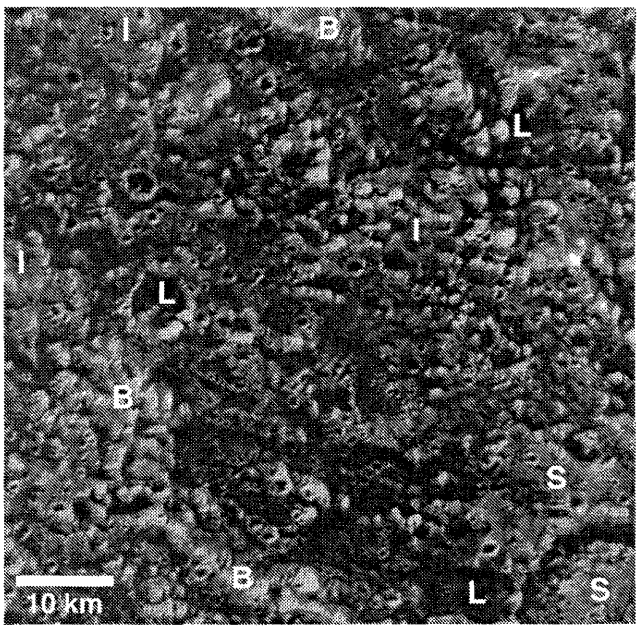

Figure 16.3. Significant heterogeneity is revealed by *Galileo* views of dark terrain in Galileo Regio. Dark material concentrates in topographic lows, while bright material tends to reside on topographic highs and steep slopes. Prockter *et al.* (1998) identify four distinct geological units in this area, with examples labeled here: low-albedo plains (L), intermediate-albedo plains (I), bright units (B), and smooth plains (S). Pole-facing (northern) slopes are generally brighter than Sun-facing slopes, suggesting sublimation and deposition of ice. From *Galileo* SSI observation G1GSGALREG01 (75 m/pixel, incidence angle 30°, phase angle 21°).

Of contemporaneous age to the plains material are bright units (S) commonly associated with high-standing topography. Some form curvilinear units, recognizable as furrow and crater rims. Others are isolated massifs, interpreted as remnants of furrow or crater rims that have been disaggregated through tectonic activity and mass wasting, such that their original forms are no longer recognizable.

Dark Terrain Endogenic Processes

Tectonism. Tectonic deformation is a major factor in the formation of Ganymede's grooved terrain and also has played an important role in dark terrain evolution. Two main types of tectonic deformation have been identified: one is furrow formation and related tectonics, and the other is

dark terrain fracturing which appears to be a precursor to grooved terrain development. Areas far from grooved terrain are more likely to be dominated by furrow tectonics, while regions closer to grooved terrain areas tend to show significant additional fracturing and/or reactivation of preexisting structures (Shoemaker *et al.* 1982, Murchie *et al.* 1986, Figueredo *et al.* 1999, Prockter *et al.* 2000).

A portion of Nicholson Regio imaged at high resolution by *Galileo* (Figure 16.4) is heavily tectonized, with several swaths of closely spaced fractures trending in several orientations. Fourier analysis of constituent ridge and trough sets reveals dominant wavelengths similar to those of bright terrain groove lanes (Patel *et al.* 1999). The orientation of the dark fractured terrain in Nicholson Regio is similar to that of nearby older furrows, implying that this tectonism exploited preexisting weaknesses created during earlier furrow formation. Evidence is also found for focusing of small-scale tectonic features within individual furrows in that there is a greater areal density of fractures within older broad furrows, as near Byblus Sulcus (see Figure 16.13) and Anshar Sulcus (see Figure 16.14).

Some craters act as zones of weakness that focus tectonic deformation through them, as is especially evident in the Nicholson Regio area (Asphaug *et al.* 1998, Figueredo *et al.* 1998, 1999, Prockter *et al.* 2000). In some cases, two differently oriented fracture sets intersect near a crater center, a phenomenon that may be analogous to tectonic focusing observed near terrestrial calderas, where faults deflect toward the zone of weakness (e.g., van Wyk de Vries and Merle 1996).

Icy Volcanism? From *Voyager* images, dark terrain was interpreted to consist of an old, heavily cratered surface buried by overlapping blankets of icy volcanic material (Croft and Strom 1985, Croft and Goudreau 1987, Murchie *et al.* 1989, Croft *et al.* 1990). This interpretation was supported by inferences of depleted small crater densities, embayment of large craters, and smooth areas associated with furrows (Cassachia and Strom 1984, Murchie *et al.* 1990, Lucchitta *et al.* 1992). Schenk and Moore (1995) proposed that volcanic activity on Ganymede included extrusion of icy materials into crater floors to form lobate domes and into furrow floors to create smooth dark deposits.

No unequivocal identification of dark terrain volcanism, such as lobate materials with an identifiable source vent, has yet been made based upon high resolution images (Prockter *et al.* 2000). Candidate volcanic units identified at low resolution on the basis of embayment and texture were instead probably formed as fluidized impact ejecta (Figure 16.4); moreover, smooth dark materials in topographic lows probably accumulated by downslope movement of loose material (Prockter *et al.* 1998). Though evidence for volcanism could potentially exist below the current limits of resolution or in areas not yet imaged, the hypothesis of dark terrain volcanism is not supported by existing imaging data.

Dark Terrain Exogenic Processes

Mass wasting. Exogenic processes are those processes which operate external to the surface of a planet, including mass wasting. *Galileo* images provide strong evidence that mass wasting has been an important modification process in dark terrain (Prockter *et al.* 1998, Moore *et al.* 1999). However, a lesser degree of degradation is inferred than on Callisto, which has a more subdued landscape and a substantial widespread regolith (Chapter 17). Evidence for downslope movement of Ganymede's dark material is found in the form of low albedo streaks on otherwise bright slopes, with an inverted V-shape characteristic of mass wasting deposits on the Earth and other solar system bodies (Figure 16.5). Aprons of material at the base of such streaks are likely talus piles. The correlation of low albedo with local topographic lows (Oberst *et al.* 1999) suggests that loose dark material has collected in furrow floors and other low-lying areas. This style of mass wasting is consistent with gravity-driven dry sliding or slumping in areas of oversteepened slopes (Moore *et al.* 1999).

Sublimation. High resolution images of Galileo Regio (Figure 16.3) show a concentration of dark material on sun-facing slopes, with brighter slopes facing away from the direction of solar illumination, contrary to what might be expected based on shading alone. This dichotomy is inferred to result from the sublimation and deposition of volatiles, specifically H_2O, from the surface (Squyres 1980a, Spencer 1987b, Spencer *et al.* 1998, Prockter *et al.* 1998). In this hypothesis, sun-facing slopes and topographic lows (where infrared radiation from the surroundings is concentrated) undergo enhanced sublimation. As water vapor is removed, a low albedo refractory material is left behind, forming a sublimation lag and consequently a darker surface. As the system evolves, the low albedo refractory deposit may grow thick enough for it to slough downslope, a process that may continue until sublimation slows and ceases from the smothering effect of a refractory lag cover. Based on retention of small craters in dark terrain, the depth of the dark lag deposit is probably a few meters to tens of meters on slopes, and may be deeper in topographic lows such as furrow floors. Condensation of water vapor as frost may occur on relatively cold pole-facing slopes and topographic highs. In addition, as dark material is shed off of these slopes, a relatively high albedo, ice-rich surface is revealed. Scarps that bound impact features in the dark terrain can be irregular to crenulate in planform, suggesting that crater material is undergoing erosion by scarp retreat perhaps related to sublimation (Moore *et al.* 1999).

These observations are consistent with models that predict sublimation to be an important process for the redistribution of ices on the Galilean satellites, notably at subkilometer spatial scales (Spencer 1987b, Moore *et al.* 1996). Sublimation of interstitial volatile ices within topography-supporting material may trigger mass wasting and thus may contribute significantly to degradation of topography at local scales, analogous to the erosional style inferred on Callisto (Chapter 17).

Sputtering. The energy imparted to Ganymede's surface by impinging particles from Jupiter's magnetosphere will cause sputtering, the ejection and redistribution of molecules, across Ganymede's surface (Chapter 20). Estimates of particle fluxes and ice sputtering rates suggest an erosion rate of $\sim$80 cm Gyr^{-1} in Ganymede's equatorial region, which is two orders of magnitude less than the expected sublimation rate (Cooper *et al.* 2001). Sputter ablation will be reduced by the presence of a refractory lag deposit, and

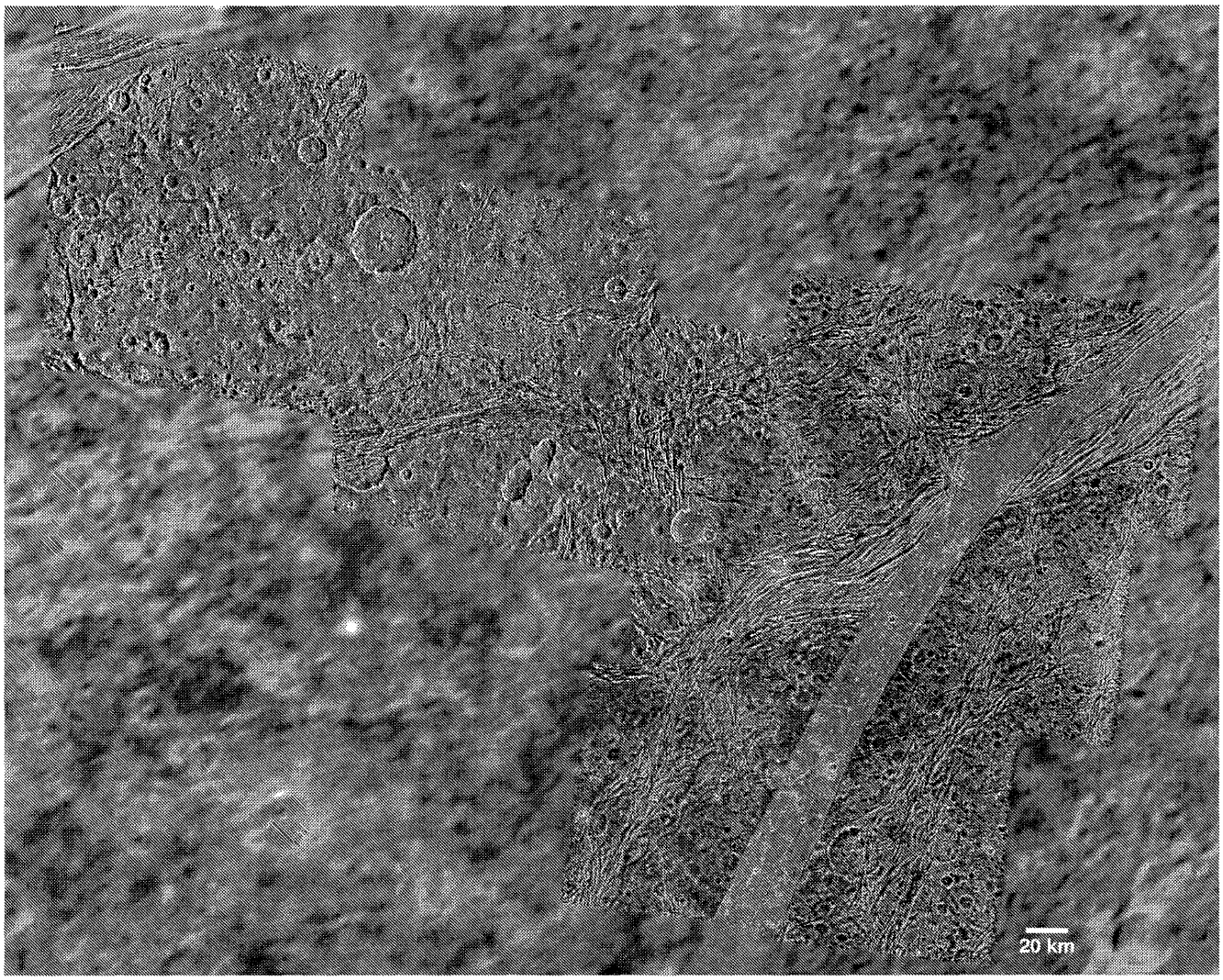

Figure 16.4. A portion of Nicholson Regio centered near 14°S, 353°W. Here the dark terrain is straddled by grooved terrain and shows evidence of heavy tectonic disruption. The NE-trending swath of smooth bright terrain in the southeast is Arbela Sulcus, and grooved swaths in the far northwest belong to the Mysia Sulci. The *Galileo* images reveal that irregular bright patches observed in the *Voyager 1* images (background) are generally tectonically disrupted areas and patches of impact ejecta. *Galileo* data is a mosaic of observations G7GSNICHOL01 (176 m/pixel, center and left) and 28GSARBELA02 (133 m/pixel, right).

impact gardening would distribute sputter-produced chemical products throughout the regolith. If sputtering rates were greater than the rate of thermal sublimation, the surface should be rehomogenized at timescales faster than those required to segregate it into dark and bright patches (Spencer 1987a); therefore, the presence of extreme albedo variations within dark terrain implies that sublimation does occur at a significantly higher rate than sputtering. It is therefore unlikely that sputtering is a major influence on dark terrain surface morphology, at least in the non-polar regions.

Interpretation and Geological Evolution of Dark Terrain

Ganymede's dark terrain is extremely heterogeneous at the scale of hundreds of meters, implying that the ice and non-ice components are distributed unevenly across the surface. The lowest albedo areas are stratigraphically young materials found at the bottom of furrows and within crater floors. Low albedo material forms a relatively thin veneer atop a brighter substrate and has likely been concentrated by a variety of processes including sublimation and mass wasting. High albedo material is found at topographically high elevations and commonly forms crater and furrow rims. Plains units are intermediate or low in albedo, relatively old, and distributed somewhat randomly, but ubiquitously, across the surface. The presence of furrows, isolated massifs, and swaths of ridges and troughs indicate that tectonic activity has been instrumental in shaping dark terrain. No direct evidence for icy volcanism has been found within dark terrain.

These observations and inferences have led to a model for dark terrain in which the surface is comprised of a thin dark veneer of silicate-rich lag, overlying a cleaner, icier substrate (Figure 16.6). In this hypothesis, the substrate has a small amount of a low albedo component heterogeneously admixed, emplaced by projectile in-fall during the late stages of Ganymede's accretion. High albedo, topographically ele-

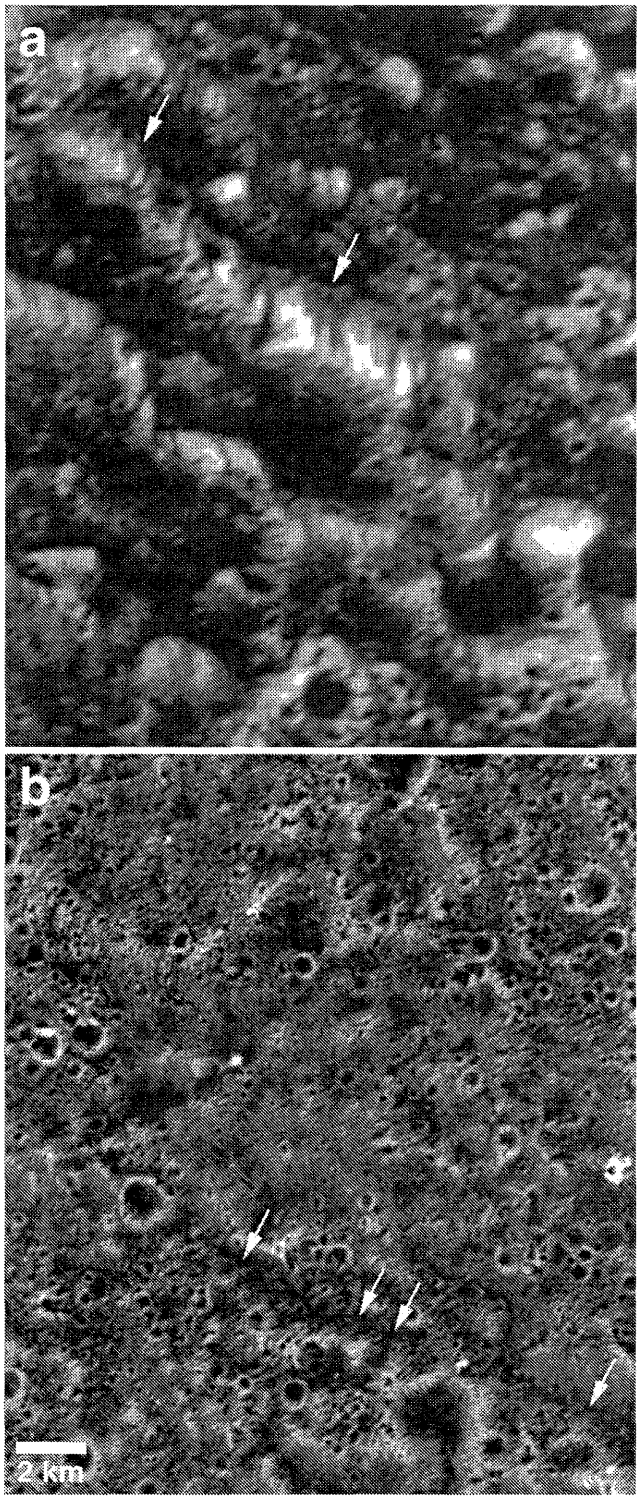

Figure 16.5. Detail of dark terrain (a) in Galileo Regio, and (b) in Nicholson Regio, shown at a common scale. In both images, dark material lies at the base of scarps with dark streaks oriented downslope (arrows), indicating downslope wasting of dark material. Compared to Galileo Regio, topography in the Nicholson Regio image is much more subdued. From *Galileo* SSI observations G1GSGALREG01 (75 m/pixel) and 28GSNICHOL01 (28 m/pixel), respectively.

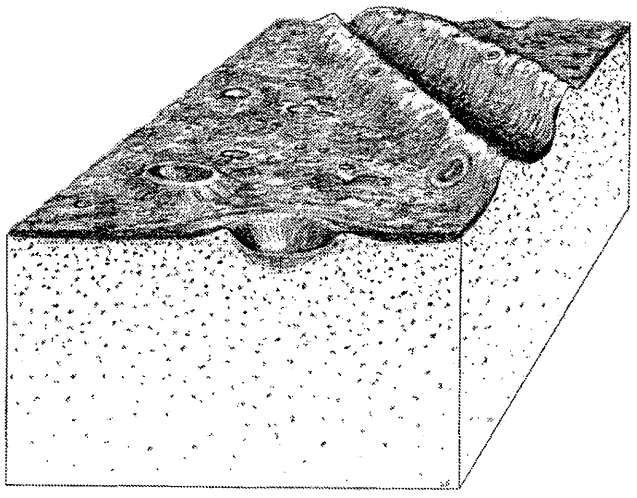

Figure 16.6. Schematic interpretation of dark terrain derived from *Galileo* observations. The low albedo material on Ganymede's surface is proposed to be a lag deposit of dark silicate material overlying cleaner ice. Impacts and furrow formation through the surface lag will result in brighter topographic features, and the lag deposit may be concentrated in topographic lows by mass wasting and thermal segregation. From Prockter *et al.* (1998).

vated units, such as crater and furrow rims, are inferred to be outcrops of icy substrate from which the dark lag deposit has sloughed off, and/or which have trapped a bright frost veneer. In the warmest regions and local topographic lows, notably sun-facing slopes and troughs, volatiles have been removed and the non-ice material has concentrated. Large impacts, including palimpsests, have penetrated the lag-enriched surface to deeper ice-rich levels, uniformly mixing and excavating the impacted material to create relatively bright ejecta. This model of dark terrain evolution is also consistent with observations in bright grooved terrain, discussed next.

16.2.2 Bright Grooved Terrain

Swaths of bright grooved terrain (*sulci*, singular *sulcus*, from the Latin for furrow or groove) are 10s to 100s of kilometers wide and cross-cut the older dark terrain, forming an intricate patchwork across 2/3 of Ganymede's surface. Bright grooved terrain has crater densities 2 to 10 times less than dark terrain, with a nominal age of ~2 Gyr; however, large uncertainties in the impact flux through time imply that grooved terrain may have been emplaced any time from ~400 Myr to >4 Gyr ago (Zahnle *et al.* 1998, 2003, Chapter 18). Observations of grooved terrain have been used to constrain models of Ganymede's surface, interior, and orbital evolution.

The view of grooved terrain formation developed from *Voyager* images was that bright cells are broad graben that have been infilled by extrusion of relatively clean (silicate-poor) liquid water, warm ice, or icy slush that hardened as it cooled to ambient temperatures (Golombek and Allison 1981, Golombek 1982, Parmentier *et al.* 1982, Shoemaker *et al.* 1982, Squyres 1982, Allison and Clifford 1987). This model can be expressed as a three-step process: (1) formation of a broad fault-bounded graben in dark

terrain, (2) volcanic eruption of relatively clean water and/or ice to flood the broad graben and resurface the dark terrain within to create bright smooth terrain; and (3) further extension to produce the grooved terrain, either as sets of narrow subparallel graben, or as crevasse-like tension fractures subsequently modified through viscous relaxation and mass wasting.

Galileo observations have permitted these models to be further tested. Overall a rift-like model of grooved terrain is supported, with elements that include: multiple superimposed topographic wavelengths of deformation, a significant role for tilt-block style normal faulting, high thermal gradients, locally high extensional strain, the potential for tectonism alone to cause resurfacing in some regions, and a generally less prominent role for icy volcanism. The discussion below suggests up to four key stages in the evolution of grooved terrain (Figure 16.7): (i) reactivation of dark terrain tectonic structures; (ii) extensional tectonic deformation of preexisting terrain; (iii) possible icy volcanic resurfacing with continued faulting; and (iv) cross-cutting by more recent lanes of grooved terrain.

Bright Terrain Characteristics

Regional-Scale Characteristics. Much of the bright terrain is textured by subparallel ridges and troughs (Smith *et al.* 1979a, 1979b) in elongate swaths or truncated polygons. This "grooved terrain" was described by Shoemaker *et al.* (1982) as sets of curvilinear, alternating ridges and troughs that can be continuous along their trend for hundreds of kilometers. The ridges and troughs of an individual set commonly trend subparallel to the long axis of the elongate cell of bright terrain in which they occur, but in regions of complexly cross-cutting sulci they can also trend obliquely to a polygon's long axis (Figure 16.2). A hierarchy of grooves has been recognized, with more prominent grooves commonly bounding individual cells, while structures within a groove set are typically less prominent (Golombek and Allison 1981).

As observed at the regional scale in *Voyager* images, structural relationships among troughs have led to an extensional tectonic interpretation for the terrain (Smith *et al.* 1979a, 1979b, Shoemaker *et al.* 1982). A continuum of forms exists from single troughs to ridge-and-trough sets to complexly grooved terrain, suggesting a common genesis. Because single troughs are suggestive of graben, association with multiple subparallel ridges and grooves argues for an origin by extension. Observations that grooved terrain generally lies lower than surrounding terrain, and that relatively deep bounding troughs commonly define the margins of ridge and trough sets, are consistent with an extensional tectonic origin.

In some locations there appears to be an inheritance of structural patterns at the boundaries between dark terrain and grooved terrain, suggesting that prominent grooved terrain structures have utilized preexisting zones of structural weakness, specifically furrows, in dark terrain (Murchie *et al.* 1986), as illustrated schematically in Figure 16.7a. One such transition occurs at the northern boundary of Uruk Sulcus (Figure 16.2), where prominent structures within bright terrain trend subparallel to furrows of similar morphology, degree of curvature, and spacing within adjacent dark ter-

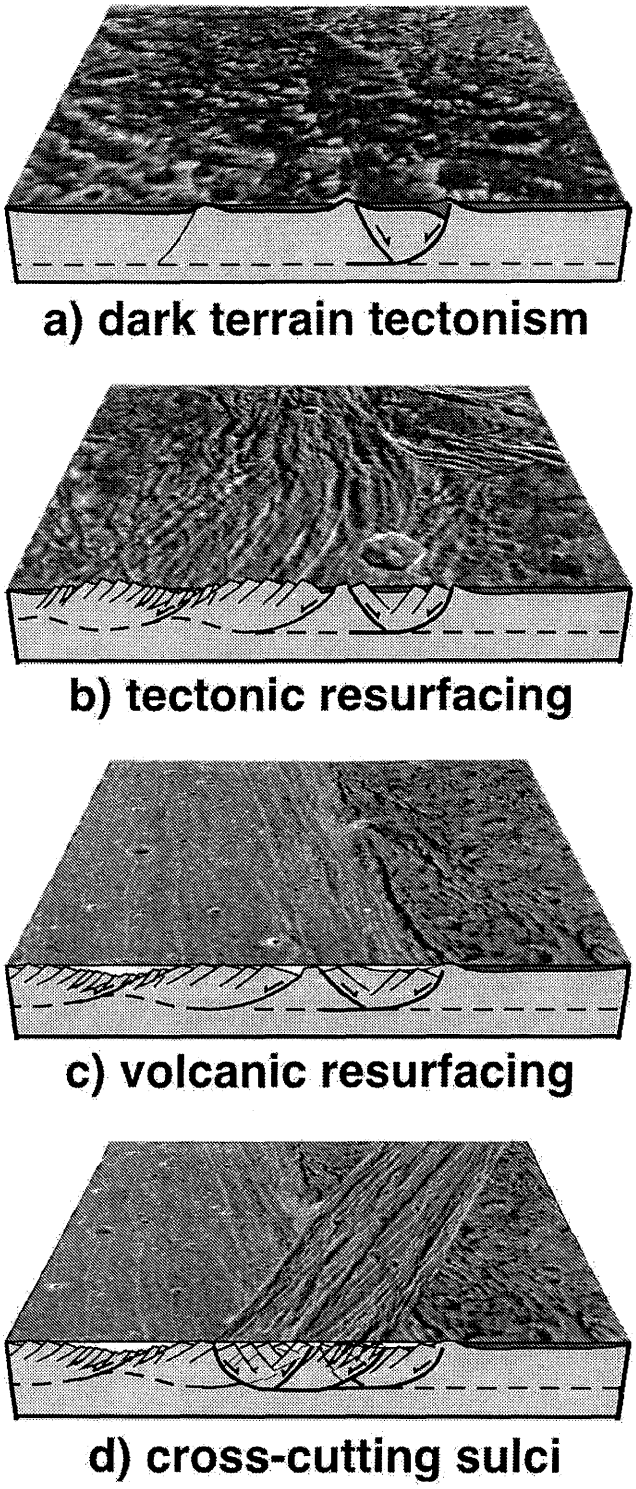

Figure 16.7. Summary model for the formation and evolution of grooved terrain. (a) Normal faults inferred to define furrows in dark terrain may be reactivated to focus later grooved terrain deformation. (b) Some grooved terrain may form by tectonic disruption of the preexisting surface, without concurrent icy volcanism. (c) Some grooved terrain may form by a combination of tectonism and icy volcanism which brightens and smooths the surface. (d) Bright terrain swaths can cross-cut one another, dissecting the preexisting surface into a polygonal patchwork.

rain of *Galileo* Regio. Global patterns of groove orientations have been investigated to help constrain the global causes of grooved terrain formation.

Intersecting grooved terrain sulci can exhibit complex stratigraphic relationships. From regional-scale *Voyager* imaging, it was suggested that newer grooved terrain structures commonly end against older, more prominent grooves in T-terminations, where the cross-bar of the T was inferred to be older (Golombek and Allison 1981). Subsequently, Murchie *et al.* (1986) recognized the significance of reactivation of older structures in creating grooved terrain stratigraphy. High resolution images ultimately demonstrated that newer grooved terrain typically cross-cuts and can destroy older terrain, creating the observed complex array of cross-cutting swaths (Figure 16.7d) (Collins *et al.* 1998a). The principal differences in interpretation arise from the realization based on *Galileo* images that newer cross-cutting sulci can effectively destroy the groove topography of older ones, in some cases leaving no recognizable trace of the older structures, as discussed below. Some orthogonally intersecting troughs form regions of reticulate terrain (see Figure 16.17), inferred to represent intersecting groove sets in which the preexisting grooves are preserved.

Smooth terrain is an additional type of bright terrain inferred from regional-scale images. Apparent smooth terrain is observed in polygonal regions bounded by prominent grooves or cells of grooved terrain, or in structurally unconfined regions such as alongside grooved terrain (Shoemaker *et al.* 1982). Smooth terrain was inferred to be of icy volcanic origin and contributed to the interpretation that volcanism is a critical component of grooved terrain emplacement. As discussed next, higher resolution imaging by *Galileo* demonstrates that truly smooth terrains are relatively rare, and that tectonic fabrics consisting of small ridges and lineaments are very common at sub-kilometer scales.

High Resolution Characteristics. The first high resolution images returned by *Galileo* (Figure 16.8a) were obtained at low phase angle, and reveal the extent of albedo heterogeneity in grooved terrain (Pappalardo *et al.* 1998a). Stereo imaging confirms the close correlation of albedo to topography, with the darkest material being concentrated in local topographic lows (Figure 16.8b) (Pappalardo *et al.* 1998a, Oberst *et al.* 1999). Bright material is generally located on ridge crests, dark material concentrates in the topographic lows between ridges, and intermediate albedo material is common on ridge slopes. There is a tendency for those slopes which receive the least total insolation during the day to be brighter, implying cold-trapping of water molecules (Spencer 1987b, Spencer *et al.* 1998, Pappalardo *et al.* 1997a, 1998a); however, either east or west facing slopes can be brightest (cf. 16.8 and 16.9), implying complex relationships between insolation, slope, and temperature. The correlation of albedo and topography implies that some "grooves" inferred in low incidence angle regional-scale images are actually low albedo stripes that closely correlate to topographic lows (Collins *et al.* 1998b).

At high resolution, the albedo contrast between "bright" and "dark" terrain can sometimes be elusive. Figure 16.9 shows the eastern boundary of Philae Sulcus, centered near 61°N, 168°W, within Ganymede's north polar hood. The *Voyager* context image (Figure 16.9, inset)

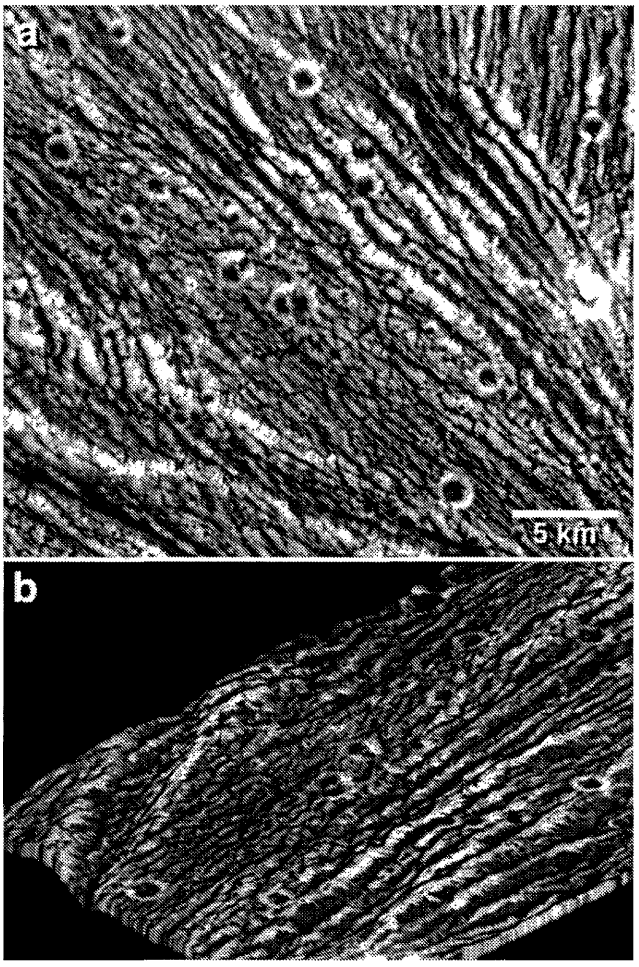

Figure 16.8. Fine-scale albedo and topography of grooved terrain in Uruk Sulcus. (a) A portion of *Galileo* image s0349758939, the first image returned from the *Galileo* spacecraft (74 m/pixel, incidence angle 13°, phase angle 16°, from observation G1GSURUSUL01). Brightness variations are due to variations in albedo, and are closely correlated to topography with dark material residing in local topographic lows. (b) Simulated view across the high resolution Uruk image from the northeast, generated using stereo image data and rectified with the resulting digital elevation model. Both fine-scale topography and longer-wavelength swells and troughs are evident. (Courtesy Bernd Giese, DLR, Institute of Planetary Exploration, Germany.)

shows a distinct contrast between the bright terrain of Philae Sulcus and the dark terrain of *Galileo* Regio. However, in the superimposed high resolution image strip, these terrains are most reliably distinguished by their texture and crater density, rather than their integrated albedos. Overlap in the albedos of "bright" and "dark" terrains was inferred from *Voyager*-based photometry (Squyres and Veverka 1981); however, disk-resolved photometric studies have not yet been performed on *Galileo* images, so the influence of lighting and viewing geometry on reflectance in individual *Galileo* images is not yet established.

Grooved terrain exhibits a range of superposed spacing scales of ridges and troughs. The close correlation of albedo to topography implies that profiles across albedo striping (at low incidence angle) or shading (at high incidence angle) reveals the wavelength characteristics of topography.

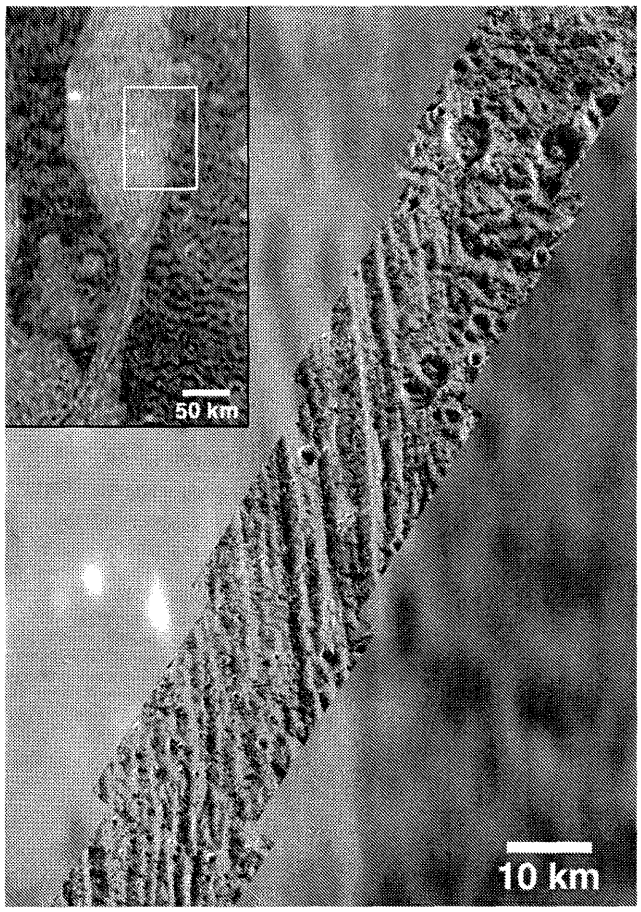

Figure 16.9. High resolution (47 m/pixel) images within Ganymede's north polar cap (centered at 61° latitude; incidence angle 64°, phase angle 33°, *Galileo* observation G2GSLTDKBD01). These images transect the eastern boundary of Philae Sulcus, from bright grooved terrain (west) to dark terrain (east). The albedo contrast apparent at *Voyager* resolution (inset and background) is not obvious in these high resolution images; instead the terrain types are more readily identified by their textural differences. North and east facing slopes in this region are bright, apparently having cold-trapped water frost. North is to the top, and the Sun illuminates the scene from the southeast.

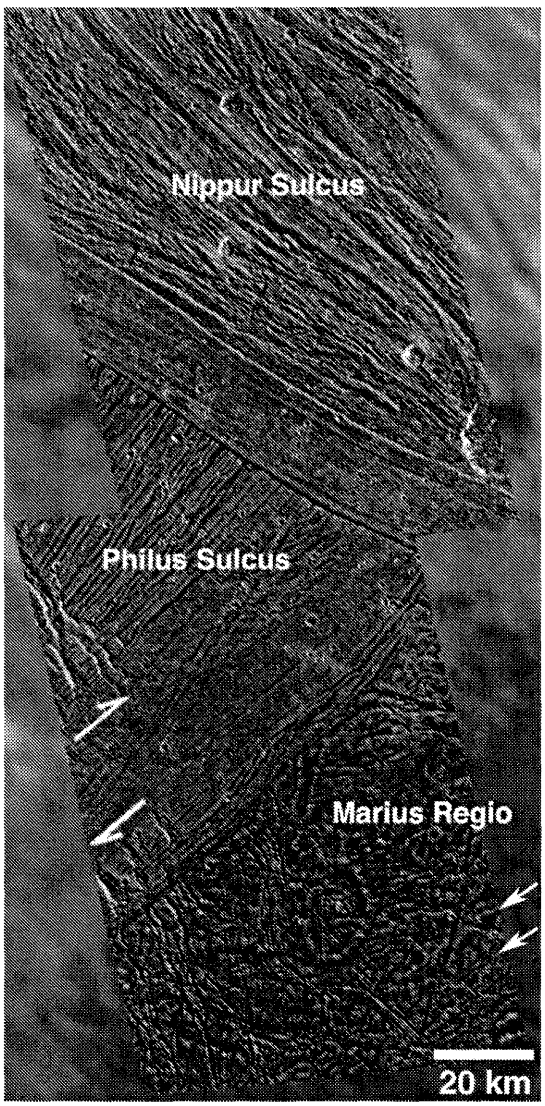

Figure 16.10. Boundaries between dark terrain of Marius Regio, grooved terrain of Philus Sulcus, and grooved terrain of Nippur Sulcus. Philus Sulcus displays grooved terrain with a horst-and-graben-like morphology. A lane of very smooth material marks the boundary between Philus and Nippur Sulci. Structural trends near the border of Marius Regio and Philus Sulcus suggest right-lateral shear (for example, displacing orthogonally trending structures at half-arrows), consistent with dextral shear straining of an oblong (20 × 12 km) crater visible in Marius Regio (Pappalardo and Collins 2003). Subtle structures within Marius Regio (e.g., at arrows) parallel the border between Philus Sulcus and Marius Regio, suggesting a genetic relationship. From *Galileo* observation G2GSNIPPUR01 (99 m/pixel), overlain onto *Voyager* image data.

The largest-scale grooves have a mean spacing of about 8 km, derived from Fourier analysis of photometric profiles across groove sets in *Voyager* images (Grimm and Squyres 1985). The spacing of ridges and troughs within a single set is typically regular, though variation is found among sets. Fourier analysis on several sites imaged by *Galileo* reveals multiple superposed wavelengths of topography (Patel *et al.* 1999). Multiple small-scale wavelengths (~1 to a few km) are generally superimposed on longer wavelength topography (~5 to 10 km). This result is confirmed by limited high resolution stereo imaging, which shows that small-scale ridges and troughs are superimposed on larger-scales swells and valleys (Figure 16.8b). These observations are best explained by a model of extensional necking in creating grooved terrain.

High resolution stereo imaging further reveals the detailed topographic characteristics of grooved terrain. In Uruk Sulcus, topographic amplitudes reach ~500 m and the resolved (long wavelength) slopes are ≤19° (Giese *et al.* 1998); superimposed smaller-scale ridges are probably ≤200 m high (Pappalardo *et al.* 1998a). These results are quite consistent with photoclinometric profiles from *Voyager* images which suggested that the long-wavelength ridges and grooves have crest-to-trough height differences typically 300–400 m and as great as 700 m, with slopes up to 20° (Squyres 1981).

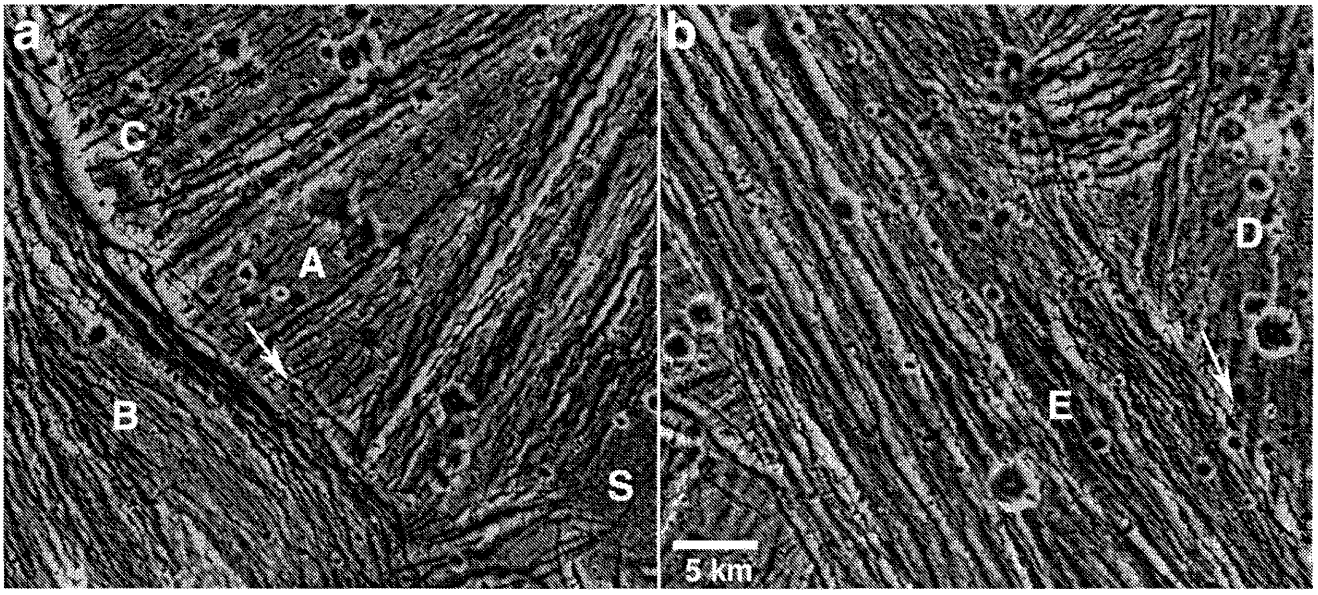

Figure 16.11. Grooved terrain within Uruk Sulcus, illustrating the process of tectonic resurfacing. (a) Boundary between older grooved terrain unit A with horst-and-graben-like morphology, and younger unit B with tilt-block-style morphology. Boundary relationships suggest that unit B has formed through tectonic dismemberment of unit A, exemplified by incipient structures (e.g., at arrow), and by an apparent cut 6 km crater immediately south of C. Smooth material at S suggests an earlier stage of icy volcanic resurfacing. (b) Unit E with tilt-block-style morphology has apparently formed at the expense of older grooved units, including D. Incipient structures associated with unit E have cut the flanking terrains (e.g., at arrow).

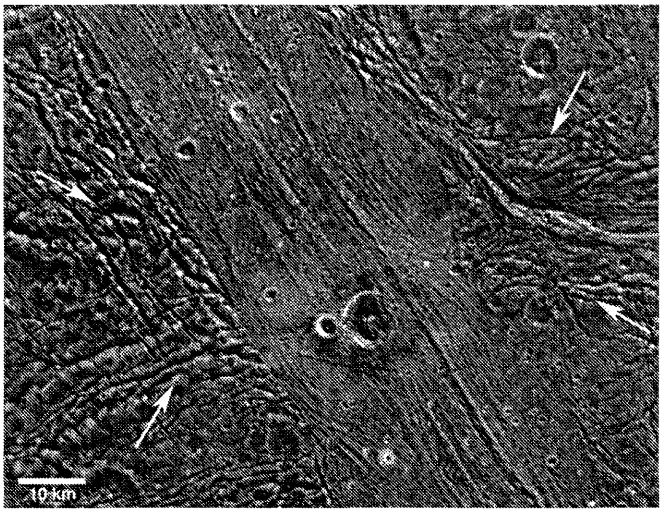

Figure 16.12. Bright grooved terrain of Byblus Sulcus trends NW–SE across dark terrain of Marius Regio, imaged at 86 m/pixel. Relatively young fractures in the dark terrain parallel the grooved terrain trend, suggesting a genetic relationship. Older broad (~30 km) furrows (with approximate lateral extents as marked with arrows) trend nearly orthogonally and have concentrated fine (kilometer scale) tectonic deformation within them. Smooth materials of Byblus Sulcus hint at icy volcanism, and an unusual 8 km crater within Byblus displays dark lobate ejecta surrounded by bright ejecta. *Galileo* observation G2GSGRVLNS01.

Figure 16.13. Idealized model for the topography and structure of grooved terrain. Small-scale ridges and troughs (typically ~1 to 2 km wavelength), potentially formed by tilt-block-style normal faulting, are superimposed on large-scale pinches and swells (typically ~8 km wavelength), which may be created by extensional necking of the lithosphere. The smallest scale ridges and troughs are located within pinched regions, suggesting finer-scale fault imbrication there. An especially deep trough marks the boundary between faulted and undeformed terrain (left), suggesting deformation of the hanging wall fault block above a prominent marginal fault. Dashed curve represents the brittle–ductile transition within the lithosphere at the time of grooved terrain formation. From Pappalardo *et al.* (1998a).

Bright Terrain Tectonism

Overall, high resolution *Galileo* images support an extensional tectonic model of grooved terrain formation. Important modifications to *Voyager*-based models are discussed in the following sections, including: multiple superimposed length scales of deformation, a significant role for tilt-block style normal faulting, locally high extensional strains, the potential for tectonism alone to cause resurfacing of some groove lanes through destruction of preexisting topography, an important role for strike-slip faulting, the possible occurrence of local lithospheric spreading, and a less prominent role for icy volcanism.

Styles of Extensional Tectonism. Grooved terrain within some polygons has a morphology resembling flat-floored graben and intervening flat-topped horst ridges. Examples are seen within Philus Sulcus (Figure 16.10) and at higher resolution within Uruk Sulcus (Figure 16.11a). Rather than downdropping along prominent and distinct bounding faults, offset has occurred by cumulative displacement along several of the sub-kilometer-scale fractures or

faults that are pervasive across these grooved terrains. In regions where horst-and-graben grooved terrain morphology occurs, typically the stratigraphically lower grooved terrain set shows this morphology, suggesting that this may have been the preferred morphology of older grooved terrains (Collins *et al.* 1998a, 1998c).

The more common morphology of grooved terrain is kilometer-scale blocks with ridges that appear to be triangular to rounded in cross-section. Intervening troughs are typically narrow and somewhat V-shaped in cross-section, as exemplified in Uruk Sulcus (Figures 16.8 and 16.11). This morphology – narrow triangular ridges and similarly shaped troughs with no topographic break in between – is suggestive of tilt-block-style normal faulting, where arrays of normal faults dip in the same direction and fault motion induces back tilting of the surface (Figure 16.12). This style of normal faulting is also called "bookshelf" or "domino-style" normal faulting because of the similarly to a set of tilted books or dominoes. Tilt-block normal faulting creates regularly spaced ridges and troughs, with the faulted layer thickness proportional to the fault spacing, based on terrestrial examples and sandbox experiments (Mandl 1987, Vendeville *et al.* 1987). Tilt blocks are most commonly asymmetric in cross-section, as recognized in some regions of grooved terrain. A good candidate for tilt-block morphology is also observed in dark terrain adjacent to a prominent bounding groove of Harpagia Sulcus (see Figure 16.18). Stratigraphically more recent grooved terrains tend to show this tilt-block-like morphology (Collins *et al.* 1998a, 1998c).

Boundary relationships give strong support to an extensional tectonic origin for grooved terrain. In Uruk Sulcus, incipient fractures immediately adjacent to the grooved terrain have a spacing similar to the grooved terrain structures (Figure 16.11, arrows), suggesting that grooved terrain has formed as fractures propagated into and imbricated preexisting terrain. Similarly, small-scale troughs in dark terrain commonly trend subparallel to sulcus boundaries suggesting a genetic relationship, as flanking Byblus Sulcus (Figure 16.13).

Extensional necking of Ganymede's lithosphere can explain the topography of groove sets dominated by tilt-block faulting (Collins *et al.* 1998b, Dombard and McKinnon 2001). Where ductile material underlies a brittle lithosphere and the decrease in viscosity with depth is rapid, an extensional necking instability can occur in which the stretched lithosphere evolves into a series of pinches and swells, as first modeled for the Basin and Range of the western United States (Fletcher and Hallet 1983). Initial application of this process to icy satellites suggested that it may not be applicable to the relatively warm surface of Ganymede (Herrick and Stevenson 1990). Subsequent modeling shows that this process can operate on Ganymede when the superplastic rheological behavior of ice is considered, for strain rates $\sim 10^{-16}$ to 10^{-14} s^{-1} and thermal gradients >10 K km^{-1} (heat fluxes >30 mW m^{-2}), implying a lithosphere locally ~ 1 to several kilometers thick at the time of stretching (Dombard and McKinnon 2001).

The extensional instability model can account for the long-wavelength (~ 8 km) ridges and troughs observed in *Voyager* images, and is consistent with the shallow slopes ($\leq 20°$, Squyres 1981, Giese *et al.* 1998) of these long-wavelength undulations. In this model, the finer-scale deformation revealed by high resolution *Galileo* imaging represents brittle faulting of the surface layer, with additional imbrication of these faults into a finer length scale in regions of greatest local strain (Figure 16.12) (Pappalardo *et al.* 1998a, Collins *et al.* 1998b, Patel *et al.* 1999). The model might also account for multiple pinch-and-swell wavelengths if generated and then stretched out as extension proceeds (Dombard and McKinnon 2001). The broadly similar dominant wavelengths of deformation across Ganymede suggest similar lithospheric properties across the satellite at the time of grooved terrain development, for extended regions in both bright and dark terrains (Grimm and Squyres 1985, Patel *et al.* 1999).

In model experiments and terrestrial rift zones, a deep trough commonly marks the edge of a rift zone, reflecting the presence of a prominent boundary fault and deformation of the downthrown (or hanging wall) fault block above the fault (Figure 16.12) (Hamblin 1965, McClay and Ellis 1987). This process is aided if the marginal fault has a listric, curved geometry. Prominent bounding faults and hanging wall deformation are commonly associated with terrestrial tilt-block domains, and could explain the prominent bounding troughs alongside some lanes of grooved terrain (Pappalardo *et al.* 1998a, Prockter *et al.* 2000).

As an illustration, hanging wall deformation may have been important in shaping Anshar Sulcus (Figure 16.14) (Prockter *et al.* 2000). It appears from *Voyager* images (Figure 16.14, inset) that bright volcanic material might have emerged from a prominent dark terrain furrow at the southeastern tip of Anshar (Murchie and Head 1988). High resolution *Galileo* images show that a prominent bounding groove runs along Anshar's southern border as a continuation of a prominent dark terrain furrow, while the northern boundary is less topographically distinct. The interior of the sulcus consists of blocks ~ 1 to 2 km in width that trend subparallel to the sulcus boundaries. These morphologies are suggestive of domino-style normal faulting above a prominent north-dipping fault that forms Anshar's southern margin. This is consistent with the observed transition from the dark terrain furrow if the furrow served as a detachment surface above which the sulcus faulting occurred. In the case of Anshar Sulcus, differences in structure seem to be key to the transition from dark to grooved terrain (Prockter *et al.* 2000).

Amount of Extension. Domino-style faulting implies a much higher degree of local extension than graben formation. The assumption that individual grooves are graben leads to estimates of the degree of extensional strain across grooved terrain of a few percent (Golombek 1982). In contrast, domino-style faulting is commonly associated with at least tens of percent of extensional strain (Wernicke and Burchfiel 1982). Based on the geometry of fault blocks seen in high resolution Uruk Sulcus images, a minimum extensional strain of $\sim 50\%$ was estimated by Collins *et al.* (1998b).

Strained craters offer valuable insight into the degree of extension across groove sets, suggesting that highly strained grooved terrain may be common (Pappalardo and Collins 2003). *Galileo* high resolution images reveal several oblong craters that are transected by sets of subparallel ridges and troughs oriented roughly orthogonal to the long axis of the crater, implying that these craters have been extensionally

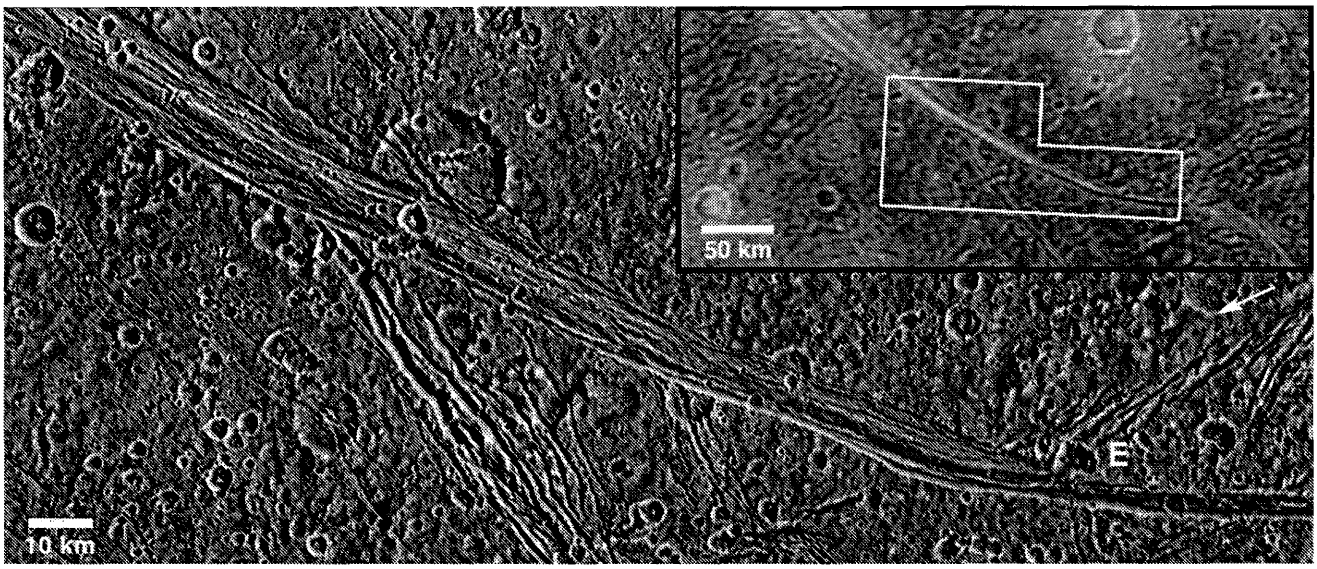

Figure 16.14. Anshar Sulcus appears as a lane of bright terrain against the dark terrain of Marius Regio in *Voyager* images (inset, 1 km/pixel), although this albedo heterogeneity is not apparent in the high resolution *Galileo* images (150 m/pixel, incidence angle 70°, phase angle 73°, *Galileo* observation G8GSANSHAR01). Grooved terrain faulting may have induced by deformation of the hanging wall fault block above a prominent NE-dipping normal fault *(Prockter et al.* 2000). A set of prominent echelon structures at E appears to have formed along older furrow structures (with northern margin and trend indicated by the arrow). North is to the top of the *Voyager* inset.

strained (Figure 16.15). The crater shapes suggest that normal faulting has extended them by amounts ranging from a few percent, for barely perceptible fractures (Figure 16.15d), to ~50% overall by a fault zone that has experienced >100% strain (Figure 16.15a). Of the strained craters identified and analyzed by Pappalardo and Collins (2003), only one (Figure 16.15c) is within what would be traditionally considered bright grooved terrain, and it has been strained by ~14%.

The maximum degree of areal expansion that could result from differentiation of Ganymede is ~6.5% (Squyres 1980b, Mueller and McKinnon 1988). Areal expansion from melting (dominated by high pressure ices) if the satellite is already differentiated is 2% (Showman *et al.* 1997). *Voyager*-based strain estimates seemed consistent with a ~1% limit on global expansion of Ganymede imposed by the large-scale coherence of dark terrain in *Galileo* Regio (McKinnon 1982). The greater strain implied by tilt-block-style normal faulting in both bright and dark terrains might invalidate the *Galileo* Regio observation as a global constraint (though it would still apply, *sensu stricto*, to global expansion). However, inferences regarding the total amount of strain implied by the global distribution of grooved terrain are confounded by the limited high resolution coverage of the satellite.

Tectonic Resurfacing. The high degree of strain in zones of tilt-block normal faulting suggests that preexisting surface features may be altered beyond recognition through a process termed tectonic resurfacing. Motivation for understanding this process was provided by *Galileo*'s first high resolution images in Uruk Sulcus(Figures 16.8 and 16.11, Head *et al.* 1997a). Regional evidence (Figure 16.2) had been cited for the volcanic flooding of rift zones in this area to produce the broad lanes of bright terrain and locally resurface polygons (Golombek and Allison 1981, Murchie *et al.* 1986, Guest *et al.* 1988), but there is no direct evidence for cryovolcanic activity in the limited high resolution Uruk Sulcus images (such as extrusive vents, lobate flow fronts, flooded and embayed terrain, or pyroclastic mantling). With the exception of a small smooth patch (S of Figure 16.11a), sequential and pervasive tectonic deformation dominates the surfaces of all units in the region as seen at high resolution. It is possible that icy volcanism might have occurred early in the region's evolution to brighten the terrain and create smooth materials (that ended up, e.g., as flat-topped horsts), but its later geological history is dominated by tectonism, which may have resurfaced newer groove lanes without associated icy volcanism.

As an example of the inferred tectonic resurfacing process, the relationships in Figure 16.11a suggest that grooved terrain of polygon (B) is younger and resurfaced by tectonic destruction of older grooved terrain of polygon (A). Polygon (A) is more heavily cratered and is cross-cut by structures of groove terrain at (B). In a transition zone a few km wide, cross-cutting faults subparallel to and which resemble those within grooved terrain (B) have progressively destroyed the linear texture of polygon (A, at arrow). Additional evidence for tectonic destruction of preexisting terrain is the truncation of a 6-km diameter crater (immediately south of C), where half of the crater has been erased, apparently by intense faulting associated with formation of grooved terrain of (B). These relationships suggest that grooved terrain of (B) is younger and resurfaced by tectonic destruction of older grooved terrain.

In a second example, a polygon of grooved terrain with internal structures that generally trend N–S (D of Figure 16.11b) is truncated at its southern margin by grooved terrain of (E). A narrow transition zone of faults at the boundary between these zones (arrow) suggests that terrain at (E) has formed tectonically at the expense of terrain at (D). The faulting has been so intense that the original texture of

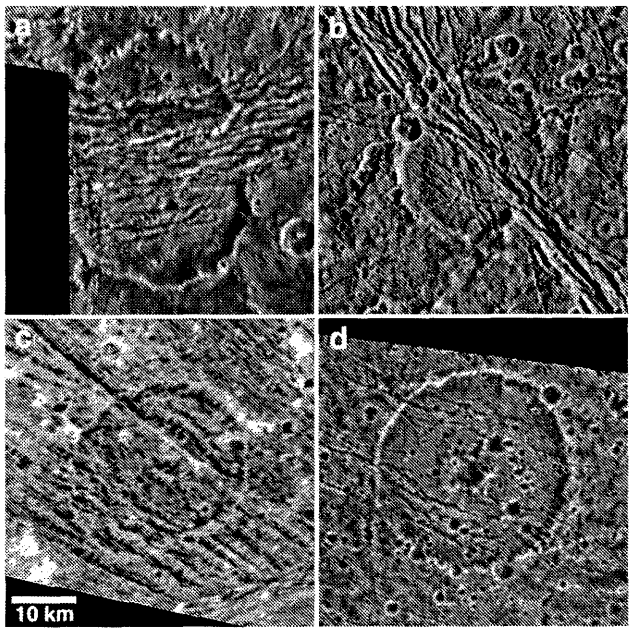

Figure 16.15. Examples of extensionally strained craters on Ganymede (Pappalardo and Collins 2003). (a) Saltu crater within the dark terrain of Nicholson Regio has experienced about 50% extensional strain, with a minor component of right-lateral shear. The extensional strain represented across the transecting zone of ridges and troughs alone is probably >100%. (b) An unnamed crater in Marius Regio near Anshar Sulcus has been elongated about 20% overall by two episodes of tectonism. (c) Nefertum crater within grooved terrain of Nun Sulci has been strained by about 14%, along with a component of right-lateral shear. (d) The minor fractures that cut Erichthonius crater near Erech Sulcus have extended it by only about 3%. From *Galileo* observations G7GSNICHOL01 (176 m/pixel), G8GSANSHAR01 (150 m/pixel), G7GSNUNSUL01 (164 m/pixel), and G8GSERECH (143 m/pixel), respectively.

terrain at (D) is unrecognizable within the newer grooved terrain unit. The rotational tilt-block-style faulting interpreted in unit (E) appears to be an important mechanism for tectonic resurfacing.

These examples show that tectonism alone can apparently resurface some grooved terrain units without requiring icy volcanism to erase preexisting terrain. However, the tectonic resurfacing hypothesis does not rule out volcanic resurfacing early in grooved terrain formation, to brighten the terrain overall and produce relatively smooth materials. For example, old craters are preserved on the horst-and-graben-like grooved terrain of polygon (A), implying that subsequent strains there have not been great enough to resurface this grooved polygon tectonically; instead, the smooth patch at (S) suggests that icy volcanism may have played an important role in shaping the early history of the region.

Support for the tectonic resurfacing endmember hypothesis is provided by extensionally strained craters (Figure 16.15), the majority of which are within dark terrain (Pappalardo and Collins 2003). Preexisting features within strained craters (such as central peaks or pits) are absent, suggesting that strains of a few tens of percent may render preexisting topography unrecognizable. Conclusions from heavily faulted dark terrain are presumed to be directly applicable to bright grooved terrain, given that lanes of subparallel ridges and troughs in both terrain types are morphologically similar, display similar topographic wavelengths of tectonic features, and experienced similar inferred heat flow during the time of their deformation (Patel *et al.* 1999, Dombard and McKinnon 2001, Pappalardo and Collins 2003). Although the limited high resolution coverage precludes definitive conclusions, and craters in bright terrain are generally less abundant, it is plausible that strained craters in bright terrain are uncommon in *Galileo* images because they have been deformed beyond recognition.

It is noteworthy that dark terrain which has undergone a high degree of tectonic deformation appears somewhat brighter than the surrounding terrain, despite there being no evidence for icy volcanism affecting the terrain (Figure 16.4). Moreover, the transition from some dark terrain to grooved terrain regions shows no direct evidence for icy volcanism, as in Anshar Sulcus (Figure 16.14) and in the groove lanes near Arbela Sulcus (Figure 16.4). It is intriguing to consider whether tectonism alone cannot just resurface older terrain, but brighten it as well. As discussed in Section 16.2.1, dark terrain probably consists of a thin dark lag above an icy substrate. Therefore, at least some brightening of initially dark terrain is expected where tilt-block faulting has occurred, revealing brighter icy material beneath, with loose dark material moving downslope into topographic lows (Figure 16.7b). Such a process may have occurred in rift zones within Nicholson Regio (Figure 16.4), and in Marius Regio where isolated fault-bounded blocks appear relatively bright (Pappalardo *et al.* 1997b). Some strike-slip fault zones are straddled by zones of smooth-appearing material (see Figure 16.16c), and some inferred strike-slip zones are expressed as smooth lanes, suggesting possible tectonic smoothing by progressive breakup of the surface (Collins *et al.* 2001). However, it remains to be demonstrated whether fine-scale faulting can effectively smooth and brighten preexisting terrain.

Strike-Slip Faulting. *Voyager* imaging suggests that strike-slip tectonism has operated on Ganymede, notably based on the sigmoidal shapes of some grooved terrain sets and candidate strike-slip offsets along major fault zones (Lucchitta 1980, Murchie and Head 1988, Pappalardo 1994). At higher resolutions, strong evidence is found for strike-slip displacement along some faults as well as for a component of distributed shear in forming grooved terrain.

En echelon fault segments are characteristic of strike-slip offsets. Left-stepping en echelon fault segments are expected to indicate right-lateral strike-slip motion, and vice-versa. Examples of en echelon offsets are common within grooved terrain, for example within Uruk Sulcus (Figure 16.16a) and Nun Sulci (Figure 16.16b) (Pappalardo *et al.* 1998a, Collins *et al.* 1998d, DeRemer and Pappalardo 2003).

Where a strike-slip fault bends, a sigmoidal shaped fault-bounded region is expected, with faults trending subparallel to the sigmoidal curvatures (Woodcock and Fisher 1986). Depending on the sense of strike-slip offset and the direction of the fault bend, regions of transtension (releasing bends, consisting of strike-slip plus extension) or transpression (restraining bends, consisting of strike-slip plus compression) will result. Fault-bounded sigmoidal regions are common within grooved terrain, suggesting a strike-slip

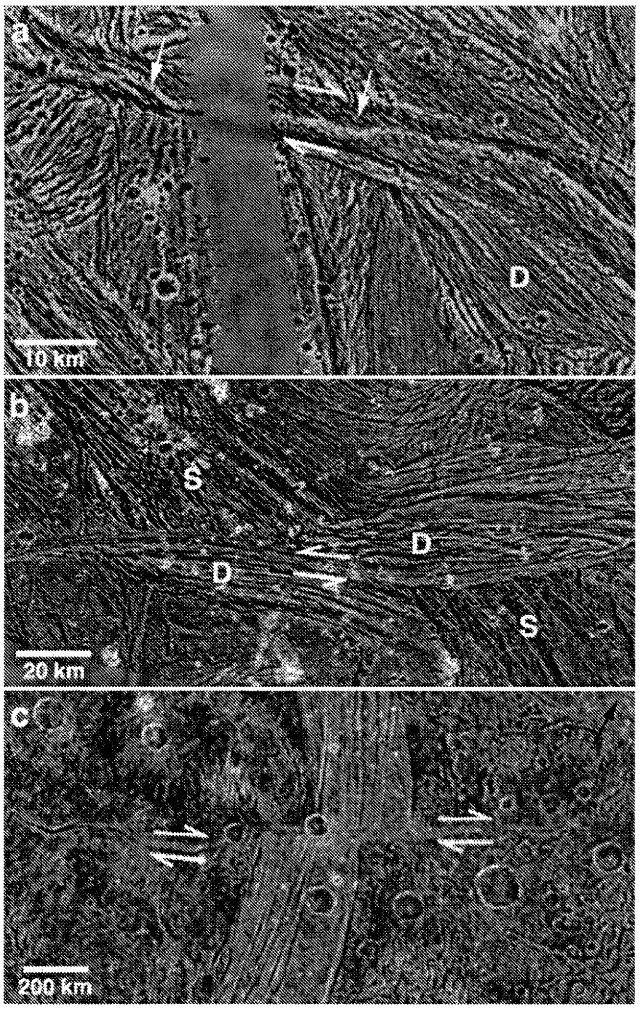

Figure 16.16. Examples of strike-slip tectonism on Ganymede. (a) In Uruk Sulcus, a right-lateral shear zone (half-arrows) ~7 to 10 km wide contains prominent en echelon structures (e.g., at arrows). A fault duplex D has formed in a releasing bend of this shear zone. (b) In Nun Sulci, an inferred left-lateral strike-slip fault (half-arrows) appears to have displaced preexisting sulci (S) (cf. Lucchitta 1980), implying that fault duplexes D formed along a constraining bend and are transpressional. (c) Dardanus Sulcus has been displaced ~150 km along a right-lateral fault, which exhibits bright material where it cuts dark terrain (e.g., at half-arrows); black arrow indicates north in this example. From *Galileo* observation G1GSURSUL01 (74 m/pixel) on *Voyager 2* context (1 km/pixel); *Galileo* observation G7GSNUNSUL01 (164 m/pixel), and *Galileo* observation 28GSDARDAN01 (750 m/pixel), respectively.

faulting component. For example, transtension is inferred within Uruk Sulcus (Figure 16.16a) at both the local and regional scales (Pappalardo *et al.* 1998a). The offset direction implied by en echelon segments in Nun Sulci (Figure 16.16b) suggests that transpression has occurred within one fault-bounded region (DeRemer and Pappalardo 2003). If so, the structures within represent scarce evidence for a compressional component of deformation. The apparent paucity of compressional or transpressional structures on Ganymede may indicate a globally dominant extensional stress environment during grooved terrain formation.

High resolution evidence for strike-slip motion lends credence to interpretations of apparent strike-slip offsets along major fault zones based on regional-scale images, as along eastern Tiamat Sulcus (Murchie and Head 1988, Patel *et al.* 1999), and offsetting Dardanus Sulcus (Figure 16.16c) (Smith *et al.* 1979b, Murchie and Head 1988). The pervasiveness of shear on Ganymede is supported by the regional context of strain indicators in several grooved terrain sites (Pappalardo *et al.* 1998a, Prockter *et al.* 2000, Collins *et al.* 1998d). For example, there is evidence of dextral shear near the boundary between Philus Sulcus and Marius Regio (Figure 16.9) (Head *et al.* 1997b), and fine-scale structures within dark terrain of Marius Regio may have served as shear planes. Analysis of strained craters also suggests that a component of distributed horizontal shear is common (Pappalardo and Collins 2003). Overall, modest amounts of strike-slip deformation appear to be an integral part of the grooved terrain formation process.

Lithospheric Spreading? At first quite controversial, lithospheric spreading is well documented on neighboring Europa (Schenk and McKinnon 1989, Sullivan *et al.* 1998, Prockter *et al.* 2002). A spreading-analog model for grooved terrain was originally suggested based on *Voyager* observations of central ridges and regions of apparent axial symmetry within grooved terrain (Lucchitta 1980). However, little evidence has been found for cut and separated older features or the large-scale horizontal shear expected to accompany lateral motion (McKinnon and Parmentier 1986). *Galileo* observations of a smooth portion of Arbela Sulcus reopen this issue.

The portion of Arbela Sulcus imaged by *Galileo* (Figure 16.4) presents the intriguing possibility that limited lithospheric spreading might have occurred on Ganymede (Head *et al.* 2002). When the smooth portion of Arbela Sulcus is digitally removed and older grooved terrains are aligned, the preexisting grooved terrains appear to reconstruct, and the missing terrain of Arbela closes with few small gaps and no overlap. If this reconstruction is correct, the smooth portion of Arbela Sulcus would have formed by ~25 km of lithospheric spreading and ~65 km of left-lateral shear. However, this reconstruction is not perfect, leaving conclusions regarding spreading of Arbela Sulcus and other "plank-like" lanes of smooth bright terrain (e.g., between Philus and Nippur Sulci, Figure 16.9) as ambiguous (Collins *et al.* 2001).

Rift-Flank Uplift. Based on their apparent, characteristic flexural shape, likely sites of flexural uplift alongside rift zones have been identified in stereo-derived topography, specifically alongside Harpagia Sulcus (see Figure 16.18) and bounding rifted dark terrain of Nicholson Regio (Nimmo *et al.* 2002). Flexural modeling suggests local heat fluxes ~30 to 45 mW m^{-2} during the time of deformation (Nimmo *et al.* 2002, Pappalardo *et al.* 2003), consistent with estimates based on models of extensional instability (Dombard and McKinnon 2001). Flexure of broad-scale topography seems to be a common characteristic of grooved terrains, but (as expected) small-scale ridge and trough topography does not appear to have been significantly affected by topographic relaxation.

Bright Terrain Volcanism

High resolution images have lacked clear and abundant morphological evidence for icy volcanism such as lava flow fronts, source vents, or embayment relationships. Such features may generally have been destroyed by fracturing, impact erosion, or mass wasting, may be too low in relief to be resolved, or perhaps did not form in volcanic terrains on Ganymede. Though the extent of volcanism in bright terrain formation remains somewhat enigmatic, indirect evidence for volcanic resurfacing of grooved terrain (Figure 16.7c) has been identified.

Eruption of liquid water through an ice-rich crust may seem a difficult prospect because of the negative buoyancy of the melt compared to the solid. Possible means of overcoming this difficulty are by the presence of contaminants within the ice crust to increase its relative density, by volatiles that exsolve with decreased pressure to decrease the density of a watery melt, or by pressurization of a crustal melt reservoir, for instance by partial crystallization (Fagents *et al.* 2000). Alternatively, warm ice might rise through the colder and denser crust to erupt in the solid state (Kirk and Stevenson 1987). Showman and Mosqueira (2001) suggest that topography could create subsurface pressure gradients that allow subsurface melt to move upward into topographic lows such as fault valleys. Such pressure gradients should wane as low areas fill, shutting off resurfacing before structural boundaries overflow and limiting embayment of surrounding topography, consistent with observed bright–dark terrain topography.

At least 18, and probably more than 30 scalloped depressions ("paterae") have been identified on Ganymede, and could represent caldera-like source vents for icy volcanism (Lucchitta 1980, Schenk and Moore 1995, Head *et al.* 1998, Kay and Head 1999, McKinnon *et al.* 2000, Spaun *et al.* 2001). High resolution *Galileo* images show that the largest patera of several within Sippar Sulcus (Figure 16.17) is associated with a ridged deposit, interpreted as an icy flow (Head *et al.* 1998). Stereo data show that its rim elevation reaches up to 800 meters above surrounding grooved terrain, with floor deposits of similar elevation to surrounding grooved terrain (Schenk *et al.* 2001). Preexisting grooves continue unmodified right up to patera rims, suggesting that elevated rims more likely formed through isostatic adjustment than constructional volcanism. Embayment relationships and truly smooth regions that might indicate icy volcanism have been elusive at high resolution. Some limited embayment is suggested in the Sippar Sulcus region (Head *et al.* 1998, Schenk *et al.* 2001).

Schenk *et al.* (2001) report that the smooth terrain in central Sippar Sulcus (Figure 16.17) exhibits topographic characteristics consistent with icy volcanic resurfacing. Using topography derived from *Voyager–Galileo* stereo pairs, they find relatively smooth terrains that lie at roughly constant elevations over great longitudinal extent and are depressed 250 to 1000 meters below surrounding terrains. These topographic data are consistent with flooding of structural troughs to an equipotential level by low-viscosity aqueous lavas to form the smooth terrains. Schenk *et al.* (2001) adopt a model in which graben are flooded by aqueous lavas (cf. Figure 16.7c) and then tectonized by groove formation until they are unrecognizable, with only the youngest smooth bands escaping tectonization. Byblus Sulcus (Figure 16.13) is another example of a relatively smooth lane of grooved terrain.

Probably the smoothest area identified at high resolution is within Harpagia Sulcus near its boundary with Nicholson Regio (Figure 16.18). Images and stereo-derived topography show patches of linear, parallel scarps with ~200 m of local topographic relief (Giese *et al.* 2001), presumably tectonic in origin. However, elsewhere in the region are patches of smooth level terrain up to ~10 km across that are disturbed only by small craters. It is difficult to reconcile these smooth patches with modification by tectonism alone. In principle, smooth level plains on airless planetary surfaces might be produced by paroxysmal landform degradation such as catastrophically disruptive seismic shaking, but there do not appear to be surrounding zones of less intense destruction or analogous features elsewhere on Ganymede to support such a model. The presence of morphologically pristine impact craters on this smooth terrain implies that the substrate is mechanically capable of supporting topography, disfavoring a hypothesis that the terrain is smooth because it is composed of loose, relatively incoherent particles. A reasonable conclusion is that these low-relief patches are examples of plains emplaced by low-viscosity icy volcanic flows.

Virtually all smooth bright terrains on Ganymede exhibit some degree of tectonic overprinting. As one of the smoothest terrains observed in *Voyager* images, another portion of Harpagia Sulcus was the target of 15 m/pixel *Galileo* imaging (Figure 16.19). The area appears very smooth in *Galileo* regional resolution images (Figure 16.19, inset), but is very rough at the scale of hundreds of meters, containing many degraded linear ridge segments inferred to be tectonic in origin. Although no definitive evidence for icy volcanic landforms is observed here, volcanic embayment is a plausible origin for the relatively smooth material between individual ridges (Head *et al.* 2002). These images suggest that volcanism on Ganymede may occur on a very fine scale, intimately associated with tectonism. The apparent intimate association of tectonism and volcanism suggests that icy volcanic extrusions and tectonic extension operate in concert. The search for pristine and unambiguous icy volcanic landforms may be frustrated by near-simultaneous tectonism which has in most instances modified them.

Bright Terrain Exogenic Processes

Mass wasting acts at a fine scale to smooth and level the topography of grooved terrain. High resolution imaging, including stereo (Figure 16.8), indicates that dark streaks occur on steep slopes and are oriented downhill, representing mass movements. Low albedo material within topographic lows may be further evidence of downslope movement, with thermal segregation induced by sublimation probably contributing to concentration of dark material in topographic lows (Spencer *et al.* 1998). As discussed above for dark terrain, sputter ablation likely plays some role in the evolution of Ganymede's debris layers (Cooper *et al.* 2001), but outside of the polar regions at least, sputtering is probably less important than mass wasting and thermal segregation (Moore *et al.* 1999).

The very highest resolution (11 m/pixel) images of

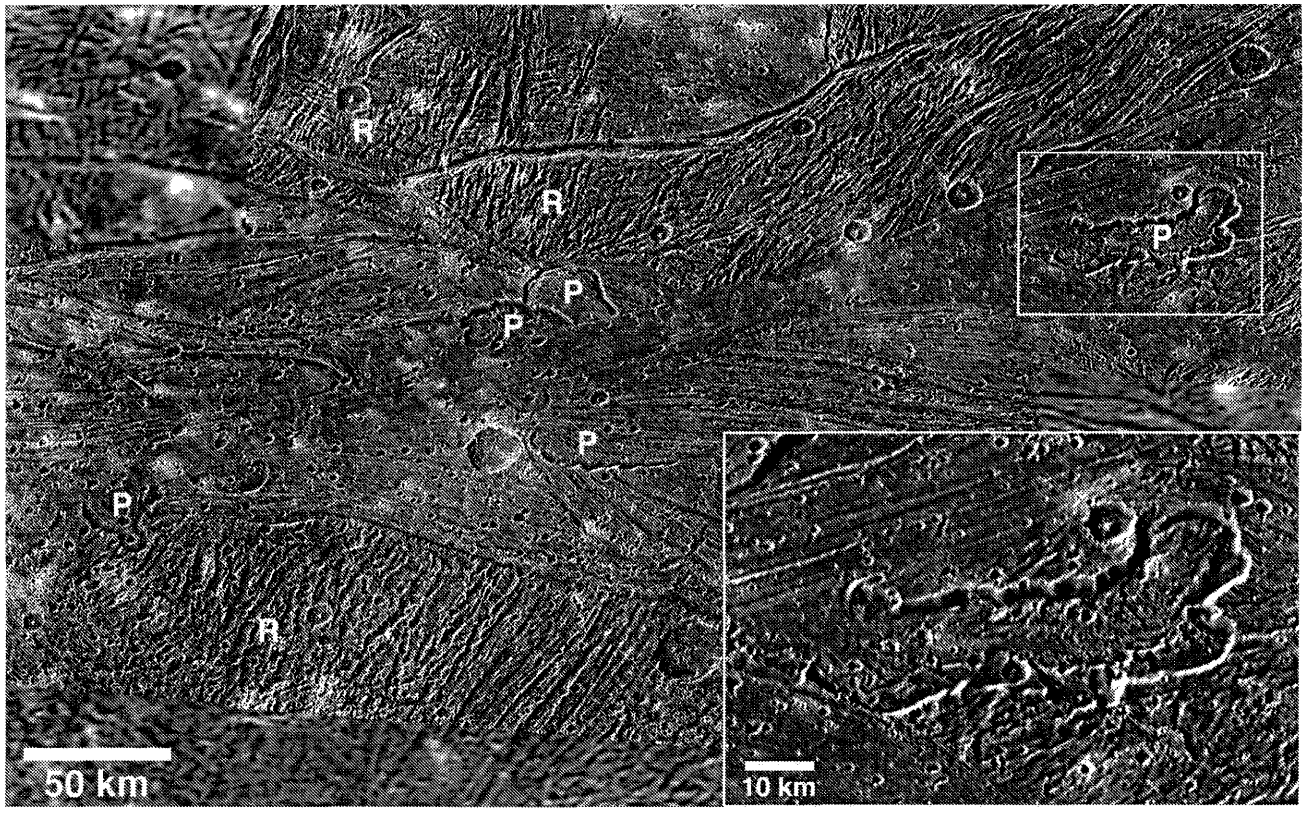

Figure 16.17. A portion of Sippar Sulcus rich in scalloped depressions (paterae, marked P), as first discussed by Lucchitta (1980). The most prominent patera (inset) displays surface texture that may be indicative of flow toward its open end, consistent with it being a source region for icy volcanic material. Some tectonic structures in the region cross each other near-orthogonally, forming reticulate terrains (marked R). Here south is to the top. From *Galileo* observation G8GSCALDRA01 (180 m/pixel).

Ganymede were acquired near 30°N, 90°W in (or near) Xibalba Sulcus during orbit G1 (Figure 16.20). Unfortunately, the imaged area contained unexpectedly bright slopes that were overexposed and thus saturated portions of the camera's CCD, producing pixel bleed that obscures portions of the images (nor is the exact location clear, or a useful context image available). Nevertheless, several possible examples of mass movement and landform modification are recognizable (Yingst *et al.* 1997, Moore *et al.* 1999). Almost nowhere is the surface found to be smooth at this high resolution. Slopes are usually less than ~10°, although in a few instances they approach ~20°, suggesting eroded massifs. The surface between the hills is generally undulatory with a rough texture suggestive of erosional hummocks or block or boulder clusters. Some craters in the region appear partially infilled by debris. Candidate talus slopes are recognized in light scattered from adjacent bright hills into shadows, where superimposed "dark" streaks, with locations and organization that appears to be controlled by the local topographic gradient, are interpreted as loose material that has moved downslope.

16.2.3 Polar Caps

Voyager observations showed continuous diffuse, bright deposits without relief poleward of about ±40° latitude, known as the polar caps or hoods (Smith *et al.* 1979b). Several hypotheses have been proposed to account for the presence of the polar caps. Water-frost deposits may simply remain longer in the colder environment of the high latitudes (Squyres 1980a), or frosts may accumulate at high latitude by cold-trapping of water ice ablated by solar radiation (Purves and Pilcher 1980, Spencer 1987b). The caps might be a relict deposit formed during the emplacement of light terrain materials (Shaya and Pilcher 1984), or may be a sink for ices which sublimate preferentially from the equatorial regions (Moore *et al.* 1996). Accumulation may be through cold-trapping of water ice bombarded by the jovian radiation belts (Sieveka and Johnson 1982, Johnson 1985). Hillier *et al.* (1996) support this model based on their analyses showing that the caps are very thin at their boundaries and increase in integrated thickness toward the poles. Moreover, the higher single scattering albedo and forward-scattering properties of the polar regions are consistent with sputter redistribution of ice there.

High resolution *Galileo* observations show that the surface at high latitudes has a dominantly bright mottled appearance (Figure 16.9). The patchy appearance and significant albedo variations suggest strong heterogeneity in the distribution and thickness of the polar frost deposits, with a preferential occurrence on pole facing slopes. Muting of some crater topography by bright deposits suggests that local thickness may be measured in terms of meters or more (Pappalardo *et al.* 1997a). The overall brightening of the polar hood is inferred to be the integrated effect of these bright mantling deposits.

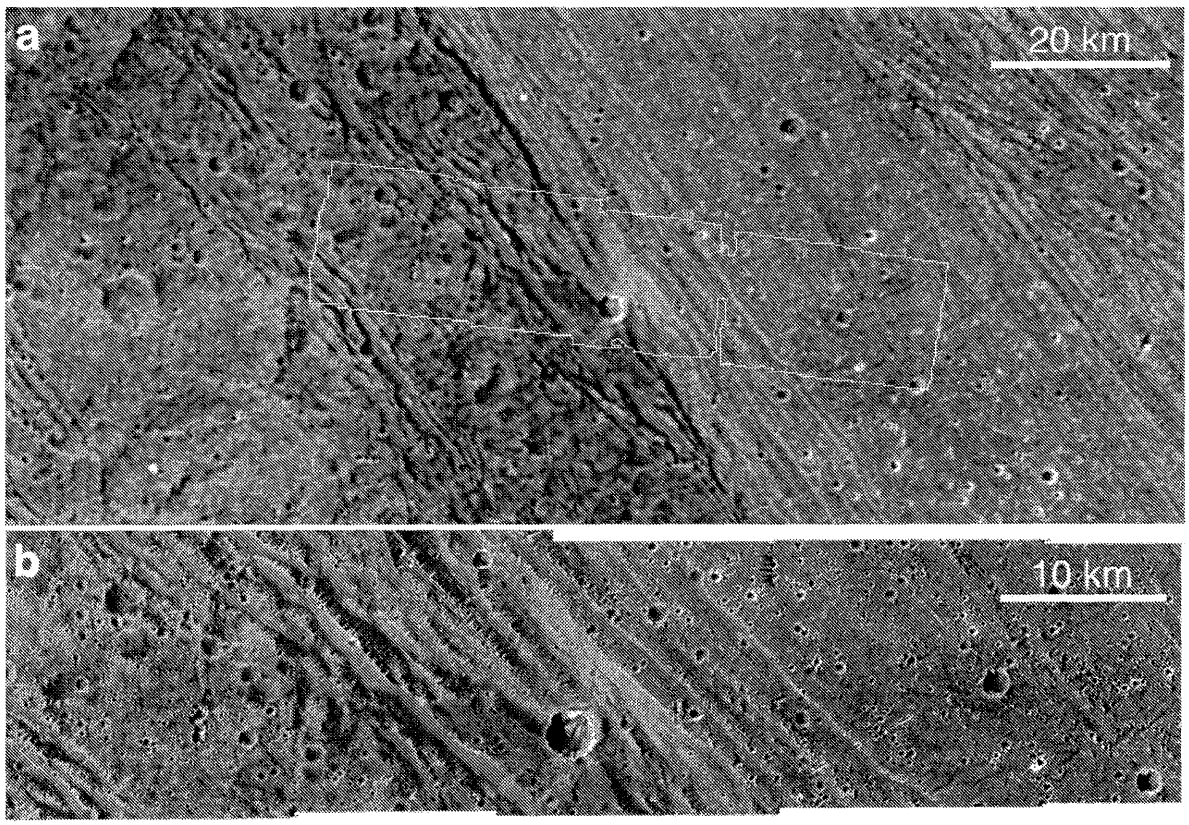

Figure 16.18. Margin between bright terrain of Harpagia Sulcus, and dark terrain of Nicholson Regio. (a) Contextual view (121 m/pixel; 28BRTDRK02), and (b) high resolution (20 m/pixel; 28BRTDRK02) images show that the bright terrain of Harpagia is very smooth, with limited tectonic deformation. A progression of domino faults is inferred in dark terrain near the margin. Stereo data demonstrate that a deep bounding trough and an adjacent topographic high (inferred to be flexural in origin) occurs within the bright terrain (Giese *et al.* 2001, Nimmo *et al.* 2002). North is to the top of the context image. At the time of going to press a colour version of this figure was available for download from http://www.cambridge.org/9780521035453 that includes an overlay of the stereo-based topographic data.

Ganymede's magnetic field deflects most charged particles in the satellite's equatorial regions but funnels plasma onto the polar regions (Kivelson *et al.* 1998, Chapter 21). The polar cap margins coincide with the boundary between field lines that are open to polar plasma and field lines that are closed to plasma, suggesting a possible causal relationship (Kivelson *et al.* 1998, Pappalardo *et al.* 1998b). Johnson (1997) suggests that bombarding plasma damages ice grains and thus brightens the polar caps. Instead or in addition, sputtering by charged particles may redistribute polar ice, with thermal segregation acting to create the patchiness and topographic muting observed in high resolution *Galileo* images.

16.2.4 Impact Structures

Ganymede displays the greatest diversity of primary impact morphologies in the solar system on one planetary surface (Figure 16.21), many of which are unique to Ganymede and its sibling Callisto. As reviewed by Schenk *et al.* (Chapter 18), these include: bright ray, dark ray, and dark floor craters (Figures 16.21a and 16.21b), pedestal craters (Figure 16.21c); craters with central pits and domes (Figures 16.21d and 16.21e); the low-relief ancient impact scars called palimpsests (Figure 16.22); and vast multi-ring structures expressed as sub-concentric furrows (Figure 16.2), interpreted to form by impact into a very thin elastic lithosphere (McKinnon and Melosh 1980).

Large crater studies combined with stratigraphic analyses indicate that the morphology of large craters (diameters >60 km) has undergone distinct changes through time (Chapter 18). Palimpsests (Figure 16.22) are the oldest known crater type, and predate bright terrain. They and the similar penepalimpsests (some of which formed during the epoch of bright terrain resurfacing and have more pronounced basin-like morphology) are circular albedo features with muted or barely visible concentric structures. Subsequent large impact morphology is characterized by the formation of bright central domes (Figure 16.21e), presumed to be exposures of Ganymede's shallow interior (Moore and Malin 1988). High resolution observations imply that central domes formed as a result of uplift in the center of the crater of relatively ductile material from depth (Schenk 1993, Chapter 18).

Palimpsests (up to 100s of kilometers in diameter) are recognized against dark terrain as low-relief bright patches (Figure 16.22). The details of palimpsest formation have been uncertain since the first *Voyager* observations. It has been suggested that the outer zones are a volcanic deposit extruded after impact (Thomas and Squyres 1990); how-

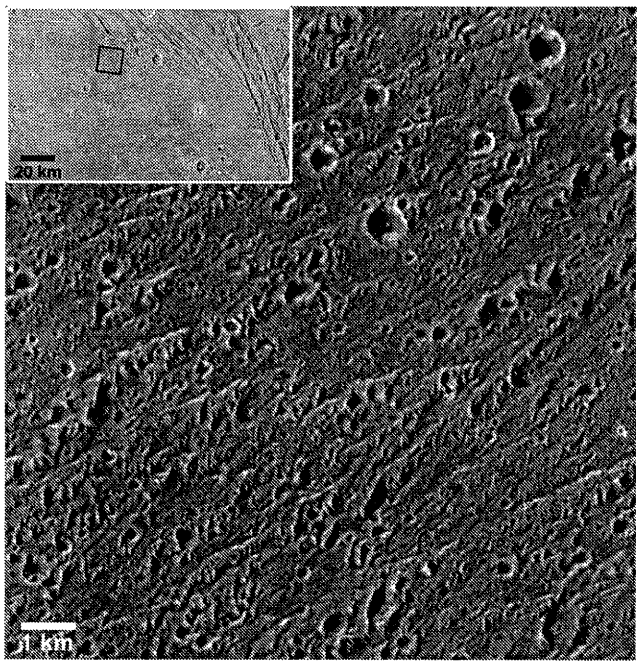

Figure 16.19. Bright terrain within Harpagia Sulcus appears very smooth in *Galileo* 119 m/pixel contextual images (inset; observation 28GSSMOOTH02). Small-scale features with significant topographic relief are revealed at very high resolution (15 m/pixel; observation 28GSSMOOTH01). This demonstrates that at least some of Ganymede's smoothest bright areas have undergone tectonic deformation at a very fine scale. Relatively smooth material between these small ridges was plausibly emplaced by icy volcanism. North is toward the top in the inset contextual image.

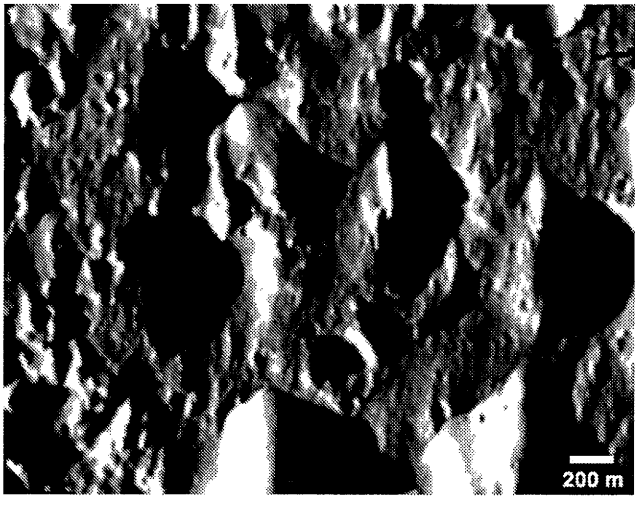

Figure 16.20. The highest resolution images obtained at Ganymede (11 m/pixel), with very low illumination from the west (83° incidence angle), reveal massifs and undulatory intervening plains. Image saturation has caused downward "bleeding" in some locations. From *Galileo* observation G1GSSULCUS01.

ever, the circularity of these features and the similarity in scaling of their radial components to conventional impact craters argues against this interpretation (Jones *et al.* 2003). The two most likely models suggest that the outer portions of the bright deposit are ejecta facies (Jones *et al.* 2003, Chapter 18). Jones *et al.* (2003) link morphologic units and stratigraphy among the four palimpsests observed at high resolution by *Galileo*, concluding that the bright material of palimpsests represents the entire continuous ejecta deposit of the impact structure. In contrast, Schenk and Ridolf (2002) argue, based on ejecta scaling of younger penepalimpsests imaged by *Voyager*, that the outer edge of the bright palimpsest deposit represents the edge of a pedestal-like ejecta deposit (analogous to the raised ejecta of pedestal craters; Figure 16.21c and see Chapter 18). The correct model is important for understanding origins and geophysical implications of palimpsests, and for determining the size distribution of these ancient impacts.

From *Voyager* images it was suggested that the subdued character of Ganymede's oldest impact structures, notably its palimpsests, imply a steep thermal gradient in Ganymede's early history, with more recent impact structures reflecting a thicker and stiffer elastic lithosphere (Passey and Shoemaker 1982, Shoemaker *et al.* 1982). This picture remains largely intact today, although our understanding of specific impact features and their origins has changed with the advent of reliable shape measurements (Schenk 1991, 1993), improved ice flow laws (Durham *et al.* 1997, Goldsby and Kohlstedt 2001), and high resolution *Galileo* images of representative impact features. The *Voyager*-based paradigm suggested that large craters were unable to retain their topography in an icy lithosphere over geological time, so viscous relaxation was inferred as the driving force for evolution of crater morphology (Passey and Shoemaker 1982). However, more recent studies show that craters can retain their topography for realistic ice flow laws and low-enough thermal gradients (Dombard and McKinnon 2000, Dombard 2000). Differences in large crater morphology with time may be consistent with impact features formed by impact into a lithosphere that evolved over time, rather than relaxation of old craterforms that originally resembled those created more recently (Chapter 18). Either interpretation indicates a much warmer shallow subsurface early in Ganymede's history than at present.

Impact craters on Ganymede can have bright, presumably ice-rich impact ejecta (e.g., Figures 16.2 and 16.21a), or dark, presumably less icy ejecta (Figure 21b). Dark ray craters seem to represent a phenomenon unique to Ganymede. Hartmann (1980) suggested that dark ray craters are indicative of subsurface chondritic silicates exposed by impacts, but this conclusion was based on the assumption that these craters only form in dark terrain and have a minimum size, suggesting penetration to a sublayer. More detailed mapping of dark ray crater sizes and distribution showed they are unrelated to terrain type (Conca 1981) but are distributed near the equator preferentially on the trailing hemisphere (Schenk and McKinnon 1991). This led to the conclusion that the rays are a lag deposit enriched in projectile material, concentrated by sublimation and charged particle bombardment on the trailing hemisphere but disrupted by micrometeorite bombardment on the leading hemisphere. The discovery of a magnetic field at

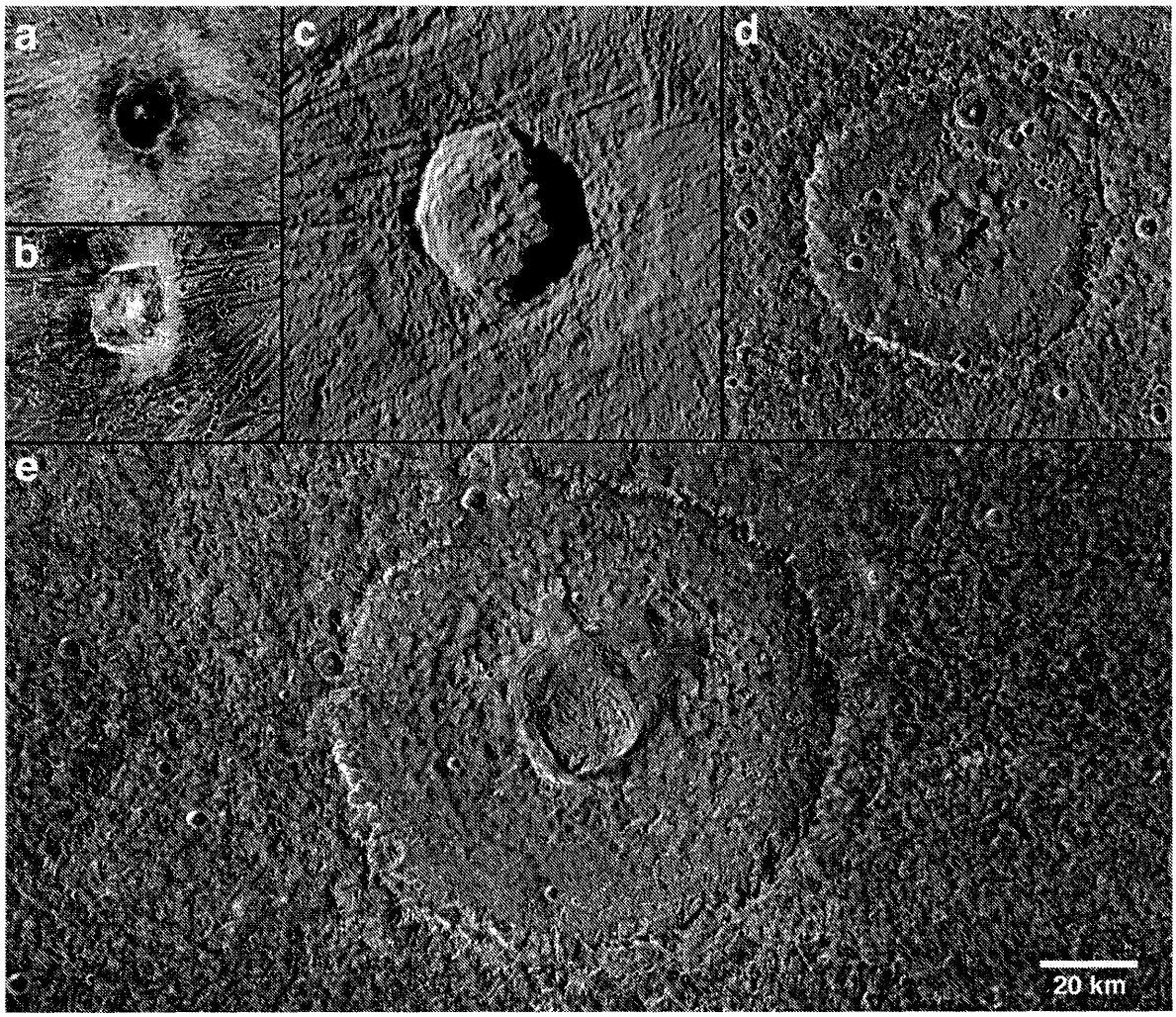

Figure 16.21. Examples of crater types on Ganymede, shown to a common scale. (a) Dark floor crater Khensu, with surrounding bright ejecta (219 m/pixel; G2GSCRATER01). (b) The rays of dark ray crater Kittu are subdued in this high resolution view (145 m/pixel; G7GSKITTU_01). (c) Pedestal crater Achelous shows characteristic outward-facing low ejecta scarp (175 m/pixel; G7GSACHELS01). (d) Central pit crater Lugalmeslam, situated on the southwestern margin of Nippur Sulcus (146 m/pixel; G8GSPITCRA01). (e) Central dome crater Melkart, on the boundary between dark terrain of Marius Regio (to the northeast) and bright terrain (176 m/pixel; G8GSMELKRT01).

Ganymede suggests that charged particle bombardment in equatorial regions may not be as important a process as previously believed (Cooper *et al.* 2001). Radiolytic effects are seen, however (Section 16.3.4) and the strength and character of the magnetic field may have varied over time. From color analyses, Schenk and McKinnon (1991) conclude that at least some dark ray craters represent impactor contamination. They find that the dark ray material of Kittu crater (Figure 16.21b) has a spectrum that is flat in the visible, consistent with C-type material from an impactor, rather than showing a red slope like other dark ray craters, which are a better match to D-type asteroids. This result is supported by *Galileo* NIMS data (Hibbitts *et al.* 2003a).

Dark floor craters are widely distributed over Ganymede's dark and bright terrains. Small (kilometer scale), fresh-appearing impact craters with low-albedo floor deposits are conspicuous in high resolution *Galileo* images (Figure 16.8), and larger analogs (typically ten or more kilometers in size) are apparent in regional-scale images (Figures 16.2 and 16.21a). Dark floor deposits have the lowest albedos of any features on Ganymede (Helfenstein 1986a, 1986b, Schenk and McKinnon 1991, Helfenstein *et al.* 1997a). Two viable hypotheses for the origin of dark floor deposits are as concentrated deposits of dark impactor material (Helfenstein 1986a, 1986b), or as impact melt from which the volatile icy constituents were lost due to vaporization (Schenk and McKinnon 1991).

Differences in crater density can permit the age of various terrains to be constrained. Issues pertinent to deriving relative and absolute age from Ganymede's impact craters are detailed in Chapter 18.

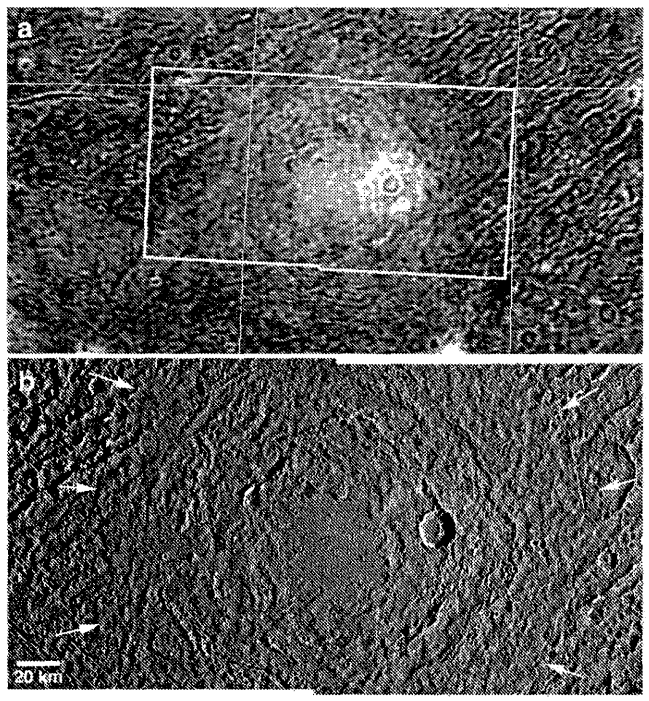

Figure 16.22. Buto Facula is a palimpsest within Marius Regio (12° N, 203° W). (a) Low incidence angle *Voyager 1* image at 1.3 km/pixel (FDS 20635.45) shows Buto as an albedo feature with no obvious relief. (b) *Galileo* images (180 m/pixel, incidence angle ~80°) show basin-like structure within Buto. The bright palimpsest margin corresponds to once-fluid ejecta (arrows), but there is disagreement as to whether this represents a pedestal-like ejecta deposit (Chapter 18) or the outer edge of the more extensive continuous ejecta blanket (Jones *et al.* 2003). *Galileo* observation G8GSBUTOFC01. North is to the top of the *Voyager* contextual image.

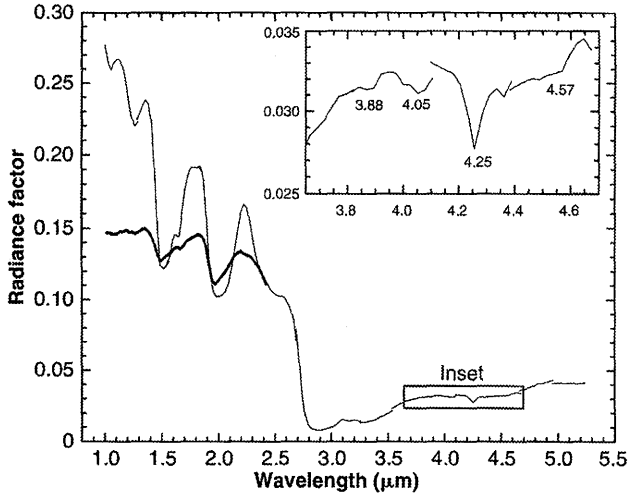

Figure 16.23. NIMS spectra of Ganymede. Thin curve is an average of 3000 pixels from a global observation covering 110° to 230° W. The strong absorption near 3 μm is the fundamental O–H stretching transition active in water ice and in hydrated and hydroxylated minerals; other bands evident in the 1 to 3 μm region are due to combination and overtone transitions in water ice. Bold spectrum is for a dark terrain region near 3° N, 274° W with ice absorptions removed, revealing asymmetric absorption bands characteristic of hydrated minerals. Inset shows details of absorptions inferred to be from minor constituents S–H (3.88 μm), SO_2 (4.05 μm), CO_2 (4.25 μm), and organic materials such as those containing C≡N (4.57 μm). After McCord *et al.* (1997, 2001a).

16.3 SURFACE COMPOSITION

16.3.1 Introduction

Ganymede shows a great deal of geological heterogeneity, yet until recently there was no obvious spectral evidence of major non-ice constituent materials. Many of the same statements regarding the early knowledge of Europa's surface, discussed in the "Surface Properties" section of Chapter 15, apply to Ganymede as well. The general impression from this early work was that the surface was mostly covered by water ice but that a very small amount of non-ice material is also present (e.g., Clark *et al.* 1986). The spectral characteristics of Ganymede's surface were reported to be intermediate between those of Europa and Callisto (Johnson *et al.* 1983) and to suggest, based on characteristics shortward of 3 μm, the presence of water ice in the grain size range of 0.1 to 1 mm. The band depths of the water-ice features were said to suggest larger grains on the trailing hemisphere. Unidentified non-water-ice absorption features were reported at 3.5 and 3.65 μm, but the low 3-μm albedo suggested few ice-free regions (cf. Calvin *et al.* 1995).

Recently, the *Galileo* spacecraft greatly improved our understanding of Ganymede's surface. In particular, the NIMS and UVS spectrometers have provided direct evidence of major and minor species. Moreover, the SSI camera has suggested links between compositional information and surface geology. Although some of the *Galileo* data have not yet been analyzed in detail, much has been learned and is summarized here.

16.3.2 Ice

Early ground-based spectroscopic observations, specifically infrared reflectance spectra, provided evidence of water ice as the major constituent of the surfaces of the three icy Galilean satellites (Europa, Ganymede, and Callisto) (see Calvin *et al.* 1995 and McCord *et al.* 1998a for reviews). This water ice is probably the result of thermal processing of water and water-bearing material that originally formed the satellites. H_2O molecules show strong, characteristic absorptions in the 1- to 3-μm spectral region, in particular near 1.4, 1.9, and 2.8 μm, but also in the 3- to 5-μm region. These absorptions vary in strength depending on abundance, particle size, and degree of crystallinity (see McCord *et al.* 1999 and Figure 15.3).

From the spatially resolved *Galileo* observations, the water-ice spectral signature on Ganymede (Figure 16.23) is seen to be particularly concentrated at the poles and away from the trailing side, and both amorphous (predominant at the poles) and crystalline forms are evident (Hansen and McCord 2000, 2003, Hansen 2002). Grain sizes have be estimated (to <10%) through modeling of ice absorption band shapes and depths (Hansen and McCord 2003). The trailing equatorial region shows evidence of mostly large-grained (>300 μm) ice. The leading side spectrum is dominated by the fine-grained deposits (20 to 50 μm) in the Osiris region,

but typical bright and dark regions are at most only a little finer grained on the leading side compared to the trailing side. The trend towards larger grain sizes on the low latitude trailing side is consistent with increased sputtering preferentially removing ice from the trailing side and the water molecules redepositing as a frost elsewhere, especially at colder sites such as the poles and colder higher-albedo areas.

Modeling of Ganymede ice spectra suggests that the surface in at least equatorial and mid-latitudes is made up of discrete patches of non-ice and ice material, i.e., there is no or little intimate mixing that would lead to multi-scattering (McCord *et al.* 2001a). The patches may be due to an uneven surface temperature distribution, resulting in uneven cold-trapping of H_2O molecules (Spencer 1987b), and/or to down-slope movement of dark material (Section 16.2).

16.3.3 Dark Material

Evidence for some unidentified non-ice component of Ganymede's surface was reported from early telescopic spectroscopic observations, but was considered by many investigators to be present only in very small amounts. Dark and light markings on the surface, observed by the *Voyager* and *Galileo* imaging systems, suggest a component other than ice on the surface. Ganymede's trailing hemisphere is darker than its leading side, presumably indicating more non-ice contaminant there. The spectral evidence for such material is difficult to discern in the infrared, however, due to strong water-ice absorptions that can hide the spectral signatures of other materials, especially in the 3 to 5-μm region.

Analysis of the *Galileo* NIMS data (Hansen *et al.* 1998, McCord *et al.* 2001a) suggests that there is considerable and widespread non-ice material on and in the surface of Ganymede (Figure 16.23). For example, it was once thought that the 2.7-μm drop-off in the reflectance spectrum was caused by water ice on Ganymede (or Callisto), but spatially resolved NIMS spectra show it is more likely due to a hydroxylated/hydrated mineral that is abundant on Ganymede at an average level of ~40 to 50% in equatorial and mid-latitudes. Ice abundance maps (Hansen 2002) indicate that there are many regions with >80% non-ice dark materials (in this interpretation, the same dark contaminant referred to in Section 16.2), consistent with photometric studies. The thermal evolution of Ganymede, leading to differentiation and migration of water toward the surface, would produce hydrated minerals as water circulates through and leaches ions from the satellite's interior materials, as is predicted by thermal modeling and meteoritic leaching experiments (Fanale *et al.* 1977, Kargel 1991, Kargel *et al.* 2000, Fanale *et al.* 1998, Zolotov and Shock 2001), and may be evident on Europa's surface (Chapter 15).

McCord *et al.* (2001a) analyzed several of the water absorption bands in the NIMS spectra looking for effects of non-ice materials on Ganymede. The wavelength positions and band shapes of the strong water absorptions, especially near 1.5 and 2 μm, differ from those of pure water ice if H_2O is bound in a hydrated mineral, and they vary depending on the particular mineral, the bonding configurations, the number of waters of hydration involved, and temperature (McCord *et al.* 1998b, 1999, 2001b, 2002). At least some regions of Ganymede's non-ice dark material are found to exhibit water absorptions near 1.4 and 1.9 μm, indicative of hydrated minerals (bold curve of Figure 16.23) (McCord *et al.* 2001a, Hansen and McCord 2003). McCord *et al.* (2001a) pointed out that the water of hydration absorptions on Ganymede for at least several locations are identical in both shape and wavelength position to those on Europa, within the precision of the measurements. This is evidence of similar hydrated materials on both satellites, with the Ganymede material perhaps being less hydrated. McCord *et al.* (1998b, 1999, 2001b, 2002) have suggested $MgSO_4$ hydrate as a likely candidate for a majority of the hydrated mineral on Europa, and a plausible hypothesis is that similar brines or deposits formed from brines reached the surface on Ganymede at some time in the past (McCord *et al.* 2001a). Interpretation of results from the *Galileo* magnetometer investigation implies a conducting water-rich layer deep beneath the surface of Ganymede today (Kivelson *et al.* 2002), and thermal modeling suggests that such a layer would have been at significantly shallower depth in the past (Chapter 13), in which case the hydrated materials at Ganymede's surface may provide a sample of Ganymede's briny ocean. Chapter 20 discusses an additional source of hydrated material, sulfuric acid hydrate, potentially formed by exogenic processes involving radiation chemistry on sulfur and sulfate ions on Ganymede's surface.

16.3.4 Other Molecules

In addition to the surface materials present in major quantities, there are molecular species present in smaller quantities on and in the near surface layer. Some of these may be indigenous but some are due to chemistry stimulated by Jupiter magnetosphere particulate radiation and perhaps from solar UV radiation. Sulfur compounds are suggested by the spectral slope through the visible (Calvin *et al.* 1995). Sulfur compounds might have an endogenic origin, or an exogenic origin related to implantation of magnetospheric material from Io.

Ground-based and Earth-orbital telescopic observations have revealed the presence of oxygen in several forms, including ozone (O_3) by Nelson *et al.* (1987) and Noll *et al.* (1996). Subsequently, Spencer *et al.* (1995) reported diatomic oxygen (O_2), with strongest concentrations on the trailing side, from groundbased visible spectroscopy. These workers suggest that O_2 has a liquid-like spectrum because it is trapped in the ice surface and the molecules are close enough together for simultaneous electronic transitions. In contrast, Vidal *et al.* (1997) suggest that O_2 is condensed within a cold atmospheric haze during the Ganymede night. The concentration of the oxygen on the trailing side suggests an association with the particle radiation trapped in the Jupiter magnetic field, perhaps implantation of oxygen ions or radiolysis of ice (Calvin *et al.* 1996). The radiolysis hypothesis is consistent with the escape of hydrogen from Ganymede inferred from *Galileo* plasma measurements (Frank *et al.* 1997), and Earth-based telescopic observations of Lyman-α and oxygen airglow (Chapter 19). The *Galileo* UVS provided evidence for ozone at the polar regions and near sunrise and sunset at low latitudes, as well as evidence for hydrogen peroxide (Hendrix *et al.* 1999a,b).

The *Galileo* NIMS indicates the presence of CO_2 in the nature of a strong 4.26-μm absorption on Ganymede (and Callisto), as seen in Figure 16.23 (inset) (McCord *et al.* 1997, 1998a, Hibbitts *et al.* 2000, 2003b). The CO_2 is inferred to be present in very small (~100 molecule) clusters probably in inclusions, and it is widely distributed in very complex patterns. Hibbitts *et al.* (2003b) analyzed in detail the CO_2 absorption and its distribution for Ganymede. They find that, in general, bright terrain contains less CO_2 than dark terrain, there is little or no CO_2 at the poles, and dark rays of impact craters are commonly depleted in CO_2 relative to surrounding terrain. The absence in the polar regions could be related to its origin or masking by polar frost deposits. Some terrain inferred to contain larger-grained ice also has higher CO_2 levels relative to surrounding terrain. The detected CO_2 seems to be contained in non-ice materials, but its presence in large-grained ice would be difficult to detect due to the strong absorption of water ice in this spectral region. Regions with mostly fine-grained ice (where CO_2 could be detected) do not seem to contain CO_2, suggesting that CO_2 distribution is not related to magnetospheric effects but is endogenic instead.

Other molecular species reported on Ganymede from early analysis of the *Galileo* NIMS IR spectra (though to a lesser extent than on Callisto) include SO_2, C≡N (perhaps as HCN), and CH (McCord *et al.* 1997, 1998a). The SO_2 has a complex spatial distribution but the band weakness prevents generating detailed maps. SO_2 has also been inferred from IUE data, which may imply abundance changes on decadal timescales (Domingue *et al.* 1998). The NIMS absorption features interpreted as due to C≡N (4.57 μm) and CH (3.4 μm) are consistent with those seen in spectra of tholins, the organic residues made in the laboratory by discharging energy into a gas mixture of C-, H-, O- and N-bearing molecules. These simple organic molecules could be the result of radiolysis on the surface or due to in-fall of asteroidal and cometary material onto Ganymede's surface. Interestingly, interstellar ice grains show very similar absorption spectra also interpreted as due to CO_2, CN, CH, in addition to H_2O (McCord *et al.* 1997, 1998a). Simple organic materials are apparently common in space, potentially synthesized from carbon-bearing ices by UV irradiation.

16.4 REGOLITH PROPERTIES

Ganymede's surface and regolith are affected by processes that include mass wasting, impact gardening, thermal processing, and charged particle interactions. The properties of Ganymede's regolith can be estimated using the tools of photometry, radiometry, and radar. Although not emphasized here, discussions of charged particle interactions with Ganymede's surface are found in chapters 19, 20, and 21.

16.4.1 Photometric Properties

Photometric investigations of Ganymede fall into two general categories: studies of whole-disk photometry that investigate average global behavior, and studies of disk-resolved observations that explore the photometric properties of different terrain units. An important advantage of whole-disk photometry is that observations from spacecraft and Earth-based telescopes can be combined to provide relatively uniform coverage of phase angles over the widest possible range so that a variety of photometric phenomena can be measured. Disk-resolved photometry from high resolution *Voyager* and *Galileo* images provides information about the scale-dependent spatial heterogeneity of materials deposited on Ganymede's surface and allows regolith photometric properties to be interpreted in a geological context.

Most work on Ganymede's photometry over the past decade has focused on application of the Hapke (1981, 1984, 1986, 1993, 2002) photometric model as a means of estimating the physical properties of the uppermost regolith. Hapke's bidirectional reflectance equation is expressed in terms of model parameters that relate to the physical structure and optical properties of the regolith and its constituents. These parameters are: ω_o, the average single-scattering albedo of regolith grains; $\bar{\theta}$, a mean slope angle of macroscopic surface relief; $B_{0,SH}$ and h_{SH}, parameters describing the amplitude and angular width of the shadow-hiding opposition effect; and additional model parameters that describe the directional scattering behavior, or particle phase function, of average regolith grains. Depending on the assumed mathematical form of the particle phase function, from one to three particle phase function parameters are typically used. In his most recent version, Hapke (2002) has introduced two additional parameters: $B_{0,CB}$ and h_{CB}, the amplitude and angular-width parameters of the coherent backscatter opposition effect.

Hapke's model parameters are valuable in having physical meaning. Single scattering albedo, ω_o, measures the scattering and absorption efficiency of average regolith grains and is related to the optical constants, mechanical structure, and grain size distribution of average regolith grains. A particle phase function $P(\alpha)$ is used to describe the directional scattering behavior with phase angle, α, for an average regolith grain. The directional scattering behavior is controlled by factors such as average particle transparency, grain size, and mechanical structure (McGuire and Hapke 1995). Because various workers have adopted different mathematical forms and parameterizations for $P(\alpha)$, it is most useful for us to express and compare their particle phase function results by calculating an effective asymmetry factor, g_{eff} (the weighted mean cosine of the scattering angle) from their model fits. Values of g_{eff} can vary from -1 to $+1$, such that $g_{eff} = 0$ for particles that scatter equally well in the forward and backward directions, $g_{eff} < 0$ for dominantly backward scattering (i.e., relatively opaque) grains, and $g_{eff} > 0$ for forward scattering (i.e., relatively transparent) grains. The macroscopic roughness parameter $\bar{\theta}$, provides a measure of surface texture at sub-millimeter and larger size scales (Helfenstein and Shepard 1999). Regolith covered planetary surfaces generally exhibit an opposition effect, a nonlinear surge in brightness that increases as the phase angle approaches zero.

Two physical mechanisms are considered to affect the opposition effect: shadow hiding (in which regolith grains progressively occult their own shadows with decreasing phase angle), and coherent backscatter (in which the tendency for separate light rays traversing conjugate paths through the regolith to constructively interfere increases with decreasing phase). The angular half-width of the shadow hiding opposition effect, h_{SH}, is controlled by the porosity of the regolith and the size distribution of regolith

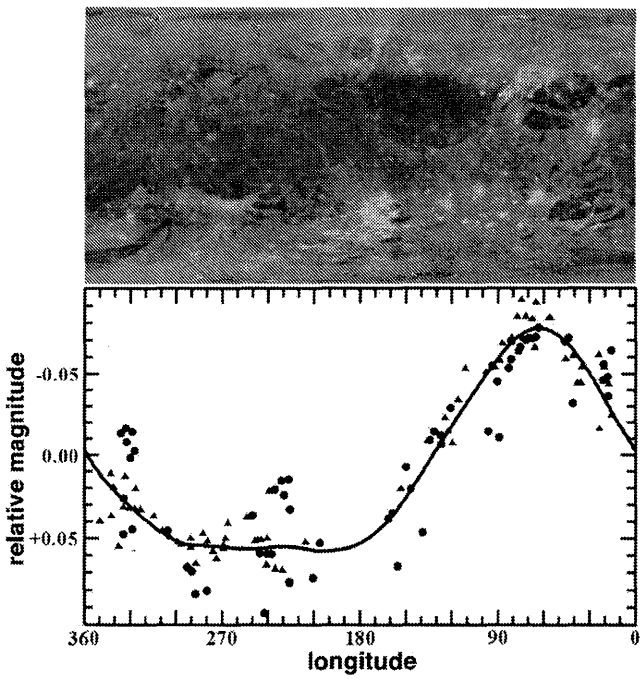

Figure 16.24. Global albedo map of Ganymede derived from *Voyager* and *Galileo* data, adjusted so that a synthetic lightcurve (solid curve) generated from the map is a best fit to the available telescopic data (circles from Morrison *et al.* (1974), and triangles from Millis and Thompson (1975)). Asymmetry is evident between the brightness of Ganymede's leading (centered 90° longitude) and trailing (centered 270° longitude) hemispheres (Helfenstein (2003).

grains. It generally decreases with increasing regolith porosity and narrowness of the particle size distribution. The shadow hiding amplitude, $B_{0,\mathrm{SH}}$, measures the transparency of grains, where $B_{0,\mathrm{SH}} = 1$ for a perfectly opaque particle and this parameter decreases with increasing grain transparency. Coherent backscatter generally contributes a very narrow peak (usually less than a couple of degrees) to the overall shape of the opposition effect (Helfenstein *et al.* 1997b, Shkuratov and Helfenstein 2001, Hapke 2002) and is superposed over the broader shadow hiding opposition effect. The angular half-width of the coherent backscatter opposition effect, h_{CB}, and its amplitude, $B_{0,\mathrm{CB}}$, are both controlled by the particle albedo, the size and spacing of particles, and especially the particle microstructure (Shkuratov and Helfenstein 2001; Helfenstein and Shkuratov 2003) relative to the wavelength of light used in its measure. The amplitude is expected to be largest for high-albedo scatterers with complex particle microstructure and narrowest for particles that allow long optical path lengths of scattering within the regolith.

Whole-Disk Photometry

Earth-based rotational lightcurves for the icy Galilean satellites, which are obtained at small phase angles, have long shown that each body exhibits a global brightness asymmetry that approximately correlates with the leading and trailing hemispheres (Figure 16.24). The hemispheric asymmetries are generally attributed to the areal distributions of different terrain albedo features and exogenic modification of the satellites' trailing hemispheres by particles trapped in Jupiter's magnetic field. Buratti (1991, 1995) and Domingue and Verbiscer (1997) sought to understand if leading-side/trailing-side asymmetries are manifested in the shapes of phase curves for each hemisphere and to identify what surface physical properties might be responsible. In each study, the parameters of the Hapke (1981, 1984, 1986) model were separately fit to leading-side and trailing-side phase curves compiled from telescopic observations and broadband *Voyager* imaging data (Table 16.1). Buratti's composite phase curves for Ganymede were derived from 20 selected *Voyager* clear filter (0.47 μm) images and comprehensive ground-based observations dating back to the work of Stebbins (1927). Domingue and Verbiscer (1997) used a more extensive collection of *Voyager* images and at two different wavelengths (0.47 μm and 0.55 μm), but relied only on the most recently published Earth-based coverage of Ganymede at small (<12°) phase angles.

The two independent studies yielded conflicting results. Buratti found little evidence that Ganymede's global photometric asymmetry was due to much more than albedo variations. In contrast, Domingue and Verbiscer (1997) concluded that Ganymede's hemispheric photometric asymmetry is due not only to variations in average particle albedos, but also to significant differences in surface macroscopic roughness, particle compaction state, and regolith grain transparency. The inconsistencies between results from the two studies above are closely tied to differences in the phase angle coverage and quality of the phase curve data that were reduced in each case. A close examination of Domingue and Verbiscer's data at small phase angles suggests that their discovery of a very narrow opposition effect on the leading hemisphere is a real phenomenon, but its apparent absence on the trailing hemisphere is more a consequence of poorer trailing-side phase coverage than it is a real difference in regolith structure (Helfenstein and Shkuratov 2003).

Only recently have photometric models been published that consider the simultaneous contributions of shadow hiding and coherent backscatter to the opposition effect (Helfenstein *et al.* 1997b, Shkuratov and Helfenstein 2001, Hapke 2002). Rather than looking for leading-side/trailing-side photometric asymmetries, Helfenstein and Shkuratov (2003) fit the Hapke (2002) model to global phase curves for Ganymede and other planetary objects by combining telescopic, *Voyager*, and *Galileo* whole-disk data. Table 16.2 compares their preliminary results for Ganymede to those for Europa and the Moon. The comparative results indicate that the average particles on Ganymede's surface are intermediate in albedo between lunar regolith and Europa's high-albedo grains. The macroscopic roughness $\bar{\theta}$ is lunar-like and agrees with earlier results of Buratti (1991 1995), and with Domingue and Verbiscer's leading side value. The effective asymmetry factor g_{eff} suggests the presence of particles that are slightly backscattering. It is important to note, however, that phase coverage of Ganymede and Europa at very large phase angles ($\alpha > 120°$) is sparse. Forward scattering in the particle phase functions of Ganymede and Europa regolith grains may occur and simply be undetectable because of limited whole-disk phase coverage.

Table 16.1. Modeled Hapke photometric parameters for Ganymede's leading and trailing hemispheres.

	Buratti (1991, 1995)		Domingue and Verbiscer (1997)			
	0.47 μm		0.47 μm		0.55 μm	
	leading	trailing	leading	trailing	leading	trailing
ω_o	0.82 ± 0.03	0.78 ± 0.03	0.83 ± 0.01	0.87 ± 0.01	0.95 ± 0.01	0.87 ± 0.01
$\bar{\theta}$	–	29° ± 2°	28° ± 3°	35° ± 3°	29° ± 3°	35° ± 3°
$B_{0,SH}$	–	–	0.62 ± 0.01	1.00 ± 0.01	0.86 ± 0.01	0.23 ± 0.01
h_{SH}	0.084	0.084	0.003 ± 0.001	0.074 ± 0.001	0.004 ± 0.001	0.074 ± 0.001
g_{eff}	−0.20 ± 0.04	−0.21 ± 0.04	0.26 ± 0.02	0.04 ± 0.01	+0.06 ± 0.02	−0.28 ± 0.02

Table 16.2. Hapke parameters fit to phase curves of Ganymede, Europa, and the Moon.

	Ganymede 0.47 μm	Europa 0.47 μm	Moon 0.56 μm
ω_o	0.76 ± 0.01	0.97	0.28
$\bar{\theta}$	28 ± 1°	23°	26°
$B_{0,SH}$	1.0	1.0	1.0
h_{SH}	0.36 ± 0.03	0.75	0.20
g_{eff}	−0.15 ± 0.01	−0.24	+0.16
$B_{0,CB}$	0.63 ± 0.05	0.83	0.46
h_{CB}	0.0038 ± 0.0004	0.0014	0.0396

Note: Data are from Helfenstein and Shkuratov (2003).

The shadow-hiding angular-width parameter h_{SH} is intermediate between the lunar value and Europa's. This could suggest that Ganymede's regolith is more compacted than the Moon's and less compacted than Europa's; however, that interpretation would be inconsistent with thermal inertial data (Section 16.4.2). It is more likely that the size distribution of particles that characterizes Ganymede's regolith is somewhat broader than the lunar regolith and narrower than Europa's. One possible geological interpretation would be that the presence of ice in the regoliths of Ganymede and Europa leads to progressively greater cementation and aggregation of soil particles than on the dry lunar surface. Helfenstein and Shkuratov's (2003) coherent backscatter results confirm the existence of a very narrow component of Ganymede's opposition effect seen in Domingue and Verbiscer's (1997) leading side data. Ganymede's coherent backscatter peak is broader than Europa's, consistent with the interpretation that Europa's regolith particles are higher in albedo and allow longer optical path lengths than Ganymede's. The Moon's coherent backscatter peak is much broader than Ganymede's, consistent with its comparatively low albedo and expected short optical path lengths. Finally, the amplitude of Ganymede's coherent-backscatter opposition effect is intermediate between the Moon's and Europa's, consistent with the intermediate albedo and average transparency of Ganymede's regolith particles.

Disk-Resolved Photometry

Early *Voyager*-based disk-resolved photometry of Ganymede was performed by Squyres and Veverka (1981), who used empirical photometric modeling to investigate the photometric behavior of individual geological features on Ganymede over phase angles $10° \leq \alpha \leq 124°$. They found that on average, bright terrain is about 20% higher in albedo than average examples of dark terrain but that the two terrains cannot be uniquely distinguished on the basis of albedo alone. Instead, the brightest examples of dark terrain are comparable in albedo to the darkest examples of bright terrain. Helfenstein (1986b), conducted a detailed investigation of 90 individual regions of Ganymede's surface covering from $5° \leq \alpha \leq 126°$ and using a precursor of Hapke's (1986) photometric model. On the basis of similarities in albedo and phase behavior, he grouped his observations into six photometric classes of dark terrain and eight classes of bright terrain. The single-scattering albedos for dark terrain classes varied from $0.42 \leq \omega_o \leq 0.72$, and bright terrain classes varied from $0.58 \leq \omega_o \leq 0.90$. In both cases, the largest values of ω_o were found within Ganymede's polar caps. For both dark and bright terrains, the derived values of macroscopic roughness varied from less than 1° to about 20° (although for individual regions, values as large as $\bar{\theta} = 39°$ were found). The particle phase functions of most regolith materials were found to be dominantly backward scattering, except for polar examples of bright and dark terrains that exhibited significant forward scattering. Though it is unclear that the opposition effect and average particle phase function were reliably decoupled in his solutions for these parameters, Helfenstein was able to show that, when these two effects are combined, bright terrain on average has a more pronounced opposition effect than dark terrain (Figure 5.2 of Helfenstein 1986b).

A decade later, Hillier *et al.* (1996) used a globally complete disk-resolved *Voyager* data set to find Hapke parameters for different Ganymede terrains. Their results of $B_{0,SH} = 0.53$ for bright terrain and $B_{0,SH} = 0.21$ for dark terrain confirm that bright terrain has a significantly more intense opposition effect. Hillier *et al.* found that the macroscopic roughness of average dark terrain and average bright terrain are statistically the same. Their derived values of $\bar{\theta} = 29°$ for dark terrain and $\bar{\theta} = 28°$ for bright terrain are in good agreement with the whole- disk results of Buratti (1991, 1995) and Ganymede leading side results of Domingue and Verbiscer (1997). Hillier *et al.* find $\omega_o = 0.72 \pm 0.02$ and $g_{eff} = -0.24 \pm 0.02$ for dark terrain, compared to $\omega_o = 0.80 \pm 0.02$ and $g_{eff} = -0.19 \pm 0.02$ for bright terrain, consistent with the average dark terrain regolith being slightly lower in albedo and more opaque than bright terrain regolith materials.

An inherent flaw with inferring the physical characteristics of Ganymede's regolith materials from Hapke analysis is that terrains are assumed to be photometrically

and compositionally homogeneous over size scales from submillimeter to tens or hundreds of kilometers. However, one of *Galileo*'s most important findings is that surface materials on Ganymede (as well as Europa and Callisto) are highly segregated at size scales of a few kilometers or less. The extreme contrast variations observed in images (~3:1) cannot be achieved solely by topographic shading, and must result largely from differences in albedo (Pappalardo *et al.* 1998a, Oberst *et al.* 1999). This dichotomy of materials on Ganymede's surface exists at a size scale that is generally below the spatial resolution of the *Voyager*-based studies described above. Consequently, the physical interpretations that have been offered are necessarily crude approximations.

The photometric characteristics of the segregated darkest and brightest materials visible at *Galileo* highest resolution have not yet been investigated in great detail. The albedo properties of dark deposits are best understood because they accumulate on topographically flat areas and relatively pure exposures can even be found at scales above the spatial resolution limits of the best *Voyager* images. In particular, unusually dark deposits cover the floors of numerous fresh-appearing craters with diameters of about 10 km or less. Crater dark floor deposits were investigated from *Voyager* images by Helfenstein (1986a, 1986b) and Schenk and McKinnon (1991). More recently, Helfenstein *et al.* (1997a) used high resolution *Galileo* images (e.g., Figures 16.8 and 16.11) to investigate the albedos of dark floor deposits. The results of these studies are all in excellent mutual agreement when accounting for differences in spectral bandpasses and phase angles of *Voyager* and *Galileo* images. The darkest materials visible on Ganymede's surface have estimated normal albedos (i.e., albedos extrapolated to incidence and emission angles normal to the surface) ranging from 0.12 to 0.34 with a mean of 0.25 ± 0.04 (Helfenstein *et al.* 1997a). This is comparable to average values for dark materials on Callisto's surface and dark deposits found in valley floors and dark spots on Europa (Helfenstein *et al.* 1998). However, even the dark deposits visible on Ganymede are about five times higher in albedo than D-type asteroid materials, which have been proposed as possible analogs for the dark contaminant in Ganymede soils.

The photometric properties of high albedo materials exposed along the walls of ridges, troughs, and crater walls are more poorly understood than Ganymede's dark materials. They are difficult to study because relatively pure-appearing exposures of the high albedo materials are reliably identified only in the highest resolution *Galileo* images, and because they generally occur on surfaces for which accurate local photometric angles are difficult to measure. Large exposures of relatively unsegregated ice may occur in the floors of large, fresh-appearing rayed craters on Ganymede, and estimated normal reflectances of the brightest such materials from global albedo mapping exceed unity ($r_n \sim 1.14$), comparable to bright icy materials on Europa (Helfenstein *et al.* 1998). Note that normal albedos greater than unity (but less than 2) are permitted due to the contribution of coherent backscatter to the opposition effect.

Due to the segregation of dark and bright materials at kilometer and smaller scales, the large-scale variations in photometric properties of Ganymede terrains observed in *Voyager* and typical *Galileo* images may best be explained by differences in the exposed areal fraction of dark deposits relative to bright ice within a resolution element. Figure 16.24 shows a composite *Voyager–Galileo* 0.56-μm global albedo map that has been normalized at $\alpha = 6°$ such that a synthetic rotational lightcurve generated from the map is a best match to Earth-based telescopic lightcurve data (Helfenstein 2003). At the *Voyager*-like resolution of this map (16 km/pixel), estimated normal reflectances range from 0.18 to 1.14 (with a mean of 0.53) after accounting for Ganymede's average opposition effect. Assuming that the value of 1.14 is representative of unsegregated clean ice, and adopting 0.12 as the normal reflectance of the darkest detectable low albedo material, then the distribution of normal albedos across the albedo map correspond to an areal abundance of exposed dark deposits ranging from 0 to 94%, with a mean of about 60%.

16.4.2 Thermal Characteristics

Ganymede's surface temperatures have been studied from the ground, from the *Voyager* Infrared Interferometer Spectrometer (IRIS) instrument, and from the *Galileo* Photopolarimeter-Radiometer. Daytime temperatures are found to peak near 150 K (Spencer 1987a, Orton *et al.* 1996), dropping to 90 to 95 K at night. The diurnal temperature range can be fitted with a thermal inertia near 7×10^4 erg cm^{-2} K^{-1} s$^{-1/2}$ (70 J m^{-2} K^{-1} s$^{-1/2}$), very similar to the values for Callisto and Europa (Spencer 1987a, Spencer *et al.* 1999). Eclipse cooling curves show that like the other Galilean satellites, Ganymede's surface is not homogeneous, and includes a lower thermal inertia component responsible for rapid initial cooling, and a higher thermal inertia component producing slower cooling during the remainder of the eclipse (Morrison and Cruikshank 1973). Morrison and Cruikshank modeled the eclipse cooling with a two-layer model in which the low thermal inertia component overlaid the higher thermal inertia component, though solutions in which the two components are separated horizontally are also possible (Spencer 1987a). In either case, there must be some extremely uncompacted material on the surface, with a thermal inertia near 1.5×10^4 erg cm^{-2} K^{-1} s$^{-1/2}$ (15 J m^{-2} K^{-1} s$^{-1/2}$).

Surface temperature is found to depend on terrain type. The bright grooved terrain is about 5 K colder during the day than the dark terrain, and bright craters are about another 20 K colder than that (Spencer 1987a, Orton *et al.* 1996). However, at night the dark/bright terrain contrast reverses, with the bright grooved terrain being about 3 K warmer than the dark terrain, though bright craters are colder than either bright or dark terrain (Figure 16.25). This contrast reversal is consistent with the idea that the surface consists of two spatially segregated units, as originally suggested to explain the eclipse cooling curve (Spencer 1987a): a dark, low thermal inertia unit, perhaps dust, and a bright, high thermal inertia unit, perhaps ice. The larger abundance of the ice component in the bright terrain would then explain its higher effective thermal inertia and warmer nighttime temperatures. However, Ganymede's bright ray craters are colder than other surface units during both day and night, and thus do not follow the nighttime temperature contrast reversal exhibited by the grooved and dark terrain. This suggests that the ice in the fresh bright craters has low thermal inertia, and is different in texture from the

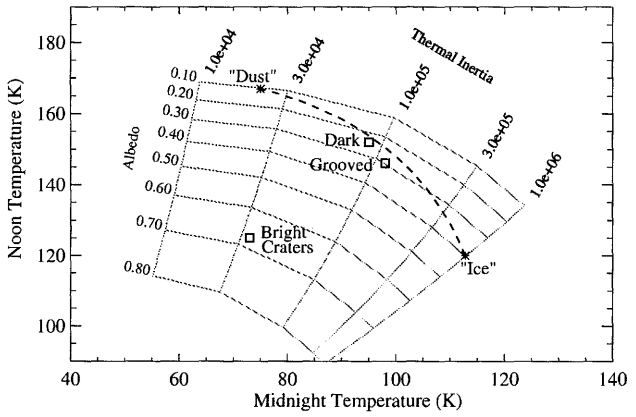

Figure 16.25. Typical Ganymede noon *vs.* midnight temperature variations (open squares), observed by *Galileo* PPR for three terrain types, compared to a grid of homogeneous thermal model temperatures with a range of albedos A and thermal inertias Γ (in units of erg cm^{-2} s$^{-1/2}$ K^{-1}). The "Dust" and "Ice" points give the diurnal temperatures for the end-member components (A = 0.1, Γ = 1.6 × 10^4 and A = 0.5, Γ= 1.0 × 10^6, respectively) of a two-component model (with equal area for each component) fitted to Ganymede's diurnal and eclipse temperature variations (Spencer 1987b). The dashed line gives temperatures for an areal mix of the two components with varying relative proportions. The dark terrain and grooved terrain temperatures fall close to this mixing line, supporting the two-component model and indicating that each terrain type has a slightly different fraction of the two surface components. However, the bright craters fall nowhere near the trend, indicating that the ice in these bright ray craters has much lower thermal inertia than the "ice" component of the two-component model that fits the rest of Ganymede's surface.

high thermal inertia ice seen elsewhere on the surface. This might be explained if ice within bright grooved terrain has undergone sintering by sublimation processes, increasing its thermal inertia relative to ice in cold and youthful fresh craters (which is somewhat finer grained, Section 16.3.2).

Ganymede's 10- to 50-μm thermal emission spectrum measured by *Voyager* IRIS, like that of Callisto and Europa, is completely featureless, offering no clues to surface composition (see Appendix 1). Like Callisto, brightness temperature varies smoothly with wavelength, probably due to temperature contrasts within each IRIS field of view, but the pattern of variation is dramatically different from that on Callisto (Spencer 1987a, Chapter 17).

Thermal emission from the Galilean satellites has also been measured at submillimeter and longer wavelengths, where daytime brightness temperatures are lower due partly due to emission coming from below the surface (see Muhleman and Berge (1991) and references within). Ganymede, like Europa, has a brightness temperature at centimeter wavelengths that is lower than the expected subsurface temperatures, probably due to the fundamentally low emissivity of cold ice at these wavelengths (Warren 1984) plus that resulting from near-surface scattering, but Ganymede is unusual in also having a low emissivity at millimeter wavelengths.

Ganymede's daytime thermal radiation is probably dominated by the dark non-ice component of the surface, because of its higher temperature. It is thus difficult to use thermal radiation to directly determine the temperature and thermal characteristics of the bright icy component. However, the daytime temperature of the icy component on the leading side has been estimated as 126 ± 12 K by means of near-IR reflectance spectroscopy, using the temperature dependence of the water-ice spectrum (Grundy *et al.* 1999).

16.4.3 Radar Characteristics

Like all the Galilean satellites, Ganymede's radar signature is unusual. Its radar geometric albedo at 13 and 3.5 cm is about 0.37 (Ostro *et al.* 1992), compared to 0.025 for a typical terrestrial planet. Moreover its circular polarization ratio, the ratio of echo power received with the transmitted sense of circular polarization compared to that received with the opposite polarization, is 1.2 compared to 0.1 for the terrestrial planets. All three icy Galilean satellites scatter radar energy like very rough surfaces, unlike the Moon's near-specular scattering properties. Crude radar images are possible using delay-Doppler techniques (Ostro *et al.* 1992) or imaging of the radar return using the Very Large Array (Harcke *et al.* 2001), but detailed correlation with geological features is not yet possible. At 70 cm, the radar albedo is lower than at shorter wavelengths, though still unusually high (Black *et al.* 2001b).

It seems likely that these unusual properties result from the near-surface material being only weakly absorbing, allowing for multiple scattering in the subsurface, whereas single-scattering from the surface dominates the radar reflectivity of the Moon and other terrestrial planets (Ostro and Shoemaker 1990). Coherent backscattering can then explain the circular polarization ratios (Hapke 1990, Peters 1992). Black *et al.* (2001a) applied the Peters model to the available radar data, and were able to reproduce Ganymede's scattering behavior with a model surface consisting of icy scatterers ranging up to at least 2 m in size, distributed in a porous ice matrix at least a few meters thick. The high radar albedos rule out silicates as the scatterers.

16.5 INTERIOR EVOLUTION AND GLOBAL HISTORY

16.5.1 Interior Structure and Evolution

Prior to the *Galileo* encounters, debate as to the possible internal structures of Ganymede centered on whether the satellite is undifferentiated with a roughly uniform mixture of rock and ice (including high-pressure ice phases), or differentiated into ice phases above a silicate core (e.g., Schubert *et al.* 1986), with the latter being favored. The spectacular results from *Galileo* gravity and magnetometry are reviewed in Chapters 13 and 21, respectively, so here we mention only the highlights of the new paradigms, along with possible connections to surface geology.

Galileo gravity data implies that Ganymede is highly differentiated, with an iron core and silicate mantle capped by an ice shell ~800 km thick (Anderson *et al.* 1996,). The existence of a current-day intrinsic magnetic field (Kivelson *et al.* 1996, 1998) suggests that Ganymede's iron core is hot enough (>1300 K (Anderson *et al.* 1996)) to be at least partially molten today. Moreover, *Galileo* magnetometer data suggest an induced magnetic field component, implying that

Ganymede has a liquid ocean tens of kilometers thick, at a nominal depth of about 170 km. A thermal gradient steep enough to induce melting implies an internal structure for Ganymede consisting of ice phases I, III, V, and VI with increasing depth, with the ocean located at the minimum melting temperature (~250 K) that occurs on the phase boundary between ice I and ice III, expected near 170-km depth (Kivelson *et al.* 2002). Sulphate and alkali halides salts would allow the ocean to be cooler.

The geologically active past of Ganymede offers a stark contrast from that of its relatively quiescent neighbor Callisto (Chapter 17), though the two satellites are of similar size and density. Moreover, the strongly differentiated structure of Ganymede differs dramatically from Callisto's weakly differentiated interior (Chapter 13). Ganymede is slightly larger and denser than Callisto, and its slight advantage in radiogenic and accretional heat has been invoked to explain the differences in their geologies (e.g., Schubert *et al.* 1986). However, given their extreme internal dichotomy as identified by *Galileo*, it seems that a more likely explanation involves past tidal heating of Ganymede related to the Laplace resonance with Europa and Io, a dance which Callisto sits out. Malhotra (1991) and Showman and Malhotra (1997) have considered the chaotic orbital evolution that would result if Ganymede were captured into the Laplace resonance, including the effects of other temporary resonances with Europa and Io that may have preceded the stable Laplace resonance. Increases in Ganymede's orbital eccentricity during resonance capture may have triggered enhanced tidal heating, internal melting, and geological activity, depending on the preexisting state of the satellite (specifically, the temperature structure of its internal ice, which in turn controls the degree of tidal dissipation) (Showman *et al.* 1997). However, radiogenic and especially accretional heat are themselves expected to differentiate Ganymede into a rocky core and ice mantle (Schubert *et al.* 1986), so the relevance of tidal heating to induce differentiation from an essentially undifferentiated (Callisto-like) state is less clear. One possibility is that Ganymede and Callisto accreted undifferentiated (see the satellite formation model of Canup and Ward (2002) discussed in Section 13.8 and in Chapter 2). Ganymede's existing intrinsic magnetic field (and implied hot iron core) may constrain the time of grooved terrain formation to $\leq$1 Gyr (the expected timescale of core cooling), if core heating and grooved terrain formation are both remnants of the same past tidal heating event (Showman *et al.* 1997, Zahnle *et al.* 2003, Chapter 13).

16.5.2 Global Stresses

Because Ganymede has experienced differentiation and orbital resonance while Callisto largely has not, it is tempting to relate these aspects of its history to the formation of Ganymede's grooved terrain. Changes in Ganymede's interior structure and orbital parameters would have changed the shape of the satellite, which in turn would induce stress on the lithosphere. Changes in internal heating and structure may also have affected convective patterns within the satellite.

The effect of internal differentiation on Ganymede's shape is possibly threefold: volume expansion, decrease of tidal and rotational distortion, and increased spin rate. Volume expansion may be driven by internal heating and melting (Zuber and Parmentier 1984, Showman *et al.* 1997) and/or differentiation of rock from ice, because rock is less compressible than ice (Squyres 1980b, Mueller and McKinnon 1988). Choosing values for interior density and mass distribution consistent with initial *Galileo* flybys of Ganymede (Anderson *et al.* 1996) for the models of Squyres (1980b) and Mueller and McKinnon (1988), the maximum volume expansion due to differentiation of Ganymede could be ~9%. Volume expansion itself induces global isotropic tensile stress, but if volume expansion is caused by differentiation, the isotropy will be broken by changes in the satellite figure. Concentration of mass in the interior will decrease the self-gravitation of the tidal and equatorial bulges, and thus the tidal and rotational distortions will decrease (Dermott 1979). For the full differentiation of Ganymede from a Callisto-like state to its current state, these distortions will decrease by 28% (Collins 2000). Mass concentration in the interior of Ganymede may also increase the rotation rate by almost 30% in order to conserve angular momentum, if the differentiation rate is faster than that of tidal locking (Collins *et al.* 1999). Friedson and Stevenson (1983) estimate that 90% of Ganymede's differentiation could have taken place in 10^3 years, similar to the tidal locking timescale if Ganymede were perfectly dissipative (Peale 1977), which might be achievable if its ice were molten (Showman *et al.* 1997). In this case, Ganymede's rotation rate may be unaffected by differentiation.

Another possibility for Ganymede is nonsynchronous rotation, which if it occurred, would induce stresses analogous to those modeled for Europa (Helfenstein and Parmentier 1985). Indirect evidence for past nonsynchronous rotation of Ganymede is accumulating. The crater distribution in bright terrains increases toward the apex of orbital motion by a factor of ~4 relative to the antapex, while models of cometary impactor fluxes predict a 70-fold difference (Zahnle *et al.* 2001). The preferred explanation for the observed weak apex/antapex asymmetry is that Ganymede rotated nonsychronously for an extended period after bright terrain formation, diluting the predicted asymmetry. This period of rotation might have been triggered by increases in orbital eccentricity and internal heating during entrance into the Laplace resonance (Malhotra 1991, Showman and Malhotra 1997, Showman *et al.* 1997). Corroborating evidence may lie in the distribution of linear crater chains (catenae), which are probably formed by tidally disrupted comets (Melosh and Schenk 1993), and should form only on the hemisphere facing the vector of outgoing comets. This is true on Callisto (Schenk *et al.* 1996), but analysis of *Galileo* imaging reveals that several of the 11 or so catenae on Ganymede occur on the opposite hemisphere of Ganymede, consistent with nonsynchronous rotation of the satellite's outer ice shell (Zahnle *et al.* 2001, Chapter 18).

Though changes in figure due to differentiation and orbital evolution may have induced global stress on the surface of Ganymede, this does not necessarily account for formation of grooved terrain. Early differentiation would be inconsistent with a young age of grooved terrain, while the heat released by differentiation may have erased any surface record of that and earlier periods (McKinnon and Parmentier 1986). Capture into the Laplace resonance could have provided a delayed heat pulse trigger for melting of internal

ices and associated global expansion, but Ganymede may have been already differentiated at that time (Showman *et al.* 1997). It has been suggested that grooved terrain may be related to diapiric activity triggered by a heat pulse upon cooling and closing of an internal ocean (Kirk and Stevenson 1987), but the existence of a modern-day ocean seems to make this argument moot (unless it is thin). It has also been proposed that grooved terrain formation may be related to internal convection (Shoemaker *et al.* 1982), but it is not clear that convective stresses are sufficient to fracture the lithosphere (McKinnon 1998), or that internal ice convection has indeed occurred (cf. Ruiz 2001). The implications for convection of Ganymede's interior structure and heat sources have not yet been explored in detail.

16.6 CONCLUDING REMARKS

The diversity and complexity of Ganymede's surface and inferred geological processes makes it one of the most compelling solar system bodies. Its dark terrain tells of ancient solar system processes; its bright grooved terrain probably formed through processes analogous to terrestrial rifting; an intermediate level of geological activity between its neighbors Callisto and Europa makes it a Rosetta Stone for understanding the icy Galilean satellites; its intricate internal layering and internal magnetic field make it a moon worthy of planetary stature.

The existence of an internal ocean within Ganymede begs the question of the satellite's potential to harbor life. Ganymede's ocean (like Callisto's) is sandwiched between layers of less and more dense ice phases. Therefore, unlike Europa's ocean, Ganymede's is cut off from any direct supply of nutrients and chemical energy from hydrothermal systems that might support life. Indirect supply of nutrients to the ocean might be possible if water-rich diapirs are able to rise buoyantly from the deep ice/rock interface through the intervening high-density ice phases (Barr *et al.* 2001), or perhaps by other means. Ganymede's ocean is also about an order of magnitude deeper than Europa's, so transport of radiolytic products from the surface to the ocean (cf. Chyba and Phillips 2001, Chapter 15) would be much less efficient on Ganymede than on Europa in the present epoch, though Ganymede's ocean may have been significantly shallower during a past epoch of intense heating. Overall, a questionable supply of nutrients and biogenic elements makes the potential for life in Ganymede's ocean seem small (Task Group on Sample Return from Small Solar System Bodies 1998), but the possibility is not ruled out. Tests of whether life could have arisen within Ganymede await direct sampling of its surface and subsurface in the distant future.

Galileo observations have greatly advanced understanding of Ganymede's geology, but many important questions remain, including:

- How does the epoch of dark terrain formation compare to Callisto's early geological history?
- Did entrance into the Laplace resonance affect internal evolution, and how is grooved terrain formation linked to internal processes (differentiation, phase changes, and/or convection)?
- What are the relative roles of geological processes (tectonism, volcanism, mass wasting) that have shaped grooved terrain?
- What is the age of grooved terrain, and how extended was its formation period?
- Is any part of the surface still geologically active today?
- What is the chemistry and biological potential of Ganymede's ocean?

Future exploration of Ganymede may include close flybys, an orbiting spacecraft, or surface landers to understand Ganymede's integrated surface (this chapter), interior (Chapter 13), magnetosphere (Chapter 21), and atmosphere (Chapter 19). Among possible goals for future exploration (Pappalardo *et al.* 2001) are: (1) characterize the global distribution, regional relationships, and detailed topography of geological features; (2) determine the composition, distribution, and state of ice and non-ice surface components, notably organic materials and irradiation products; (3) measure and monitor the magnetic field and plasma energy spectrum over time from a variety of altitudes; (4) measure the gravity field to high accuracy to constrain internal structure; (5) characterize the neutral atmosphere and ionosphere, including the composition, source, and escape mechanisms; and (6) determine the characteristics, causes, and spatial/temporal variability of auroral emissions. An orbiter would permit long-term, dedicated study of Ganymede as an integrated system to unlock secrets of this extraordinary world – one which holds key clues to the evolution of the Galilean satellite system and outer planet satellites in general.

Acknowledgements. We gratefully acknowledge Baerbel Lucchitta and Adam Showman for helpful reviews. This work was supported in part by grants to RTP and JWH from the NASA Planetary Geology and Geophysics program.

REFERENCES

Allison, M. L. and S. M. Clifford, Ice-covered water volcanism on Ganymede, *J. Geophys. Res.* **92**, 7865–7876, 1987.

Anderson, J. D., E. L. Lau, W. L. Sjogren, G. Schubert, and W. B. Moore, Gravitational constraints on the internal structure of Ganymede, *Nature* **384**, 541–543, 1996.

Asphaug, E., J. M. Moore, D. Morrison, P. H. Figueredo, R. Greeley, R. T. Pappalardo, L. M. Prockter, R. Tufts, and *Galileo* SSI Team, Crater-controlled fracture networks and the depth of ice lithospheres, in *Lunar and Planetary Science Conference Abstracts*, p. 1587, 1998.

Barr, A. C., R. T. Pappalardo, and D. J. Stevenson, Rise of deep melt into Ganymede's ocean and implications for astrobiology, in *Lunar and Planetary Science Conference Abstracts*, p. 1781, 2001.

Black, G. J., D. B. Campbell, and P. D. Nicholson, Icy Galilean satellites: Modeling radar reflectivities as a coherent backscatter effect, *Icarus* **151**, 167–180, 2001a.

Black, G. J., D. B. Campbell, and S. J. Ostro, Icy Galilean satellites: 70 cm radar results from Arecibo, *Icarus* **151**, 160–166, 2001b.

Buratti, B. J., Ganymede and Callisto: Surface textural dichotomies and photometric analysis, *Icarus* **92**, 312–323, 1991.

Buratti, B. J., Photometry and surface structure of the icy Galilean satellites, *J. Geophys. Res.* **100**, 19 061–19 066, 1995.

Calvin, W. M., R. N. Clark, R. H. Brown, and J. R. Spencer, Spectra of the icy Galilean satellites from 0.2 to 5 micron: A compilation, new observations, and a recent summary, *J. Geophys. Res.* **100**, 19 041–19 048, 1995.

Calvin, W. M., R. E. Johnson, and J. R. Spencer, O_2 on Ganymede: Spectral characteristics and plasma formation mechanisms, *Geophys. Res. Lett.* **23**, 673, 1996.

Canup, R. M. and W. R. Ward, Formation of the Galilean satellites: Conditions of accretion, *AJ* **124**, 3404–3423, 2002.

Cassachia, R. and R. G. Strom, Geologic evolution of Galileo Regio, Ganymede, lunar planet, *J. Geophys. Res.* **89**, B419–B428, 1984.

Chyba, C. F. and C. B. Phillips, Possible ecosystems and the search for life on Europa, *Proc. Natl. Acad. Sci.* **98**, 801–804, 2001.

Clark, R. N., F. P. Fanale, and M. J. Gaffey, Surface composition of natural satellites, in *Satellites*, J. A. Burns, M. S. Matthews (eds), University of Arizona Press, pp. 437–491, 1986.

Collins, G., *Driving Mechanisms for Grooved Terrain Tectonics on Ganymede and Chaotic Terrain Formation on Europa: Constraints from Galileo Data*, Ph.D. thesis, Brown University, 2000.

Collins, G. C., The youngest grooves on Ganymede, in *Lunar and Planetary Science Conference Abstracts*, p. 1783, 2002.

Collins, G. C., J. W. Head, and R. T. Pappalardo, Formation of Ganymede grooved terrain by sequential extensional episodes: Implications of *Galileo* observations for regional stratigraphy, *Icarus* **135**, 345–359, 1998a.

Collins, G. C., J. W. Head, and R. T. Pappalardo, The role of extensional instability in creating Ganymede grooved terrain: Insights from *Galileo* high-resolution stereo imaging, *Geophys. Res. Lett.* **25**, 233, 1998b.

Collins, G. C., J. W. Head, R. T. Pappalardo, and *Galileo* SSI Team, Analysis of regional stratigraphic relationships in Ganymede grooved terrain: Galileo results, in *Lunar and Planetary Science Conference Abstracts*, p. 1319, 1998c.

Collins, G. C., J. W. Head, R. T. Pappalardo, and *Galileo* SSI Team, Geology of the *Galileo* G7 Nun Sulci target area, Ganymede, in *Lunar and Planetary Science Conference Abstracts*, p. 1755, 1998d.

Collins, G. C., R. T. Pappalardo, and J. W. Head, Surface stresses resulting from internal differentiation: Application to Ganymede tectonics, in *Lunar and Planetary Science Conference Abstracts*, p. 1695, 1999.

Collins, G. C., J. W. Head, R. T. Pappalardo, and *Galileo* SSI Team, A global database of grooves and dark terrain on Ganymede, enabling quantitative assessment of terrain features, in *Lunar and Planetary Science Conference Abstracts*, p. 1034, 2000.

Collins, G. C., J. W. Head, R. T. Pappalardo, B. Nixon, B. Giese, and R. Wagner, The formation of Arbela Sulcus and other smooth linear features on Ganymede: Possible crustal spreading and shear, in *Lunar and Planetary Science Conference Abstracts*, p. 1498, 2001.

Conca, J., Dark-ray craters on Ganymede, in *Lunar and Planetary Science Conference Abstracts*, pp. 172–174, 1981.

Cooper, J. F., R. E. Johnson, B. H. Mauk, H. B. Garrett, and N. Gehrels, Energetic ion and electron irradiation of the icy Galilean satellites, *Icarus* **149**, 133–159, 2001.

Croft, S., R. Cassachia, and R. Strom, Geologic map of the Tiamat Sulcus quadrangle of Ganymede, *U. S. Geol. Surv. Map.* **I-1548**, Jg–9, 1990.

Croft, S. K. and B. N. Goudreau, Tectonism and volcanism in Ganymede's dark terrain, in *Lunar and Planetary Science Conference Abstracts*, p. 209, 1987.

Croft, S. K. and R. G. Strom, Ganymede's crust: Structural indicators in the Tiamat Sulcis quadrangle, in *Lunar and Planetary Science Conference Abstracts*, pp. 156–157, 1985.

DeRemer, L. C. and R. T. Pappalardo, Manifestations of strike-slip faulting on Ganymede, in *Lunar and Planetary Science Conference Abstracts*, p. 2033, 2003.

Dermott, S. F., Shapes and gravitational moments of satellites and asteroids, *Icarus* **37**, 575–586, 1979.

Dombard, A. J., *Modeling of Geodynamics Processes on Ganymede and Callisto: Insight into Thermal and Tectonic Histories*, Ph.D. thesis, Washington University, St. Louis, 2000.

Dombard, A. J. and W. B. McKinnon, Long-term retention of impact crater topography on Ganymede, *Geophys. Res. Lett.* **27**, 3663, 2000.

Dombard, A. J. and W. B. McKinnon, Formation of grooved terrain on Ganymede: Extensional instability mediated by cold, superplastic creep, *Icarus* **154**, 321–336, 2001.

Domingue, D. and A. Verbiscer, Re-analysis of the solar phase curves of the icy Galilean satellites, *Icarus* **128**, 49–74, 1997.

Domingue, D. L., A. L. Lane, and R. A. Beyer, IUE's detection of tenuous SO_2 frost on Ganymede and its rapid time variability, *Geophys. Res. Lett.* **25**, 3117, 1998.

Durham, W. B., S. H. Kirby, and L. A. Stern, Creep of water ices at planetary conditions: A compilation, *J. Geophys. Res.* **102**, 16 293–16 302, 1997.

Fagents, S. A., R. Greeley, R. J. Sullivan, R. T. Pappalardo, L. M. Prockter, and the *Galileo* SSI Team, Cryomagmatic mechanisms for the formation of Rhadamanthys Linea, triple band margins, and other low-albedo features on Europa, *Icarus* **144**, 54–88, 2000.

Fanale, F. P., T. V. Johnson, and D. L. Matson, Io's surface and the histories of the Galilean satellites, in *Planetary Satellites*, J. A. Burns (ed), University of Arizona Press, pp. 379–405, 1977.

Fanale, F. P., Y. H. Li, E. Decarlo, N. Domergue-Schmidt, S. K. Sharma, K. Horton, J. C. Granahan, and *Galileo* NIMS Team, Laboratory simulations of the chemical evolution of Europa's aqueous phase, in *Lunar and Planetary Science Conference Abstracts*, p. 1248, 1998.

Figueredo, P. H., R. Greeley, J. M. Moore, E. Asphaug, and *Galileo* SSI Team, Crater-influenced fracture pattern of Nicholson Regio: Implications for the cratering record of Ganymede, in *Lunar and Planetary Science Conference Abstracts*, p. 1330, 1998.

Figueredo, P. H., R. Greeley, and *Galileo* SSI Team, Fracture patterns on Ganymede and the initiation of tectonic resurfacing, in *Lunar and Planetary Science Conference Abstracts*, p. 1832, 1999.

Fletcher, R. C. and B. Hallet, Unstable extension of the lithosphere: A mechanical model for basin-and-range structure, *J. Geophys. Res.* **88**, 7457–7466, 1983.

Frank, L. A., W. R. Paterson, K. L. Ackerson, and S. J. Bolton, Outflow of hydrogen ions from Ganymede, *Geophys. Res. Lett.* **24**, 2151, 1997.

Friedson, A. J. and D. J. Stevenson, Viscosity of rock-ice mixtures and applications to the evolution of icy satellites, *Icarus* **56**, 1–14, 1983.

Gehrels, T., Pictures of Ganymede, in *Jupiter*, T. Gehrels (ed), University of Arizona Press, pp. 406–411, 1976.

Giese, B., J. Oberst, T. Roatsch, G. Neukum, J. W. Head, and R. T. Pappalardo, The local topography of Uruk Sulcus and Galileo Regio obtained from stereo images, *Icarus* **135**, 303–316, 1998.

Giese, B., R. Wagner, G. Neukum, R. Pappalardo, J. W. Head, and the *Galileo* SSI Team, the topography of bright/dark terrain on Ganymede, in *Lunar and Planetary Science Conference Abstracts*, p. 1751, 2001.

Goldreich, P. and S. Soter, Q in the solar system, *Icarus* **5**, 375–389, 1966.

Goldsby, D. L. and D. L. Kohlstedt, Superplastic deformation of ice: Experimental observations, *J. Geophys. Res.* **106**, 11 017–11 030, 2001.

Golombek, M. P., Constraints on the expansion of Ganymede and the thickness of the lithosphere, *J. Geophys. Res.* **87**, 77, 1982.

Golombek, M. P. and M. L. Allison, Sequential development of grooved terrain and polygons on Ganymede, *Geophys. Res. Lett.* **8**, 1139–1142, 1981.

Golombek, M. P. and W. B. Banerdt, Early thermal profiles and lithospheric strength of Ganymede from extensional tectonic features, *Icarus* **68**, 252–265, 1986.

Grimm, R. E. and S. W. Squyres, Spectral analysis of groove spacing on Ganymede, *J. Geophys. Res.* **90**, 2013–2021, 1985.

Grundy, W. M., M. W. Buie, J. A. Stansberry, J. R. Spencer, and B. Schmitt, Near-infrared spectra of icy outer solar system surfaces: Remote determination of H_2O ice temperatures, *Icarus* **142**, 536–549, 1999.

Guest, J. E., B. Remo, and R. Greeley, Geologic map of the Uruk Sulcus quadrangle, Ganymede, *U. S. Geological Survey Miscellaneous Investigations Series* **Map I-2289**, 1988.

Hamblin, W. K., Origin of "reverse drag" on the downthrown side of normal faults, *Geol. Soc. America Bull.* **76**, 1145–1164, 1965.

Hansen, G. B., A method of measuring surface ice abundance: Application to Ganymede, in *Lunar and Planetary Science Conference Abstracts*, p. 1060, 2002.

Hansen, G. B. and T. B. McCord, Amorphous and crystalline ice on the Galilean satellites: A balance between thermal and radiolytic processes, in *Lunar and Planetary Science Conference Abstracts*, p. 1630, 2000.

Hansen, G. B. and T. B. McCord, Amorphous and crystalline ice on the Galilean satellites: A balance between thermal and radiolytic processes, *J. Geophys. Res.* **submitted**, 2003.

Hansen, G. B., T. B. McCord, W. D. Smythe, and R. Carlson, The state of water ice on the icy Galilean satellites from the *Galileo* NIMS investigation, in *The jovian system after Galileo, the Saturnian system before Cassini-Huygens*, Nantes, France, 1998.

Hapke, B., Bidirectional reflectance spectroscopy: I. Theory, *J. Geophys. Res.* **86**, 3039–3054, 1981.

Hapke, B., Bidirectional reflectance spectroscopy: III. Correction for macroscopic roughness, *Icarus* **59**, 41–59, 1984.

Hapke, B., Bidirectional reflectance spectroscopy: IV. The extinction coefficient and the opposition effect, *Icarus* **67**, 264–280, 1986.

Hapke, B., Coherent backscatter and the radar characteristics of outer planet satellites, *Icarus* **88**, 407–417, 1990.

Hapke, B., *Theory of Reflectance and Emittance Spectroscopy*, Cambridge University Press, 1993.

Hapke, B., Bidirectional reflectance spectroscopy: V. The coherent backscatter opposition effect and anisotropic scattering, *Icarus* **157**, 523–534, 2002.

Harcke, L. J., B. J. Butler, H. A. Zebker, M. A. Slade, and R. F. Jurgens, Unambiguous 3.5 cm radar images of Ganymede and Callisto from bistatic Goldstone/VLA radar observations, *BAAS* **33**, 1107, 2001.

Hartmann, W. K., Surface evolution of two-component stone/ice bodies in the Jupiter region, *Icarus* **44**, 441–453, 1980.

Head, J. W., R. T. Pappalardo, G. Collins, and R. Greeley, Tectonic resurfacing on Ganymede and its role in the formation of grooved terrain, in *Lunar and Planetary Science Conference Abstracts*, p. 535, 1997a.

Head, J. W., R. T. Pappalardo, G. Collins, and L. Prockter, Nippur Sulcus region, Ganymede: Nature of high-latitude groove lanes and their relation to Marius Regio from *Galileo* SSI data, in *Lunar and Planetary Science Conference Abstracts*, p. 537, 1997b.

Head, J. W., R. T. Pappalardo, J. Kay, G. Collins, L. Prockter, R. Greeley, C. Chapman, M. Carr, M. J. S. Belton, and *Galileo* Imaging Team, Cryovolcanism on Ganymede: Evidence in bright terrain from *Galileo* Solid State Imaging data, in *Lunar and Planetary Science Conference Abstracts*, p. 1666, 1998.

Head, J. W., R. T. Pappalardo, and S. L. Murchie, Imaging of Ganymede, in *In Orbit at Jupiter: Contributions of the Galileo Imaging Science Team*, M. J. S. Belton (ed.), *Galileo* Project Document 625–8001, 1999.

Head, J. W., R. Pappalardo, G. Collins, M. J. S. Belton, B. Giese, R. Wagner, H. Breneman, N. Spaun, B. Nixon, G. Neukum, and J. Moore, Evidence for Europa-like tectonic resurfacing styles on Ganymede, *Geophys. Res. Lett.* **29**, 4–1, 2002.

Helfenstein, P., Dark-floored craters on Ganymede: Evidence for devolatilized impact melt, in *Lunar and Planetary Science Conference Abstracts*, pp. 331–332, 1986a.

Helfenstein, P., *Derivation and Analysis of Geological Constraints on the Emplacement and Evolution of Terrains on Ganymede from Applied Differential Photometry*, Ph.D. thesis, Brown University, 1986b.

Helfenstein, P., Modelling the phase dependence of rotational lightcurves for large satellites , *Icarus* **in preparation**, 2003.

Helfenstein, P. and E. M. Parmentier, Patterns of fracture and tidal stresses due to nonsynchronous rotation: Implications for fracturing on Europa, *Icarus* **61**, 175–184, 1985.

Helfenstein, P. and M. K. Shepard, Submillimeter-scale topography of the lunar regolith, *Icarus* **141**, 107–131, 1999.

Helfenstein, P. and Y. Shkuratov, The opposition effect and the quasi-fractal structure of regolith: II. Application and refinement, *Icarus* **in preparation**, 2003.

Helfenstein, P., J. Veverka, T. Denk, G. Neukum, J. W. Head, and R. Pappalardo, Dark-floor craters: *Galileo* constraints on a Ganymede regolith component, in *Lunar and Planetary Science Conference Abstracts*, p. 547, 1997a.

Helfenstein, P., J. Veverka, and J. Hillier, The lunar opposition effect: A test of alternative models, *Icarus* **128**, 2–14, 1997b.

Helfenstein, P., N. Currier, B. E. Clark, J. Veverka, M. Bell, R. Sullivan, J. Klemaszewski, R. Greeley, R. T. Pappalardo, J. W. Head, T. Jones, K. Klaasen, K. Magee, P. Geissler, R. Greenberg, A. McEwen, C. Phillips, T. Colvin, M. Davies, T. Denk, G. Neukum, and M. J. S. Belton, *Galileo* observations of Europa's opposition effect, *Icarus* **135**, 41–63, 1998.

Hendrix, A. R., C. A. Barth, and C. W. Hord, Ganymede's ozone-like absorber: Observations by the *Galileo* Ultraviolet Spectrometer, *J. Geophys. Res.* **104**, 14 169–14 178, 1999a.

Hendrix, A. R., C. A. Barth, A. I. F. Stewart, C. W. Hord, and A. L. Lane, Hydrogen peroxide on the icy Galilean satellites, in *Lunar and Planetary Science Conference Abstracts*, p. 2043, 1999b.

Herrick, D. L. and D. J. Stevenson, Extensional and compressional instabilities in icy satellite lithospheres, *Icarus* **85**, 191–204, 1990.

Hibbitts, C. A., T. B. McCord, and G. B. Hansen, Distributions of CO_2 and SO_2 on the surface of Callisto, *J. Geophys. Res.* **105**, 22 541–22 558, 2000.

Hibbitts, C. A., G. B. Hansen, T. B. McCord, and K. Stephan, Impactor contamination of dark ray craters on Ganymede, in *Lunar and Planetary Science Conference Abstracts*, p. 1925, 2003a.

Hibbitts, C. A., R. T. Pappalardo, G. B. Hansen, and T. B. McCord, Carbon dioxide on Ganymede, *J. Geophys. Res.* pp. 2–1, 2003b.

Hillier, J., P. Helfenstein, and J. Veverka, Latitude variations of the polar caps on Ganymede, *Icarus* **124**, 308–317, 1996.

Johnson, R. E., Polar frost formation on Ganymede, *Icarus* **62**, 344–347, 1985.

Johnson, R. E., Polar "caps" on Ganymede and Io revisited, *Icarus* **128**, 469–471, 1997.

Johnson, T. V., L. A. Soderblom, J. A. Mosher, G. E. Danielson, A. F. Cook, and P. Kupperman, Global multispectral mosaics of the icy Galilean satellites, *J. Geophys. Res.* **88**, 5789–5805, 1983.

Jones, K. B., J. Head, R. T. Pappalardo, and J. M. Moore, Morphology and origin of palimpsests on Ganymede from *Galileo* observations, *Icarus* **164**, 197–212, 2003.

Kadel, S. D., F. C. Chuang, R. Greeley, and J. M. Moore, Geological history of the Tyre region of Europa: A regional perspective on europan surface features and ice thickness, *J. Geophys. Res.* **105**, 22 656–22 669, 2000.

Kargel, J. S., Brine volcanism and the interior structures of asteroids and icy satellites, *Icarus* **94**, 368–390, 1991.

Kargel, J. S., J. Z. Kaye, J. W. Head, G. M. Marion, R. Sassen, J. K. Crowley, O. P. Ballesteros, S. A. Grant, and D. L. Hogenboom, Europa's crust and ocean: Origin, composition, and the prospects for life, *Icarus* **148**, 226–265, 2000.

Kay, J. E. and J. W. Head, Geologic mapping of the Ganymede G8 calderas region: Evidence for cryovolcanism, in *Lunar and Planetary Science Conference Abstracts*, p. 1103, 1999.

Kirk, R. L. and D. J. Stevenson, Thermal evolution of a differentiated Ganymede and implications for surface features, *Icarus* **69**, 91–134, 1987.

Kivelson, M. G., K. K. Khurana, C. T. Russell, R. J. Walker, J. Warnecke, F. V. Coroniti, C. Polanskey, D. J. Southwood, and G. Schubert, Discovery of Ganymede's magnetic field by the *Galileo* spacecraft, *Nature* **384**, 537–541, 1996.

Kivelson, M. G., J. Warnecke, L. Bennett, S. Joy, K. K. Khurana, J. A. Linker, C. T. Russell, R. J. Walker, and C. Polanskey, Ganymede's magnetosphere: Magnetometer overview, *J. Geophys. Res.* **103**, 19 963–19 972, 1998.

Kivelson, M. G., K. K. Khurana, and M. Volwerk, The permanent and inductive magnetic moments of Ganymede, *Icarus* **157**, 507–522, 2002.

Lucchitta, B. K., Grooved terrain on Ganymede, *Icarus* **44**, 481–501, 1980.

Lucchitta, B. K., C. W. Barnes, and M. F. Glotfelty, Geological map of the Memphis Facula quadrangle (Jg-7) of Ganymede, , *U. S. Geol. Surv. Map.* **I-2289**, Jg–9, 1992.

Malhotra, R., Tidal origin of the Laplace resonance and the resurfacing of Ganymede, *Icarus* **94**, 399–412, 1991.

Mandl, G., Tectonic deformation by rotating parallel faults: The bookshelf mechanism, *Tectonophysics* **141**, 277–316, 1987.

McClay, K. R. and P. G. Ellis, Geometries of extensional fault systems developed in model experiments, *Geology* **15**, 341–344, 1987.

McCord, T. B., R. Carlson, W. Smythe, G. Hansen, R. Clark, C. Hibbitts, F. Fanale, J. Granahan, M. Segura, D. Matson, T. Johnson, and P. Martin, Organics and other molecules in the surfaces of Callisto and Ganymede, *Science* **278**, 271–275, 1997.

McCord, T. B., G. B. Hansen, R. N. Clark, P. D. Martin, C. A. Hibbitts, F. P. Fanale, J. C. Granahan, M. Segura, D. L. Matson, T. V. Johnson, R. W. Carlson, W. D. Smythe, and G. E. Danielson, Non-water-ice constituents in the surface material of the icy Galilean satellites from the *Galileo* Near Infrared Mapping Spectrometer investigation, *J. Geophys. Res.* **103**, 8603–8626, 1998a.

McCord, T. B., G. B. Hansen, F. P. Fanale, R. W. Carlson, D. L. Matson, T. V. Johnson, W. D. Smythe, J. K. Crowley, P. D. Martin, A. Ocampo, C. A. Hibbitts, and J. C. Granahan, Salts on Europa's surface detected by *Galileo*'s Near Infrared Mapping Spectrometer, *Science* **280**, 1242, 1998b.

McCord, T. B., G. B. Hansen, D. L. Matson, T. V. Jonhson, J. K. Crowley, F. P. Fanale, R. W. Carlson, W. D. Smythe, P. D. Martin, C. A. Hibbitts, J. C. Granahan, and A. Ocampo, Hydrated salt minerals on Europa's surface from the *Galileo* Near Infrared Mapping Spectrometer (NIMS) investigation, *J. Geophys. Res.* **104**, 11 827–11 852, 1999.

McCord, T. B., G. B. Hansen, and C. A. Hibbitts, Hydrated salt minerals on Ganymede's surface: Evidence of an ocean below, *Science* **292**, 1523–1525, 2001a.

McCord, T. B., T. M. Orlando, G. Teeter, G. B. Hansen, M. T. Sieger, N. G. Petrik, and L. van Keulen, Thermal and radiation stability of the hydrated salt minerals epsomite, mirabilite, and natron under Europa environmental conditions, *J. Geophys. Res.* **106**, 3311–3320, 2001b.

McCord, T. B., G. Teeter, G. B. Hansen, M. T. Sieger, and T. M. Orlando, Brines exposed to Europa surface conditions, *J. Geophys. Res.* pp. 4–1, 2002.

McGuire, A. F. and B. W. Hapke, An experimental study of light scattering by large, irregular particles, *Icarus* **113**, 134–155, 1995.

McKinnon, W., P. Schenk, and J. Moore, Bright terrain–Caldera associations on Ganymede, in *Eos*, p. F792, 2000.

McKinnon, W. B., Tectonic deformation of Galileo Regio and limits to the planetary expansion of Ganymede, in *Lunar and Planetary Science Conference*, pp. 1585–1597, 1982.

McKinnon, W. B., Geodynamics of icy satellites, in *Solar System Ices*, B. Schmitt *et al.* (eds), Kluwer, pp. 525–550, 1998.

McKinnon, W. B. and H. J. Melosh, Evolution of planetary lithospheres: Evidence from multiringed structures on Ganymede and Callisto, *Icarus* **44**, 454–471, 1980.

McKinnon, W. B. and E. M. Parmentier, Ganymede and Callisto, in *Satellites*, J. A. Burns, M. S. Matthews (eds), University of Arizona Press, pp. 718–763, 1986.

Melosh, H. J., A simple mechanical model for Valhalla Basin, Callisto, *J. Geophys. Res.* **87**, 1880–1890, 1982.

Melosh, H. J. and P. Schenk, Split comets and the origin of crater chains on Ganymede and Callisto, *Nature* **365**, 731, 1993.

Millis, R. L. and D. T. Thompson, UBV photometry of the Galilean satellites, *Icarus* **26**, 408–419, 1975.

Moore, J. M. and M. C. Malin, Dome craters on Ganymede, *Geophys. Res. Lett.* **15**, 225–228, 1988.

Moore, J. M., M. T. Mellon, and A. P. Zent, Mass wasting and ground collapse in terrains of volatile-rich deposits as a solar system-wide geological process: The pre-*Galileo* view, *Icarus* **122**, 63–78, 1996.

Moore, J. M., E. Asphaug, R. J. Sullivan, J. E. Klemaszewski, K. C. Bender, R. Greeley, P. E. Geissler, A. S. McEwen, E. P. Turtle, C. B. Phillips, B. R. Tufts, J. W. Head, R. T. Pappalardo, K. B. Jones, C. R. Chapman, M. J. S. Belton, R. L. Kirk, and D. Morrison, Large impact features on Europa: Results of the *Galileo* nominal mission, *Icarus* **135**, 127–145, 1998.

Moore, J. M., E. Asphaug, D. Morrison, J. R. Spencer, C. R. Chapman, R. J. Sullivan, F. C. Chuang, J. E. Klemaszewsi, R. Greeley, K. C. Bender, P. E. Geissler, P. Helfenstein, and C. B. Pilcher, Mass movement and landform degradation on the icy Galilean satellites: Results of the *Galileo* nominal mission , *Icarus* **140**, 294–312, 1999.

Moore, J. M., E. Asphaug, M. J. S. Belton, B. Bierhaus, H. H. Breneman, S. M. Brooks, C. R. Chapman, F. C. Chuang, G. C. Collins, B. Giese, R. Greeley, J. W. Head, S. Kadel, K. P. Klaasen, J. E. Klemaszewski, K. P. Magee, J. Moreau, D. Morrison, G. Neukum, R. T. Pappalardo, C. B. Phillips, P. M. Schenk, D. A. Senske, R. J. Sullivan, E. P. Turtle, and K. K. Williams, Impact features on Europa: Results of the *Galileo* Europa Mission (GEM), *Icarus* **151**, 93–111, 2001.

Morrison, D., Introduction to the satellites of Jupiter, in *Satellites of Jupiter*, D. Morrison (ed), University of Arizona Press, pp. 3–43, 1982.

Morrison, D. and J. A. Burns, The jovian satellites, in *Jupiter*, T. Gerhels (ed), University of Arizona Press, pp. 991–1034, 1976.

Morrison, D. and D. P. Cruikshank, Thermal properties of the Galilean satellites, *Icarus* **18**, 224, 1973.

Morrison, D., N. D. Morrison, and A. R. Lazarewicz, Four-color photometry of the Galilean satellites, *Icarus* **23**, 399–416, 1974.

Mueller, S. and W. B. McKinnon, Three-layered models of Ganymede and Callisto: Compositions, structures, and aspects of evolution, *Icarus* **76**, 437–464, 1988.

Muhleman, D. O. and G. L. Berge, Observations of Mars, Uranus, Neptune, Io, Europa, Ganymede, and Callisto at a wavelength of 2.66 mm, *Icarus* **92**, 263–272, 1991.

Murchie, S. L. and J. W. Head, Possible breakup of dark terrain on Ganymede by large-scale shear faulting, *J. Geophys. Res.* **93**, 8795–8824, 1988.

Murchie, S. L., J. W. Head, P. Helfenstein, and J. B. Plescia, Terrain types and local-scale stratigraphy of grooved terrain on Ganymede, *J. Geophys. Res.* **91**, 222–212, 1986.

Murchie, S. L., J. W. Head, and J. B. Plescia, Crater densities and crater ages of different terrain types on Ganymede, *Icarus* **81**, 271–297, 1989.

Murchie, S. L., J. W. Head, and J. B. Plescia, Tectonic and volcanic evolution of dark terrain and its implications for the internal structure and evolution of Ganymede, *J. Geophys. Res.* **95**, 10 743–10 768, 1990.

Nelson, R. M., A. L. Lane, D. L. Matson, G. J. Veeder, B. J. Buratti, and E. F. Tedesco, Spectral geometric albedos of the Galilean satellites from 0.24 to 0.34 micrometers: Observations with the International Ultraviolet Explorer, *Icarus* **72**, 358–380, 1987.

Neukum, G., Bombardment history of the jovian system, in *The Three Galileos: The Man, The Spacecraft, The Telescope*, C. Barbieri, J. Rahe, T. V. Johnson, and A. M. Sohus, eds, pp. 201–212, 1997.

Neukum, G., R. Wagner, U. Wolf, B. A. Ivanov, J. W. Head, R. T. Pappalardo, J. E. Klemaszewski, R. Greeley, M. J. S. Belton, and *Galileo* SSI Team, Cratering chronology in the jovian system and derivation of absolute ages, in *Lunar and Planetary Science Conference Abstracts*, p. 1742, 1998.

Nimmo, F., R. T. Pappalardo, and B. Giese, Effective elastic thickness and heat flux estimates on Ganymede, *Geophys. Res. Lett.* **29**, 62–1, 2002.

Noll, K. S., R. E. Johnson, A. L. Lane, D. L. Domingue, H. A. Weaver, Detection of ozone on *Ganymede*, *Science*, **273**, 341, 1996.

Oberst, J., B. Schreiner, B. Giese, G. Neukum, J. W. Head, R. T. Pappalardo, and P. Helfenstein, The distribution of bright and dark material on Ganymede in relationship to surface elevation and slopes, *Icarus* **140**, 283–293, 1999.

Orton, G. S., J. R. Spencer, L. D. Travis, T. Z. Martin, and L. K. Tamppari, *Galileo* Photopolarimeter-Radiometer observations of Jupiter and the Galilean satellites, *Science* **274**, 389–391, 1996.

Ostro, S. J. and E. Shoemaker, The extraordinary radar echos from Europa, Ganymede, and Callisto: A geological perspective, *Icarus* **85**, 335–345, 2001.

Ostro, S. J., D. B. Campbell, R. A. Simpson, R. S. Hudson, J. F. Chandler, K. D. Rosema, I. I. Shapiro, E. M. Standish, R. Winkler, D. K. Yeomans, R. Velez, and R. M. Goldstein, Europa, Ganymede, and Callisto: New radar results from Arecibo and Goldstone, *J. Geophys. Res.* **97**, 18 277–18 244, 1992.

Pappalardo, R. T., *The Origin and Evolution of Ridge and Trough Terrain and the Geological History of Miranda*, Ph.D. thesis, Arizona State University, 1994.

Pappalardo, R. T. and G. C. Collins, Strained craters on Ganymede, *J. Struct. Geol.* **submitted**, 2003.

Pappalardo, R. T., J. W. Head, G. Collins, C. Pilcher, P. Helfenstein, J. Veverka, J. Burns, T. Denk, G. Neukum, and M. Belton, Ganymede northern high latitude frosts: Preliminary observations from *Galileo* SSI data, in *Lunar and Planetary Science Conference Abstracts*, p. 1065, 1997a.

Pappalardo, R. T., J. W. Head, B. Tufts, G. Collins, L. Prockter, and the *Galileo* imaging team, *Galileo* images of a region of transitional terrain on Ganymede: Preliminary analysis, in *Lunar and Planetary Science Conference Abstracts*, p. 1065, 1997b.

Pappalardo, R. T., J. W. Head, G. C. Collins, R. L. Kirk, G. Neukum, J. Oberst, B. Giese, R. Greeley, C. R. Chapman, P. Helfenstein, J. M. Moore, A. McEwen, B. R. Tufts, D. A. Senske, H. H. Breneman, and K. Klaasen, Grooved terrain on Ganymede: First results from *Galileo* high-resolution imaging, *Icarus* **135**, 276–302, 1998a.

Pappalardo, R. T., K. K. Khurana, T. Denk, W. Ip, T. Rosanova, A. S. McEwen, T. V. Johnson, P. E. Helfenstein, J. W. Head, R. Goyal, J. Warnecke, M. G. Kivelson, G. Neukum, L. Gaddis, T. Becker, *Galileo* Imaging Team, and *Galileo* Magnetometer Team, A comparison of the plasma bombardment boundary on Ganymede's surface to *Galileo* imaging data, *BAAS* **30**, 1120, 1998b.

Pappalardo, R. T., K. K. Khurana, and W. B. Moore, The grandeur of Ganymede: Suggested goals for an orbiter mission, in *Forum on Innovative Approaches to Outer Planetary Exploration 2001–2020*, p. 62, 2001.

Pappalardo, R. T., F. Nimmo, B. Giese, C. E. Bader, L. C. DeRemer, and L. M. Prockter, Furrow topography and the thickness of *Ganymede*'s dark terrain lithosphere, *Lunar Planet. Sci. Conf.*, **XXXIV**, 2003.

Parmentier, E. M., S. W. Squyres, J. W. Head, and M. L. Allison, The tectonics of Ganymede, *Nature* **295**, 290–293, 1982.

Passey, Q. R. and E. M. Shoemaker, Craters and basins on Ganymede and Callisto: Morphological indicators of crustal evolution, in *Satellites of Jupiter*, D. Morrison (ed), University of Arizona Press, pp. 379–434, 1982.

Patel, J. G., R. T. Pappalardo, J. W. Head, G. C. Collins, H. Hiesinger, and J. Sun, Topographic wavelengths of Ganymede groove lanes from Fourier analysis of *Galileo* images, *J. Geophys. Res.* **104**, 24 057–24 074, 1999.

Peale, S. J., Rotation histories of the natural satellites, in *Planetary Satellites*, J. A. Burns (ed), University of Arizona Press, pp. 87–111, 1977.

Peters, K., The coherent backscattering effect: A vector formulation accounting for polarization and absorption effects and small and large scatterers, *Phys. Rev. B* **42**, 801–812, 1992.

Prockter, L. M., J. W. Head, R. T. Pappalardo, D. A. Senske, G. Neukum, R. Wagner, U. Wolf, J. O. Oberst, B. Giese, J. M. Moore, C. R. Chapman, P. Helfenstein, R. Greeley, H. H. Breneman, and M. J. S. Belton, Dark terrain on Ganymede: Geological mapping and interpretation of Galileo Regio at high resolution, *Icarus* **135**, 317–344, 1998.

Prockter, L. M., P. H. Figueredo, R. T. Pappalardo, J. W. Head, and G. C. Collins, Geology and mapping of dark terrain on Ganymede and implications for grooved terrain formation, *J. Geophys. Res.* **105**, 22 519–22 540, 2000.

Prockter, L. M., J. W. Head, R. T. Pappalardo, R. J. Sullivan, A. E. Clifton, B. Giese, R. Wagner, and G. Neukum, Morphology of Europan bands at high resolution: A mid-ocean ridge-type rift mechanism, *J. Geophys. Res.* pp. 4–1, 2002.

Purves, N. G. and C. B. Pilcher, Thermal migration of water on the Galilean satellites, *Icarus* **43**, 51–55, 1980.

Ruiz, J., The stability against freezing of an internal liquid-water ocean in Callisto, *Nature* **412**, 409–411, 2001.

Schenk, P. M., Ganymede and Callisto: Complex crater formation and planetary crusts, *J. Geophys. Res.* **96**, 15 635, 1991.

Schenk, P. M., Central pit and dome craters: Exposing the interiors of Ganymede and Callisto, *J. Geophys. Res.* **98**, 7475–7498, 1993.

Schenk, P. M. and W. B. McKinnon, Ring geometry on Ganymede and Callisto, *Icarus* **72**, 209–234, 1987.

Schenk, P. M. and W. B. McKinnon, Fault offsets and lateral crustal movement on Europa: Evidence for a mobile ice shell, *Icarus* **79**, 75–100, 1989.

Schenk, P. M. and W. B. McKinnon, Dark-ray and dark-floor craters on Ganymede, and the provenance of large impactors in the jovian system, *Icarus* **89**, 318–346, 1991.

Schenk, P. M. and J. M. Moore, Volcanic constructs on Ganymede and Enceladus: Topographic evidence from stereo images and photoclinometry, *J. Geophys. Res.* **100**, 19 009–19 022, 1995.

Schenk, P. M. and F. J. Ridolfi, Morphology and scaling of ejecta deposits on icy satellites, *Geophys. Res. Lett.* **29**, 31–1, 2002.

Schenk, P. M., E. Asphaug, W. B. McKinnon, H. J. Melosh, and P. R. Weissman, Cometary nuclei and tidal disruption: The geologic record of crater chains on Callisto and Ganymede, *Icarus* **121**, 249–274, 1996.

Schenk, P. M., W. B. McKinnon, D. Gwynn, and J. M. Moore, Flooding of Ganymede's bright terrains by low-viscosity water-ice lavas, *Nature* **410**, 57–60, 2001.

Schubert, G., T. Spohn, and R. T. Reynolds, Thermal histories, compositions and internal structures of the moons of the solar system, in *Satellites*, J. A. Burns, M. S. Matthews (eds), University of Arizona Press, pp. 224–292, 1986.

Shaya, E. J. and C. B. Pilcher, Polar cap formation on Ganymede, *Icarus* **58**, 74–80, 1984.

Shkuratov, Y. G. and P. Helfenstein, The opposition effect and the quasi-fractal structure of regolith: I. Theory, *Icarus* **152**, 96–116, 2001.

Shoemaker, E. M., B. K. Lucchitta, D. E. Wilhelms, J. B. Plescia, and S. W. Squyres, The geology of Ganymede, in *Satellites of Jupiter*, D. Morrison (ed), University of Arizona Press, pp. 435–520, 1982.

Showman, A. P. and R. Malhotra, Tidal evolution into the Laplace resonance and the resurfacing of Ganymede, *Icarus* **127**, 93–111, 1997.

Showman, A. P. and I. Mosqueira, On the liquid-water resurfacing of Ganymede, *BAAS* **33**, 0, 2001.

Showman, A. P., D. J. Stevenson, and R. Malhotra, Coupled orbital and thermal evolution of Ganymede, *Icarus* **129**, 367–383, 1997.

Sieveka, E. M. and R. E. Johnson, Thermal- and plasma-induced molecular redistribution on the icy satellites, *Icarus* **51**, 528–548, 1982.

Smith, B. A., L. A. Soderblom, T. V. Johnson, A. P. Ingersoll, S. A. Collins, E. M. Shoemaker, G. E. Hunt, H. Masursky, M. H. Carr, M. E. Davies, A. F. Cook, J. M. Boyce, T. Owen, G. E. Danielson, C. Sagan, R. F. Beebe, J. Veverka, J. F. McCauley, R. G. Strom, D. Morrison, G. A. Briggs, and V. E. Suomi, The Jupiter system through the eyes of *Voyager 1*, *Science* **204**, 951–957, 1979.

Smith, B. A., L. A. Soderblom, R. Beebe, J. Boyce, G. Briggs, M. Carr, S. A. Collins, A. F. Cook II, G. E. Danielson, M. E. Davies, G. E. Hunt, A. P. Ingersoll, T. V. Johnson, H. Masursky, J. F. McCauley, D. Morrison, T. Owen, C. Sagan, E. M. Shoemaker, R. G. Strom, V. E. Suomi, and J. Veverka, The Galilean satellites and Jupiter: *Voyager 2* imaging science results, *Science* **206**, 927–950, 1979b.

Spaun, N. A., J. W. Head, R. T. Pappalardo, and the *Galileo* SSI Team, Scalloped depressions on Ganymede from *Galileo* (G28) very high resolution imaging, in *Lunar and Planetary Science Conference Abstracts*, p. 1448, 2001.

Spencer, J. R., *The Surfaces of Europa, Ganymede, and Callisto: An Investigation Using Voyager IRIS Thermal Infrared Spectra*, Ph.D. thesis, University of Arizona, 1987a.

Spencer, J. R., Thermal segregation of water ice on the Galilean satellites, *Icarus* **69**, 297–313, 1987b.

Spencer, J. R., W. M. Calvin, and M. J. Person, CCD spectra of the Galilean satellites: Molecular oxygen on Ganymede, *J. Geophys. Res.* **100**, 19 049–19 056, 1995.

Spencer, J. R., L. Prockter, R. Pappalardo, J. Head, J. Moore, and *Galileo* SSI Team, Local volatile migration on Ganymede: *Galileo* SSI images, PPR radiometry, and theoretical considerations, in *Lunar and Planetary Science Conference Abstracts*, p. 1149, 1998.

Spencer, J. R., L. K. Tamppari, T. Z. Martin, and L. D. Travis, Temperatures on Europa from *Galileo* PPR: Nighttime thermal anomalies, *Science* **284**, 1514–1516, 1999.

Squyres, S. W., Surface temperatures and retention of H_2O frost on Ganymede and Callisto, *Icarus* **44**, 502–510, 1980a.

Squyres, S. W., Volume changes in Ganymede and Callisto and the origin of grooved terrain, *Geophys. Res. Lett.* **7**, 593–596, 1980b.

Squyres, S. W., The topography of Ganymede's grooved terrain, *Icarus* **46**, 156–168, 1981.

Squyres, S. W., The evolution of tectonic features on Ganymede, *Icarus* **52**, 545–559, 1982.

Squyres, S. W. and J. Veverka, *Voyager* photometry of surface features on Ganymede and Callisto, *Icarus* **46**, 137–155, 1981.

Stebbins, J., The light-variations of the satellites of Jupiter and their application to measures of the solar constant, *Lick Observatory Bulletin* **13**, 1–11, 1927.

Sullivan, R., R. Greeley, K. Homan, J. Klemaszewski, M. J. S. Belton, M. H. Carr, C. R. Chapman, R. Tufts, J. W. Head, and R. Pappalardo, Episodic plate separation and fracture in fill on the surface of Europa, *Nature* **391**, 371, 1998.

Thomas, P. J. and S. W. Squyres, Formation of crater palimpsests on Ganymede, *J. Geophys. Res.* **95**, 19 161–19 174, 1990.

van Wyk de Vries, B. and O. Merle, The effect of volcanic constructs on rift fault patterns, *Geology* **24**, 643–646, 1996.

Vendeville, B., P. R. Cobbold, P. Davy, J. Brun, and P. Choukroune, Physical models of extensional tectonics at various scales, in *Continental Extensional Tectonics*, M. P. Coward *et al.* (eds), vol. 28, pp. 95–107, Geol. Soc. Amer. Spec. Publ., 1987.

Vidal, R. A., D. Bahr, R. A. Baragiola, and M. Peters, Oxygen on Ganymede: Laboratory studies, *Science* **276**, 1839–1842, 1997.

Warren, S. G., Optical constants of ice from the ultraviolet to the microwave, *Appl. Opt.* **23**, 1206–1225, 1984.

Wernicke, B. and B. C. Burchfiel, Modes of extensional tectonics, *J. Struct. Geol.* **4**, 105–115, 1982.

Woodcock, N. H. and M. Fischer, Strike-slip duplexes, *J. Struct. Geol.* **10**, 725–735, 1988.

Yingst, R. A., J. W. Head, J. M. Moore, C. R. Chapman, and R. Pappalardo, Ganymede bright terrain at very high resolution: Geologic structure and regolith processes, in *Lunar and Planetary Science Conference Abstracts*, p. 1611, 1997.

Zahnle, K., L. Dones, and H. F. Levison, Cratering rates on the Galilean satellites, *Icarus* **136**, 202–222, 1998.

Zahnle, K., P. Schenk, S. Sobieszczyk, L. Dones, and H. F. Levison, Differential cratering of synchronously rotating satellites by ecliptic comets, *Icarus* **153**, 111–129, 2001.

Zahnle, K., P. Schenk, H. Levison, and L. Dones, Cratering rates in the outer solar system, *Icarus* **163**, 263–289, 2003.

Zolotov, M. Y. and E. L. Shock, Composition and stability of salts on the surface of Europa and their oceanic origin, *J. Geophys. Res.* **106**, 32 815–32 828, 2001.

Zuber, M. T. and E. M. Parmentier, Lithospheric stresses due to radiogenic heating of an ice-silicate planetary body: Implications for Ganymede's tectonic evolution, *J. Geophys. Res.* **89**, 429–, 1984.